ENERGETICS OF SHOALING INTERNAL WAVES AND TURBULENCE IN THE ST. LAWRENCE ESTUARY

by

Clark Richards

Submitted in partial fulfillment of the requirements
for the degree of Doctor of Philosophy

at

Dalhousie University
Halifax, Nova Scotia
August 2012

DALHOUSIE UNIVERSITY

DEPARTMENT OF OCEANOGRAPHY

The undersigned hereby certify that they have read and recommend to the Faculty of Graduate Studies for acceptance a thesis entitled "ENERGETICS OF SHOALING INTERNAL WAVES AND TURBULENCE IN THE ST. LAWRENCE ESTUARY" by Clark Richards in partial fulfillment of the requirements for the degree of Doctor of Philosophy.

Dated: August 17, 2012

External Examiner: _____

Research Supervisor: _____

Examining Committee: _____

_____

_____

Departmental Representative: _____

DALHOUSIE UNIVERSITY

DATE: August 17, 2012

AUTHOR: Clark Richards

TITLE: ENERGETICS OF SHOALING INTERNAL WAVES AND TURBULENCE IN THE ST. LAWRENCE ESTUARY

DEPARTMENT OR SCHOOL: Department of Oceanography

DEGREE: PhD CONVOCATION: October YEAR: 2012

Signature of Author

For Juniper and Linden

Table of Contents

List of Tables

List of Figures

Abstract

The shoaling of horizontally propagating internal waves may provide an important source of mixing and transport in estuaries and coastal seas. Parameterizing such effects in numerical models demands better understanding of several aspects of wave energetics, especially relating to horizontal energy flux and turbulence generation. Observations are needed to build this understanding. To address some of these issues in the estuarine context, an intensive field program was undertaken in Summer 2008 in the St. Lawrence Estuary, involving shore-based photogrammetry, ship-based surveys, and moorings that held conventional and turbulence-resolving sensors. The measurements reveal that waves generally arrived during the rising phase of the M_2 tide. Shoreward of the 40 m isobath, waves traversed the field site perpendicular to bathymetry, a pattern that continued as the waves transformed nonlinearly. A tight temperature-salinity relationship permits the estimation of the time-varying density field from a moored chain of temperature-depth recorders. A new method for inferring the heaved internal wave density field is developed, using a relaxation solver to determine the wave streamfunction. The method is applied to discrete events measured with acoustic Doppler profilers to estimate the kinetic and available potential energy, as well as the nonlinear horizontal energy flux. Acoustic Doppler velocimeters were used to infer near-bottom turbulent energetics, revealing two main features. First, a period of wave incidence had turbulence dissipation rates that exceeded values associated with tidal shear by an order of magnitude. Second, the evolving spectral signatures associated with a particular wave-shoaling event indicate that the turbulence is at least partly locally generated. A simple model for wave-induced turbulence is proposed based on the energy flux measurements. Generally, the results suggest that during the rising phase of the tide, energy input from shoaling waves is required to explain the observed levels of dissipation. Estimates of vertical diffusivity during times of wave shoaling are on average 3 times larger than values predicted by tidal shear alone.

List of Abbreviations and Symbols Used

Abbreviation	Description
ADCP	acoustic Doppler current profiler (manufactured by RDInstruments)
ADP	acoustic Doppler profiler (generic)
ADV	acoustic Doppler velocimeter
ENU	East-North-Up coordinate system
XYZ	Instrument coordinate system
CTD	conductivity-temperature-depth instrument
DJL	Dubreil-Jacotin-Long
M01-M11	SLEIWEX 2008 mooring name
SLEIWEX	St. Lawrence Estuary internal wave experiment
TDR	temperature-depth recorder

Roman symbol	Description	Unit
N	buoyancy frequency	s^{-1}
C_D	bottom drag coefficient	NA
J_b	buoyancy flux	W/kg
K_V	vertical diffusivity	m^2/s
g	acceleration due to gravity	m/s^2
APE	available potential energy	J
BPE	background potential energy	J
PE	gravitational potential energy	J
E	energy	J
KE	kinetic energy	J
KE_w	internal wave kinetic energy proxy	J/kg
E_a	available potential energy density	J/m^3
E_k	kinetic energy density	J/m^3

Roman symbol	Description	Unit
E_p	potential energy density	$\mathrm{J/m^3}$
E_w	perturbation potential energy density	$\mathrm{J/m^3}$
$\mathcal{E}$	pseudoenergy density	$\mathrm{J/m^3}$
f_E	total horizontal energy density flux	$\mathrm{W/m^2}$
$\mathcal{F}$	relaxation convergence criterion	NA
H	total water depth	m
i, j	matrix indices (rows, columns)	NA
I, J	matrix dimensions (rows, columns)	NA
c	phase velocity	m/s
c_n	phase velocity of n^{th} normal mode	m/s
c_{wnl}	weakly nonlinear phase velocity	m/s
p	pressure	$\mathrm{N/m^2}$
p_w	total pressure perturbation for a wave	$\mathrm{N/m^2}$
$\rho_0 g \eta_0$	external pressure perturbation	$\mathrm{N/m^2}$
p_h	internal hydrostatic pressure perturbation	$\mathrm{N/m^2}$
p_{nh}	nonhydrostatic pressure perturbation	$\mathrm{N/m^2}$
Ri	gradient Richardson number	NA
R_f	flux Richardson number	NA
R	velocity residual for ψ calculation	m/s
S	practical salinity	PSU
$\mathcal{S}$	magnitude of the vertical shear of the horizontal current	$\mathrm{s^{-1}}$
T	temperature	°C
t	time	s
$\mathbf{u}$	3D velocity vector	m/s
u	eastward velocity	m/s
u_*	friction velocity	m/s
U_f	low-pass filtered near-bottom velocity	m/s
v	westward velocity	m/s
w	vertical velocity	m/s
V_n	velocity normal to the boundary	m/s

Roman symbol	Description	Unit
V_s	velocity tangential to the boundary	m/s
x, y, z	Eulerian coordinates	m
k	wavenumber magnitude	1/ m
$\mathbf{k}$	wavenumber vector	1/ m
z^*	height of fluid element in reference state	m
z_0	roughness height (law of the wall)	m
$\bar{\cdot}$	averaging operator	NA
$\langle\cdot\rangle_{ba}$	bin average	NA
$\langle\cdot\rangle_{lp}$	low-pass filter	NA
$\langle\cdot\rangle_{\phi}$	phase average	NA
$\langle\cdot\rangle$	integration over time and depth	NA
$\cdot'$	a small perturbation	NA

Greek symbol	Description	Unit
ϵ	rate of dissipation of turbulence kinetic energy	W/kg
η	isopycnal displacement	m
η_0	surface displacement	m
Γ	mixing efficiency	NA
κ_ρ	scalar diffusivity	m^2/s
μ	dynamic viscosity of water	$kg\,m^{-1}\,s^{-1}$
ν	kinematic viscosity of water	m^2/s
Π_n	vertical structure function for mode n	NA
ψ	velocity streamfunction	m^2/s
ψ_b	ψ values on a boundary	m^2/s
$\psi_{i,j}^{(t)}$	ψ evaluated at location (i,j) and time t	m^2/s
ρ	density of water	kg/m^3
ρ_0	a reference density	kg/m^3
ρ_w	perturbation density	kg/m^3
$\overline{\rho}$	reference density profile	kg/m^3
ρ_r	adiabatically rearranged reference density profile	kg/m^3
σ_T	$\rho - 1000$	kg/m^3
σ_θ	Potential density	kg/m^3
θ	Potential temperature	°C
ϕ	Tidal phase	rad
κ	von Karman's constant	NA
ζ	vorticity	s^{-1}
$\hat{\zeta}$	vorticity estimated from data	s^{-1}

Acknowledgements

The work contained in this thesis could not have been undertaken or completed without the support and encouragement from a large number of people. I am blessed to have been surrounded by such dedication and inspiration.

To my supervisor, Dan, whose unfailing support kept me always inquiring, learning, and exploring, my thanks cannot be counted by the pages contained herein. Nor by the approximately 3000 emails sent and received between us in the last 3 years alone (an average of 24 a day!), by the (countless) hours spent exchanging ideas or seeking advice, or by the scribbles and drawings put to paper and chalkboard. I value our friendship, and look forward to continuing our collaborations.

Thanks also to my SLEIWEX colleague and friend Daniel Bourgault who, after introducing me to the project and helping me write a proposal to obtain funding, watched me skip off to the mainland to attend Dalhousie. And to Alex Hay and Peter Galbraith, as well as the rest of the SLEIWEX 2008 team (Trajce Alcinov, Richard Cheel, Rémi Demarais, Jack Foley, Walter Judge, Doug Schillinger, and the Captain and Crew of the *RV Coriolis II*), without whom the field work would not have been possible.

I thank my committee members, both past and present, whose expertise I regret that I didn't take advantage of sooner in my program, but whose guidance (when I learned how to ask for it) helped make the work stronger.

To Jackie, for all the wonderful conversations and the help with *everything* over the years. To Daniel Morrison, for fixing my computer no matter how badly I broke it. To my fellow students, too many to list, who make this department what it is. And to my office mates Ramzi and Eric, who patiently listened to me say "Quick question ..." more times that I can count.

To my parents (Bill and Barb, Deborah and Yvan), in-laws (Mary and Bob), and brothers and sisters, whose support (and childcare) during the final stages of the writing were instrumental to its completion. There were times where I didn't think I'd be able to finish – that I even managed to find any time to attempt to is because of them.

Finally, to my wife Tara, whose love and support lie at the base of everything I have accomplished during this time. To say that I couldn't have done this without her is an understatement – the sleepness nights with kids, picking up all the slack I was forced to leave around the house, and the unfailing determination and encouragement in the face of it all are but a few of the monumental tasks which fell on her shoulders. This thesis is as much hers as mine (and unconsciously she probably understands as much as I do, just from patiently listening to me babble). Thank-you.

Chapter 1

Introduction

Nonlinear internal waves have increasingly been recognized as important features in the ocean, where they may contribute to turbulence, mixing, and the horizontal transport of momentum and fluid. This is especially true in coastal seas such as estuaries and continental shelves, where strong tidal motions of stratified fluid over steep topography result in conditions favourable to internal wave generation. The subsequent redistribution of energy from the mean flow through internal waves, and eventually to turbulence and mixing, represents a facet of the oceanic energy cascade from large to small scales that is currently unresolved in regional circulation models.

From a societal perspective, understanding coastal mixing and circulation is important, as we depend on coastal seas for natural resources, transportation, recreation, and waste dispersal. Coastal circulation and mixing processes are also important ecologically, mediating the supply of nutrients to surface waters, and for transporting larvae. More broadly, the mechanisms that mix stratified fluid at ocean boundaries may have an influence on water properties in the deep ocean, through lateral spreading of mixed water along isopycnals.

For the effects of nonlinear internal waves to be included in regional models, suitable parameterizations must be developed, based on large scale quantities that can be resolved by the model (e.g. currents and stratification). All stages of wave lifetime will need to be incorporated, including generation, propagation, and dissipation. Developing realistic parameterizations requires detailed knowledge of the physics involved (which may include nonlinear and nonhydrostatic effects that occur on small spatial scales), and of the dependence on the large scale variables.

Studies of mixing caused by internal waves have included laboratory experiments, direct numerical simulation, and field observations. Much insight has been gained from laboratory experiments and numerical simulations, particularly relating to wave dissipation and turbulence. Extending the results to field scenarios can be challenging, however, owing to the influence of background conditions not included in experiments. Further, to avoid aliasing, field observations are typically limited by the requirement for dense spatial and temporal sampling of the velocity and density fields.

A recent focus on observations of nonlinear internal waves, particularly on continental shelves, has led to insights regarding their energetics and associated turbulence. The applicability of results from continental shelves to estuarine systems has yet to be demonstrated, however, and this is an issue that needs consideration, as the latter tend to have different physical scales, background stratification, and flow fields. This provides a good incentive to undertake studies of internal waves and turbulence in estuaries.

Such is the aim of this thesis – to quantify the influence of shoaling internal waves on turbulence at a location in the St. Lawrence Estuary. The measurements are derived from an intensive field campaign undertaken in summer 2008 which involved a variety of moored, underway, and shore-based instrumentation.

The following sections present a brief summary of oceanic internal waves and of the St. Lawrence Estuary, followed by a statement of research goals and an outline of the thesis.

1.1 Internal Waves

For a fluid with a gravitationally stable density structure, the dispersion relation for linear (i.e. small-amplitude) internal waves propagating in the (x, z) plane is (see e.g. *Gill*, 1982, Chapter 6)

$$\omega = \frac{k_w N}{(k_w^2 + m_w^2)^{1/2}}, \tag{1.1}$$

where ω is the wave frequency, k_w and m_w are the horizontal and vertical components of the wavenumber vector, and N is the buoyancy frequency, given by

$$N = \left(-\frac{g}{\rho_0} \frac{\partial \rho}{\partial z} \right)^{1/2}, \tag{1.2}$$

where g is the acceleration due to gravity, and ρ_0 is a constant reference density.

When $\rho(z)$ contains a single discontinuity, the system is said to be "two-layered"[1]. In such cases, the pycnocline (the region of maximum vertical density gradient) acts as a waveguide along which disturbances propagate horizontally. Internal waves of this type are often called "interfacial waves".

When $\rho(z)$ is continuous, the water column can support more complex motions, and internal waves may propagate at an angle to the vertical according to Equation 1.1. For this case, the response can be separated into orthogonal modes (see Section 3.5.3 as well as e.g. *Kundu and Cohen* (2002), Chapter 14 Section 9), each comprising a vertical structure function and associated phase speed. When the vertical density structure is approximately two-layered (as is often the case in estuaries and coastal seas), the phase speed of the first mode will be largest, and it will tend to dominate the observed wave field (see e.g. *Gill*, 1982, Chapter 6.11).

As the wave amplitude increases, the nonlinear terms in the equations of motion become increasingly important. Nonlinearity will tend to steepen the waves as they evolve, whereas dispersion will act to counter the steepening. If the nonlinear steepening is balanced by the dispersion, the result is a stable wave of constant form, known generally as a "soliton". Solitons occurring below the ocean surface are called "internal solitary waves"[2], and have been known to exist since the 1960's (see e.g. the review by *Helfrich and Melville*, 2006). The Korteweg-de Vries (KdV) equation describes a solitary wave solution for weak nonlinearity and dispersion. Typical observations of solitary internal waves have amplitudes beyond the limits of the KdV assumptions, and in such situations, more complicated theories must be invoked to described the observed wave properties (see Appendix B, and also *Helfrich and Melville* (2006) for further review).

[1] In this case, $N(z)$ is given by a delta-function, centred on the discontinuity.

[2] Despite the fact that the waves are referred to as "solitary", singular waves are rarely observed in nature. More often, a "train" of internal solitary waves will be observed, rank-ordered with amplitude due to the dependence of phase speed on wave size.

1.2 The St. Lawrence Estuary

The St. Lawrence Estuary is a large estuary (over 300 km long) in eastern Canada, and is the location at which freshwater from the Great Lakes and seawater from the North Atlantic ocean intermingle. With a mean flow of over $10^4\,\mathrm{m}^3/\mathrm{s}$, the St. Lawrence River has the largest freshwater discharge of any North American river on the Atlantic coast, and represents 80% of the total flow into the St. Lawrence Estuary (*El-Sabh*, 1988).

Geographically, the St. Lawrence Estuary is divided into two regions, comprising the upper and lower estuaries (see Figure 1.1). The division is near the mouth of the Saguenay fjord at Tadoussac, in a region known as the "Head of the Laurentian Channel". This region, characterized by large variations in bottom topography including several sills, is an area of intense mixing, hydraulic control, and water mass transformation that influences water mass properties in the upper estuary (see e.g. *El-Sabh*, 1988; *Saucier and Chassé*, 2000).

The upper estuary is typically classified as a partially mixed estuary (*El-Sabh*, 1988), with the deep (up to 120 m) northern portion of the channel containing much of the circulation. The southern channel, characterized by water depths generally less than 10 m, exhibits little stratification owing to mixing caused by strong tidal currents.

1.3 Observations of Internal Waves in the St. Lawrence Estuary

Observations of internal waves in the St. Lawrence Estuary began with the study of *Deguise* (1977), followed by *Ingram* (1978) who observed nonlinear internal waves in aerial photographs and *in situ* measurements near Île Rouge. The internal waves were thought to be generated from a warm surface front during ebb flow. *Galbraith* (1992) observed solitary internal waves in the same region during a period of rapid sampling with a CTD, and the resulting mixing was estimated to be larger than that associated with internal tidal shear in the region. *Bourgault et al.* (2001) observed a strongly nonlinear internal wave train in the upper estuary, about 25 km upstream from the head of the Laurentian Channel.

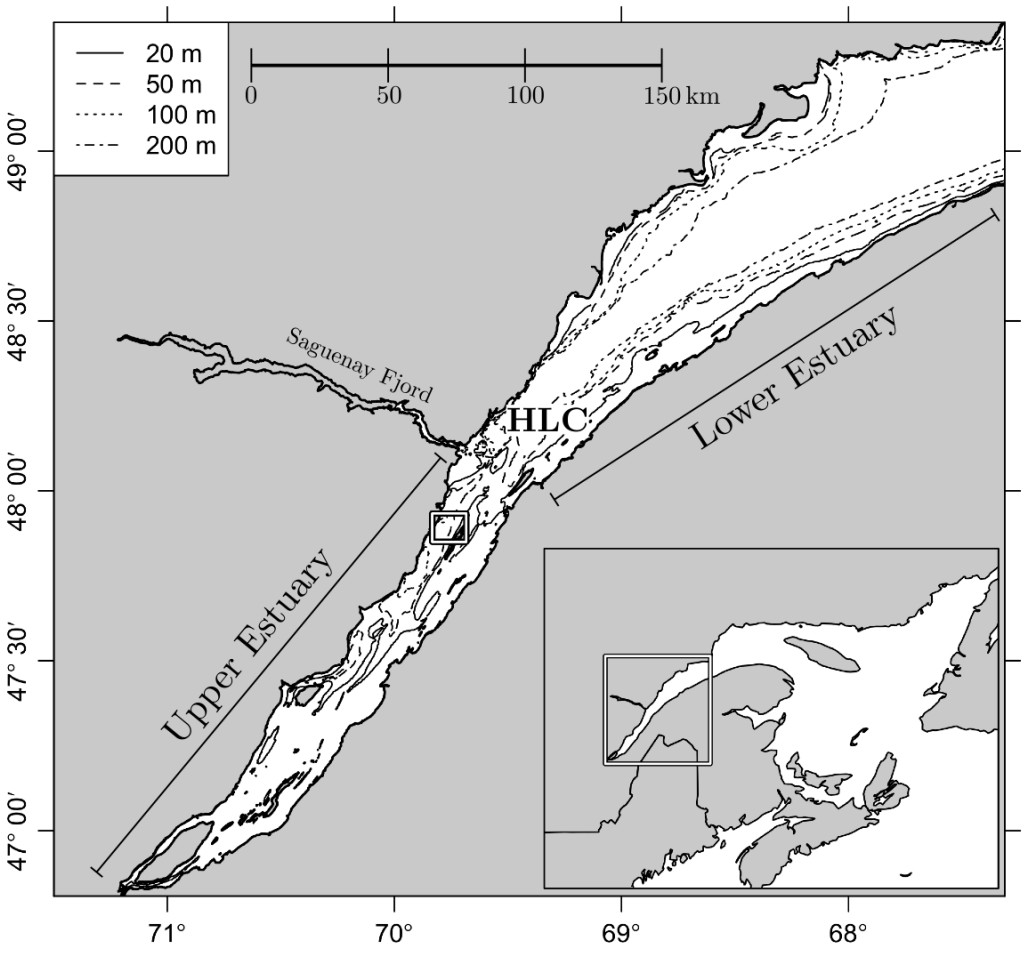

Figure 1.1: The St. Lawrence Estuary. HLC indicates the Head of the Laurentian Channel, near the mouth of the Saguenay fjord (see text). The field site for this thesis is indicated by the box to the South of the Saguenay, corresponding to the domain plotted in Figure 2.1. Depths of bathymetric contours are indicated in the legend. Inset on the lower right is the Gulf of St. Lawrence and Atlantic Canada.

Field work related to boundary mixing caused by internal waves began with an exploratory study that identified a region in the upper St. Lawrence Estuary where high-frequency internal waves regularly approach a nearly planar bottom at approximately right angles (*Bourgault and Kelley*, 2003). Located in the same area as the study of *Bourgault et al.* (2001) near Île aux Lièvres, the 2003 study began the research programme known as the St. Lawrence Estuary Internal Wave Experiment (SLEIWEX hereafter), for which follow-up work offered insights on internal wave shoaling (*Bourgault et al.*, 2005, 2007) and reflectance (*Bourgault and Kelley*, 2007).

These in turn led to the data analysis techniques of *Mirshak and Kelley* (2009), and the first time-varying estimates of internal wave energy flux (*Mirshak*, 2008, Chapter 6). A recent focus has been on the breaking phase of internal waves, including bolus production and turbulence (*Bourgault et al.*, 2008). This thesis will focus on the issues of energy flux and turbulence, which are of particular interest from the point of view of parameterizing the role of internal waves in coastal mixing.

1.4 Goals and Thesis Outline

The goal of this thesis is to quantify the effect of internal waves on near-bottom turbulence in the St. Lawrence Estuary. This will be accomplished through several sub-goals, outlined briefly here and detailed in subsequent chapters.

Chapter 2 introduces the SLEIWEX 2008 experiment, including the data sources used in this thesis, and some of the data processing required prior to analysis.

Chapter 3 summarizes the background oceanographic conditions at the field site, including currents, shear, and hydrography. The time varying fields to be used in the remainder of the thesis will be developed, including vertical density structure and a proxy for internal wave kinetic energy density.

Chapter 4 presents a new method for inferring the wave-heaved density field for a nonlinear internal wave from measurements made with an acoustic current profiler. The method is shown to be acceptably insensitive to noise and background shear, and is well suited for application to waves in the St. Lawrence Estuary.

Chapter 5 deals with measurements of internal wave energy and energy flux, as inferred from the mooring array and utilizing the technique developed in Chapter 4 and the background fields from Chapter 3.

Chapter 6 presents measurements of near-bottom turbulence, assessed by inferring the dissipation rate of turbulence kinetic energy from vertical velocity spectra measured from an acoustic Doppler velocimeter.

Chapter 7 synthesizes the results from Chapters 5 and 6, to assess the connection between turbulence and internal waves at the field site. Additionally, the implications for mixing are discussed.

Chapter 8 provides a summary of the results, and some directions for future work.

Chapter 2

SLEIWEX 2008

In this chapter, a brief overview of the SLEIWEX 2008 experiment will be given, prior to the presentation of scientific results in following chapters. The purpose is primarily for context; details such as mooring names, data sources, instrument types, and several data processing techniques will be summarized.

2.1 Field Site and Experiment

The 2008 SLEIWEX field program, jointly funded by CFCAS (the Canadian Foundation for Climate and Atmospheric Sciences; core funding) and NSERC (the Natural Sciences and Engineering Research Council of Canada; ship time), had the goal of sampling internal waves in the St. Lawrence Estuary throughout their entire lifecycle, from generation, through propagation, to dissipation. Many aspects of these three processes were observed, with the present thesis focusing primarily on the latter two.

The study site, located in the North Channel of the St. Lawrence Estuary along the flanks of Île aux Lièvres, is shown in Figure 2.1. Previous studies identified the area shoreward of the 40 m isobath as a region of active internal wave shoaling and overturning (*Bourgault et al.*, 2005, 2007). In this area, termed the "dissipation zone", the sloping bottom leading up to the shoreline at Île aux Lièvres has a maximum steepness of approximately 2°, and is relatively uniform between the 40 and 10 m isobaths.

The experiment took place between 2008-06-25 and 2008-07-04, with mooring deployment and recovery occupying the first and last days. Some pre-sampling was carried out the week prior, including shore-based photogrammetry (Section 2.2.3)

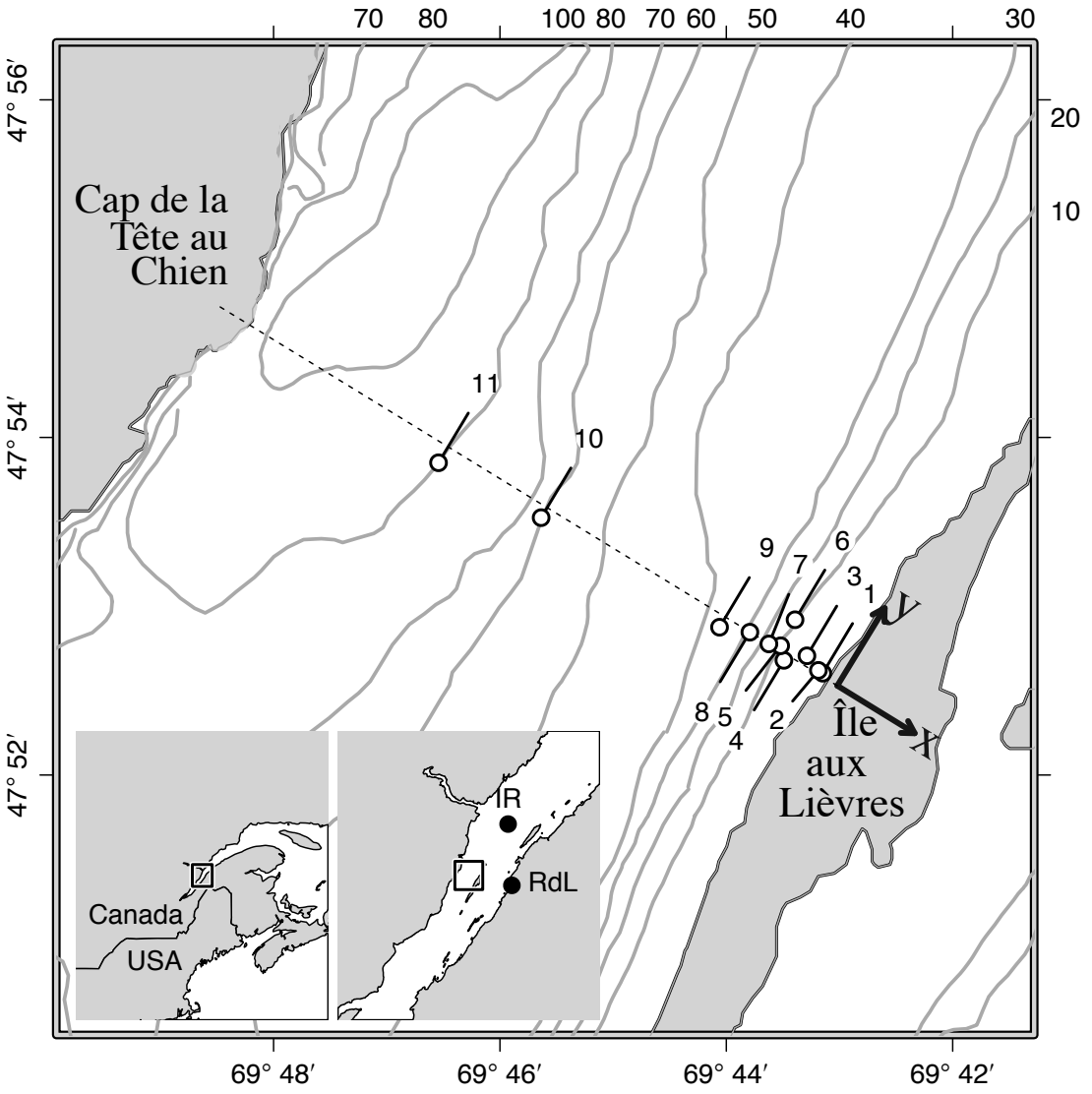

Figure 2.1: Study region, showing 11 moorings near Île aux Lièvres, an island in the St. Lawrence Estuary (insets). Contours of depth in metres are labelled outside the frame. The dashed line indicates the orientation of a time-lapse camera system set up on the island to overlook the moorings. The axes of an xy coordinate system centered on this camera (47° 52.529′ N; 69° 43.019′ W) are drawn to indicate 1 km distance. Locations labelled on the medium-scale inset include Île Rouge (IR) and Rivière-du-Loup (RdL).

to select the exact location for mooring deployment. A terrain-based xy coordinate system was constructed to simplify the analysis, with the origin located on the island. The x-axis was rotated from East by $-31.5°$ (i.e. clockwise) so that the y-axis was aligned with the bathymetry, oriented down-estuary.

2.2 Data Sources

In this section the various data sources used in the experiment are outlined, with particular emphasis on those employed in this thesis (moorings and shore-based photogrammetry).

2.2.1 Moorings

Eleven moorings were deployed for the experiment, titled *M01* through *M11*, with the first nine deployed near Île aux Lièvres in the "dissipation" zone, inshore of the 40 m isobath. See Figure 2.1 and Table 2.1 for mooring locations, water depths, instrument heights, and sampling parameters. Most of the moorings contained single instruments, with the exception of *M05*, *M07*, *M08*, and *M11*. *M05*, *M07*, and *M08* were multi-instrument "pods", including upward- and downward-looking acoustic Doppler profilers (ADPs) and turbulence resolving acoustic Doppler velocimeters (ADVs). *M08* also included a chain of temperature depth recorders (TDRs), attached to the anchor line. *M11* contained an upward-looking ADP (mounted to a streamlined underwater buoyancy system, or SUBS), with an S_4 electromagnetic current meter below.

The ADV at *M02* malfunctioned, and no usable data were retrieved. Also, due to a configuration error, the ADP at *M08* profiled only to a distance of about 12 m above the bottom (in 33 m of water), and the data were mostly excluded from the following analysis.

A sectional view of the mooring array is shown in Figure 2.2, highlighting the spatial coverage in both the x and z directions. The location of ADP bins and the nominal TDR locations at *M08* are indicated (note that at times the TDR chain leaned up to 80° from the vertical, discussed further in Section 3.4.2). The horizontal line at ~ 17 m corresponds to the mean pycnocline, as determined in Section 3.4.1.

2.2.2 Ship-Based Sampling

Four vessels were used throughout the experiment for data collection and mooring deployment and recovery.

The *RV Coriolis II* was used during the beginning and end of the experiment to deploy most of the deeper moorings (*M05* through *M11*), and to carry out a CTD

Name	**Lon (deg)**	**Lat (deg)**	x **(m)**	y **(m)**	Δxy **(m)**	**Sensor**	**Mfr**	**Freq**	δt **(s)**	δz **(m)**	**FB (m)**	**Bins**	**HAB (m)**	**Water Depth (m)**
M01	−69.71913	47.87672	−208	34	1	TDR	RBR	NA	1	NA	NA	NA	0.20	2.0
M02	−69.71977	47.87700	−265	35	5	Vector	Nortek	6 MHz	0.25	NA	0.15	1	0.97	3.0
M03	−69.72146	47.87844	−457	106	8	ADV	Sontek	10 MHz	0.1667	NA	0.1	1	0.82	6.7
M04	−69.72485	47.87799	−646	−69	48	ADCP	RDI	1200 kHz	10	0.5	0.44	25	0.40	11.9
M05	−69.72533	47.87943	−761	49	29	ADP ADV Vector Aquadopp	Sontek Sontek Nortek Nortek	1.5 MHz 10 MHz 6 MHz 2 MHz	20 0.1 0.125 10	1 NA NA 0.04	0.8 0.1 0.15 0.05	40 1 1 25	0.86 0.65 0.98 1.05	18.3
M06	−69.72321	47.88200	−775	376	27	ADCP	RDI	600 kHz	10	1	0.88	29	0.40	20.5
M07	−69.72706	47.87961	−881	−1	27	ADCP Vector PCADP	RDI Nortek Sontek	1200kHz 6 MHz 1.5 MHz	10 0.125 10	0.5 NA 0.04	0.44 0.15 0.05	35 1 32	0.97 0.37 1.08	23.3
M08	−69.72986	47.88077	−1127	−1	36	ADP ADV Vector TDR chain	Sontek Sontek Nortek RBR	1.5 MHz 10 MHz 6 MHz NA	20 0.1 0.125 1	1 NA NA NA	0.8 0.1 0.15 NA	40 1 1 NA	0.45 0.58 0.98 (...)	32.9
M09	−69.73433	47.88126	−1440	−128	100	ADCP	RDI	600 KHz	10	0.5	0.88	84	0.57	39.7
M10	−69.76060	47.89208	−3742	−126	25	ADCP	RDI	300 kHz	10	1	1.76	70	10.0	67.6
M11	−69.77571	47.89750	−5019	−201	25	ADCP S_4	RDI IO	300 kHz NA	10 60	1 NA	1.76 NA	35 1	31.9 9.5	84.5

Table 2.1: Moorings and instruments from the 2008 field program. The x and y positions are with respect to axes centred at 47° 52.529′ N; 69° 43.019′ W, with the x-axis rotated 31.5 degrees clockwise from East. "ADV" refers to acoustic Doppler velocimeters (including units called "ADV" manufactured by Sontek and called "Vector" manufactured by Nortek), "ADP" refers to acoustic Doppler profilers (called "ADP" by Sontek, "ADCP" by Teledyne RDI, "PCADCP" by Sontek, and "Aquadopp" by Nortek), "TDR" refers to temperature-depth recorders manufactured by RBR, and "S_4" refers to S_4 current meter manufactured by InterOcean. The TDR chain at mooring *M08* consisted of 7 units separated by a spacing of $\sim 4\,\mathrm{m}$.

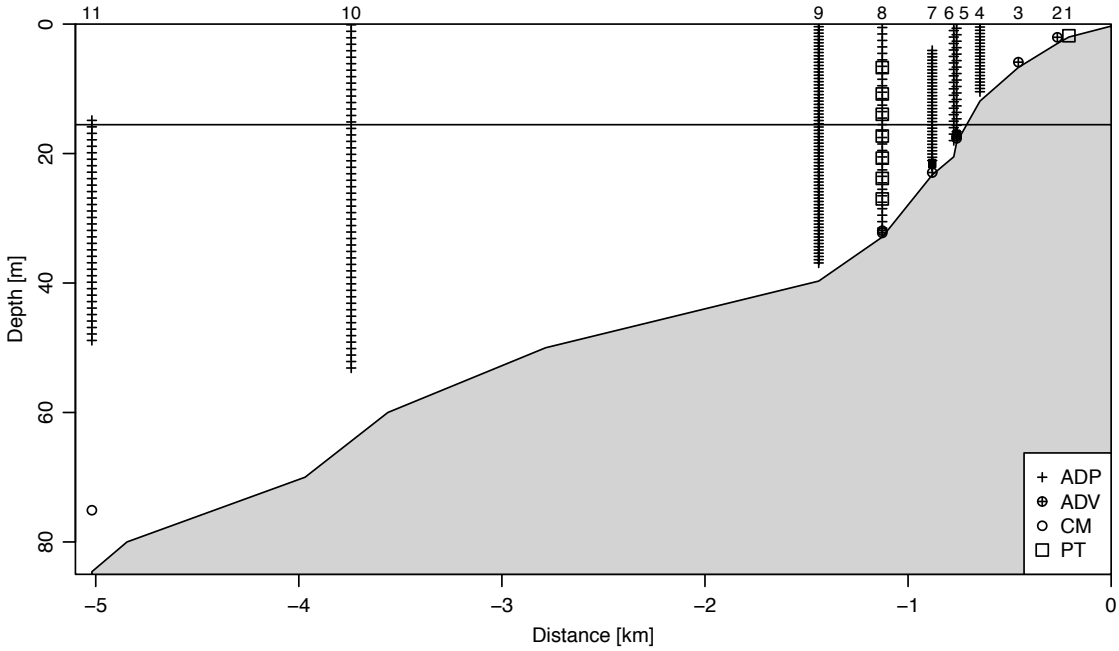

Figure 2.2: Side view of mooring instrument coverage. The horizontal line marks the centre of the statistical pycnocline. Labels at the top indicate mooring number. In the list of symbols, ADP stands for acoustic-Doppler profiler, ADV stands for acoustic Doppler velocimeter, CM stands for current meter, and TDR stands for temperature-depth recorder. The solid squares at *M06* and *M07* represent downward-looking acoustic Doppler profilers that cover a metre of water at centimetre-scale resolution. *M05* and *M06* nearly overlap in this, the x coordinate, but are separated by about 300 m (see Figure 2.1). The ADV at *M02* recorded for under a tidal cycle, and was recovered in a damaged state, so its record was not used in the analysis.

survey of the region over about 24 hours. Also onboard was a 150 kHz vessel-mounted ADP, which was used during the latter part of the experiment to survey currents in the deep channel (not discussed here). As it had a relatively large draft (~ 6 m), the *RV Coriolis II* was unable to sample in shallow water near the dissipation array.

To make up for this, the *RV Lampsilis* was used during the experiment as a platform for sampling near shore (~ 1 m draft). Instruments utilized on the *RV Lampsilis* were a vessel-mounted 1200 kHz ADP and a Seabird CTD. Typically the ship was anchored in shallow water near the mooring array, and sampling was carried out continuously for approximately 10 hours during the daytime only. The data from the *RV Lampsilis* will not be discussed here, but have been examined extensively by *Sutherland* (2009).

The *RV Merlu*, operated by Fisheries and Oceans Canada, was used for opportunistic sampling throughout the experiment. Equipped with a towed body containing a 200 kHz Biosonics echosounder and a 300 kHz ADP, the *RV Merlu* was used to run transects through the mooring array during wave shoaling events. From time to time, the *RV Merlu* was used for profiling using a small CTD.

Finally, the zodiac from the *RV Lampsilis* was used with a small CTD for profiling in very shallow water (less than 5 m). These data are not discussed here.

2.2.3 Shore-Based Photogrammetry

In the right conditions, internal waves have surface signatures as alternating dark and light bands (*Wang and Pawlowicz*, 2011). Shore-based photogrammetry has been successfully applied in the study region previously (*Bourgault and Kelley*, 2003), though never coincident with *in situ* data collection, as was the case during this field campaign. Two cameras were used, with their fields of view overlapped by a few degrees. The images were georectified with the method described by *Bourgault* (2008). Rectification parameters are presented in Table 2.2. Figure 2.3 shows an example image, from June 15 2008 (approximately 1 week prior to the experiment). Visible in the image are at least 5 groups of wave-like surface signatures, seen from time lapse animation to propagate in the direction indicated by the arrows. The 2008 field site is located to the north of the camera's field of view, which was obscured by trees in that direction. The rectangle around the field site indicates the region for which photogrammetry was used during the experiment (Section 6.3.3).

Images from Île aux Lièvres were collected at 45 s intervals on July 1, and 30 s intervals on July 2, from an elevation of 35 m. Poor weather conditions (rain, strong winds, and a choppy surface) prevented the use of photogrammetry on other days. Images were rectified using 30 ground control points collected using the *RV Merlu* within the region of the moorings. Image resolution was 3888×2592 pixels, leading to pixel dimensions (and hence position uncertainty) of less than 20 m for locations within 2 km of the camera.

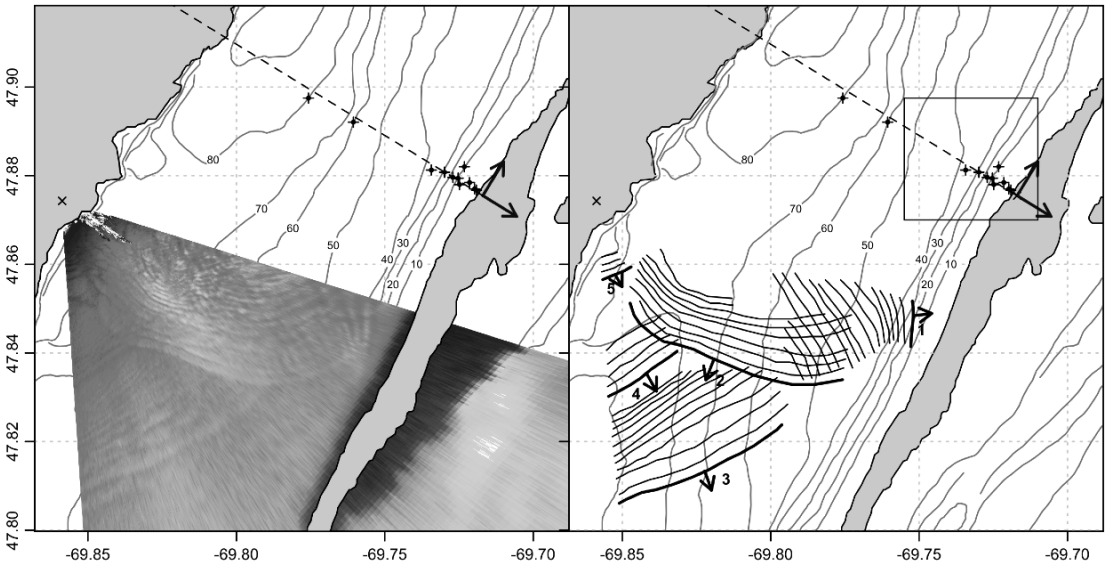

Figure 2.3: Sea-surface patterns observed on June 15 2008 13:47:09 UTC (during the flood phase of the tide, ~ 2 hours after low water) from a location ($\times$) on the Northern shore (47° 52.4580′ N; 69° 51.522′ W). The camera elevation was 308 m. Several distinct groups of internal waves can be identified, moving in different directions. The waves in group "1" can be seen to be approaching Île aux Lièvres, and refracting as they shoal. The box around the field site indicates the region within which shore-based photography was used during the experiment.

Date (2008)	Start (UTC) End (UTC)	Δt (s)	FOV (deg)	H (m)	ϑ (deg)	λ (deg)	φ (deg)	n_{gcp}	Δ_{xy} (m)
June 15	13:47:09 16:01:09	60	68.7	308	218	63.0	−0.31	6	211
July 1	11:39:59	45	64.6	35.8	88.1	69.4	0.72	30	43
	19:25:44		70.1	37.3	28.8	61.9	−0.54	36	35
July 2	11:55:00	30	70.4	39.8	92.5	62.5	−0.63	30	51
	20:40:00		66.0	32.9	27.2	68.8	0.19	33	37

Table 2.2: Parameters related to the georectification of shore-based photographs, determined using the technique of *Bourgault* (2008). Here, Δt is the time between successive photographs, FOV is the horizontal field of view in degrees, H is the camera altitude above sea-level, ϑ is the view angle of the camera counterclockwise from true North, λ is the angle above the vertical, φ is the clockwise tilt, n_{gcp} is the number of ground-control points used, and Δ_{xy} is the rms uncertainty in pixel location.

2.3 Data Processing

Orientations

Data from each Doppler current meter were collected and stored in either beam or XYZ (instrument) coordinates. Conversion from beam or XYZ velocities to geographical velocities (ENU, or East-North-Up) was done following the method given in Appendix A, after removing near-surface bins contaminated by sidelobe reflection. Prior to the conversion, it was necessary to perform some pre-processing to obtain sensible estimates of instrument heading, pitch, and roll.

Several of the instruments on the multi-instrument pods (*M05*, *M07*, and *M08*) either did not contain compass and tilt sensors, or the compass calibrations failed for an undetermined reason. In such cases, alignment of each instrument was based on position on the mooring frame, relative to an instrument for which the orientation was known. Alignment in this manner is likely only accurate to a few degrees, owing to the uncertainty of visually aligning instruments on deck. The compass and tilt sensor for the *M03* ADV malfunctioned in such a way that it returned reliable data only a fraction of the time, with the missing values replaced by zeros. In this case statistical analysis was used to recover the orientation angles, by examining histograms of the data and trimming values different from the peaks by more than a few degrees.

The alignment was verified by plotting horizontal velocity variance ellipses for the low-pass filtered currents, determined with eigenanalysis of u and v (see e.g. *Marsden*, 1999). It was determined in this way that the three pod moorings required an additional heading correction to align the mean currents with the other moorings. The reasons for the errors in the headings are unknown, as each of the compasses were oriented differently on the frames. The erroneous readings were possibly a result of magnetic interference from the steel frames, however, no systematic correction was discovered. In addition, it was discovered that the Sontek ADV at *M05* required a further correction for alignment with the Nortek Vector, most likely due to alignment uncertainty on the frame.

The corrected velocity variance ellipses for each acoustic current meter are summarized in Figure 2.4. Note the tidal dependence, and the consistent alignment relative to the isobath orientation (Figure 2.1). It is worth noting that following

the re-alignment, the high-frequency events displayed consistent patterns among instruments, confirming the validity of the rotation based on tidal currents.

ADP Bin Mapping

Acoustic Doppler profilers use a multiple beam configuration to measure the three dimensional water velocities averaged into depth bins, centred along the axis of the instrument (see e.g. *RD Instruments*, 1996). The beams angles are therefore referenced relative to the vertical, and thus the velocity estimate for a single bin actually incorporates beam velocity measurements from different horizontal locations. To combine the beam velocities to determine XYZ (and ultimately ENU) velocities, an assumption of horizontal homogeneity of the current is invoked. In many cases in the ocean this assumption may be valid, especially over long time scales. The situation is complicated, however, when the instrument is tilted (i.e. with non-zero pitch and/or roll), as in this case bins which are the same distance from the transducer will not be on constant geopotential surfaces. In the presence of vertical velocity shear, the bins may record very different velocities, resulting in a poor estimate of the transformed velocity. In the case of RDI ADCPs, on-board firmware can implement a "bin-mapping" algorithm, which identifies bins which are nominally horizontal based on the measured pitch and roll, and combines them to produce orthogonal velocities (*RD Instruments*, 1997).

This issue has been discussed in the literature, where it has been noted that the bin-mapping as implemented by RDI is unsuitable in many situations as it both duplicates and discards data from some bins, depending on the tilt and the ADCP parameters (*Ott*, 2002). In predominantly horizontal flows, it is therefore preferable to interpolate the beam velocities prior to combining vertical levels and transforming to an orthogonal coordinate system.

For flow that may contain high-frequency and large amplitude events (such as internal waves), or for which the mean current may not be along geopotential surfaces (e.g. in the presence of a sloping bottom), the situation is more complicated. Several authors have proposed solutions to the former (*Marsden and Ingram*, 2004; *Scotti et al.*, 2005). For the latter, especially when there is significant variability in the flow (e.g. due to tidal currents), it is unclear which surface should be used for aligning bins. Mostly likely, the mean flow will at times be along geopotential surfaces, and

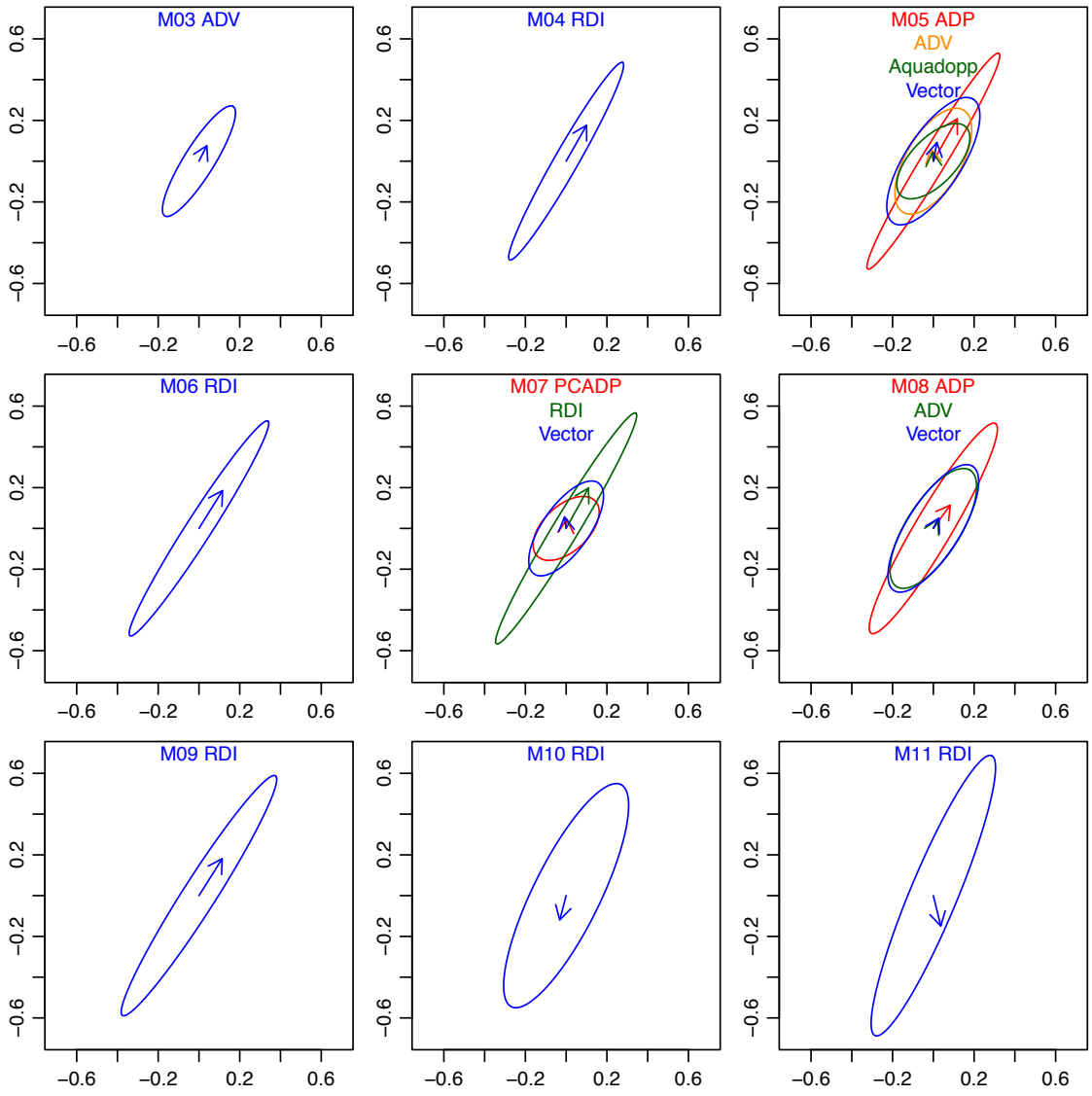

Figure 2.4: Velocity variance ellipses for all current meters, after heading corrections. The ellipse shows the results of the eigenanalysis, and the arrows indicate the time mean currents.

at times be parallel to the sloped bottom, over some length scale related to the slope angle.

Untangling all of the above issues is a difficult task. Tests using a bin mapping procedure similar to that proposed by *Ott* (2002) produced qualitatively improved velocities some of the time, but without knowing the "true" three dimensional velocity, it was difficult to assess if there was any quantitative improvement. One complication of the bin mapping is that data near the bottom and top of the profiles are discarded from some of the beams (due to there being no bins with which to map), and thus coverage of the water column is decreased. For a small to moderate tilt (e.g. about 5°), this may only amount to a few metres. However, in shallow water as much as 25% of the water column is unsampled after near-surface bins have been discarded based on side-lobe reflection. For these reasons, bin mapping algorithms were not applied to the data used in this thesis. Future processing techniques, perhaps involving data-assimilative methods for the waves and the background flow, may enable better estimates of velocities in such situations.

2.4 Summary

In this chapter, the SLEIWEX 2008 experiment and field site was introduced. Data sources included moorings, ship-based sampling, and shore-based photogrammetry, all of which are used in this thesis to varying degrees.

An overview of the data processing applied to the moorings was presented, with an emphasis on recovering best estimates of the instrument orientations. The current meters from several moorings required alignment based on mean velocity variances as compared with other instruments.

Corrections for tilted ADPs sampling in shear flows were discussed, highlighting the issues involved with the bin mapping corrections proposed by the manufacturer and in the literature. For the reasons outlined, no bin mapping was applied to the mooring data.

Chapter 3

SLEIWEX 2008 Background Conditions

In this chapter, the relevant background conditions from the SLEIWEX 2008 experiment will be reviewed. This is necessary to characterize the context of the physical setting within which internal waves are observed, and also to develop some of the fields that will be used in later analysis.

3.1 Meteorology

Meteorological data (wind speed and direction) were obtained from a station on Île Rouge (see Figure 2.1), a small treeless island about 25 km Northeast from the field site. The Île Rouge station lacked air temperature measurements for the period of interest, so these were obtained from Rivière-du-Loup, about 15 km to the Southeast.

Winds during the experiment were mostly aligned along the estuary, with primarily up-estuary winds until June 30, at which point they reversed. Hourly speeds during the up-estuary winds were about 7 m/s between June 28 and 30, with weak winds for several days before and after this time. On July 2, mean wind speed increased to about 8 m/s, this time oriented down-estuary.

While wind stress driven turbulence and surface heat flux are potentially important to the estuarine dynamics overall, the relevant data were not collected as part of the experiment. Scaling arguments suggest that even in strong winds (10 m/s) the local effect on the rate of change of kinetic energy in the flow (i.e. surface stress driven turbulence) will be small compared to bottom stress from tidal currents

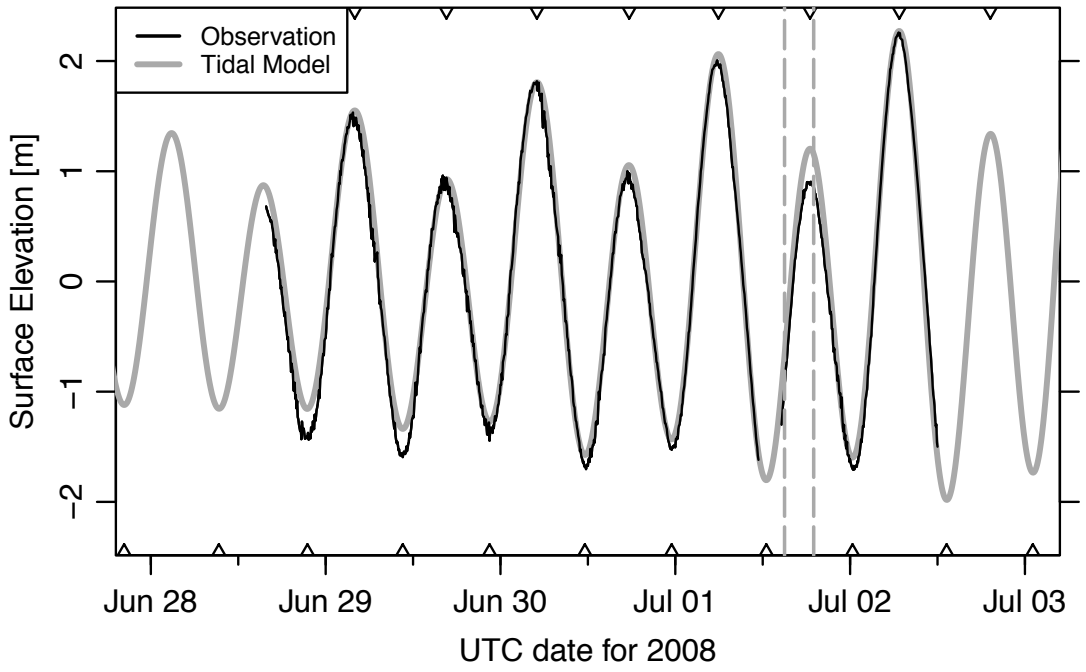

Figure 3.1: Tidal signal through the sampling period. The solid line is sea-level elevation about the mean, determined from a temperature-depth sensor at *M01*. The break in the line on July 1 indicates a time when the tide was low enough for the instrument to break the sea surface. The gray line is from the WebTide tidal model (*DFO*, 2009) at a nearby location, with amplitude and tidal lag adjusted to match the observations. Low- and high-water times are indicated along the axes, the vertical dashed lines indicate a period of focus discussed in the text.

(approximately 1%). It is possible that wind forcing may have had an influence on the variability in the observed density structure throughout the experiment, through straining of the along-channel density gradient (*Scully et al.*, 2005). For this experiment, however, it was taken to be sufficient to simply describe the variability, as it relates to other observed signals (e.g. internal waves).

3.2 Tides

Tides at the field site consisted of a mixed diurnal/semidiurnal tide. Sampling began about halfway through the neap cycle, progressing toward the maximum spring tide. The tidal range was about 2 m during neap tides, increasing to 4 m during spring tides. Instantaneous currents reached ~ 3 m/s near the surface in some locations, as a result of the high tidal range and the superposition of the estuarine circulation.

The tidal excursion was calculated to be about 5 km.

To construct a "tidal clock" for use in analysis, the pressure measurements from all sensors were combined and fitted using a smoothing spline that eliminated features lasting less than about two hours. From this signal, tidal phase (in radians) is calculated using

$$\phi(t) = \tan^{-1}\left(\frac{2\pi}{\tau_{M_2}}\frac{p_n}{\partial p_n/\partial t}\right), \tag{3.1}$$

where p_n is the demeaned pressure from the spline, $\partial p_n/\partial t$ is its time derivative, and τ_{M_2} is the M_2 tidal period. The phase ϕ is defined by $p(t) \propto \sin(\phi)$, so that $\phi = 0$ corresponds to the maximum rising tide and $\phi = \pm\pi$ corresponds to the maximum falling tide. Low water occurs at $\phi = -\pi/2$ and high water at $+\pi/2$.

3.3 Currents and Shear

3.3.1 Time-Averaged Currents

Time-averaged currents were calculated for each of the moorings containing an ADP, with the exception of *M08*. The results for along- and across-channel currents are presented in Figure 3.2, as a function of depth (instead of height above bottom), determined by the pressure measured by each instrument. Some ADP bins nearest to the surface and bottom have been removed from the calculation, due to the changing surface elevation.

Time-averaged along-channel currents near the island (*M03* to *M09*) are everywhere positive (i.e. downstream). This is expected given the depth of the channel on the Northern shore, where the subsurface upstream estuarine flow is concentrated, consistent with general conceptual models of estuaries (*Fischer et al.*, 1979) and other studies of this particular area (*Saucier and Chassé*, 2000). Mean currents at *M10* and *M11* (in ~ 60 and 80 m of water respectively) show a flow reversal at depth.

Across-channel currents are generally small (< 0.05 m/s), except in the deep moorings (*M10* and *M11*), which both exhibit mean across-channel flow, away from the Northern coastline (see Figure 2.1).

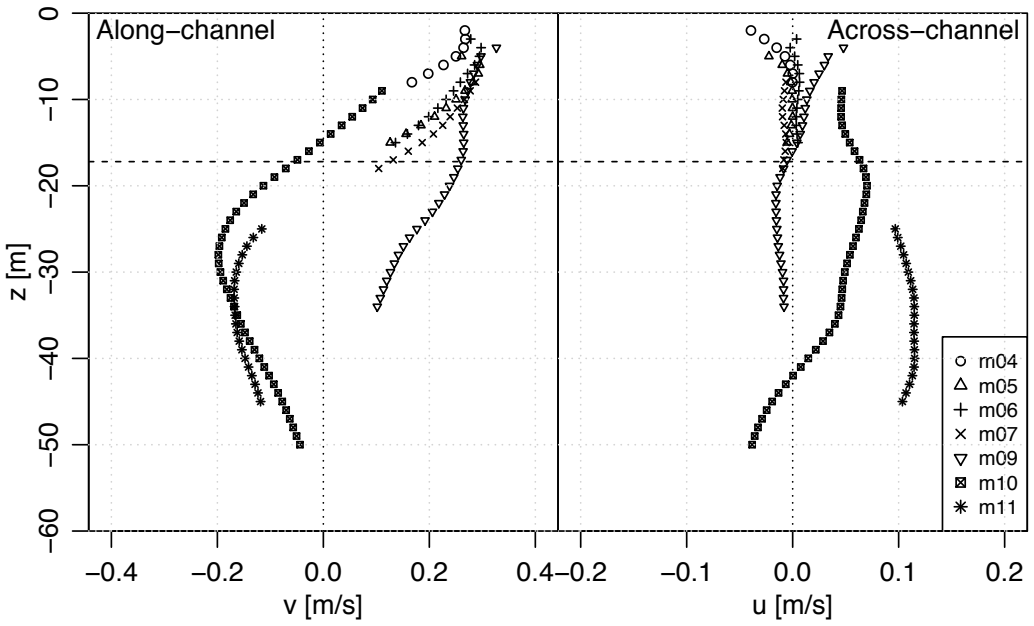

Figure 3.2: Time-averaged along- and across-channel currents from the ADPs. The dashed horizontal line indicates the mean pycnocline, as determined in Section 3.4.1.

3.3.2 Phase-Averaged Currents

Phase-averaged currents and the magnitude of the vertical shear for *M07* and *M09* are presented in Figures 3.3 and 3.4. The phase averaged shear magnitude was calculated as

$$\langle \mathcal{S} \rangle_\phi = \left\langle \sqrt{\left(\frac{\partial u}{\partial z}\right)^2 + \left(\frac{\partial v}{\partial z}\right)^2}^2 \right\rangle_\phi , \tag{3.2}$$

where (u, v) are across- and along-shore currents (corresponding to the x and y axes) and $\langle . \rangle_\phi$ represents an average across tidal phase. For each M_2 cycle the velocities were interpolated to a common phase based on Equation 3.1, and were then averaged over across tidal cycles.

Phase-averaged currents are dominated by the tidal flow (Figure 3.2), and so only the y-component is presented here. Average tidal currents reach $\pm 1.5\,\mathrm{m/s}$, with some vertical structure throughout the tidal cycle. Vertical shear during the falling tide at *M07* is dominated by near-bottom shear ($\sim 0.15\,\mathrm{s}^{-1}$), but there is some evidence of a near-surface shear layer as well. At *M09*, there is enhanced bottom and mid-water column shear during the falling tide . The ebb to flood transition for both locations tends to occur first at depth, leading to enhanced shear at mid-depth. Averaged over

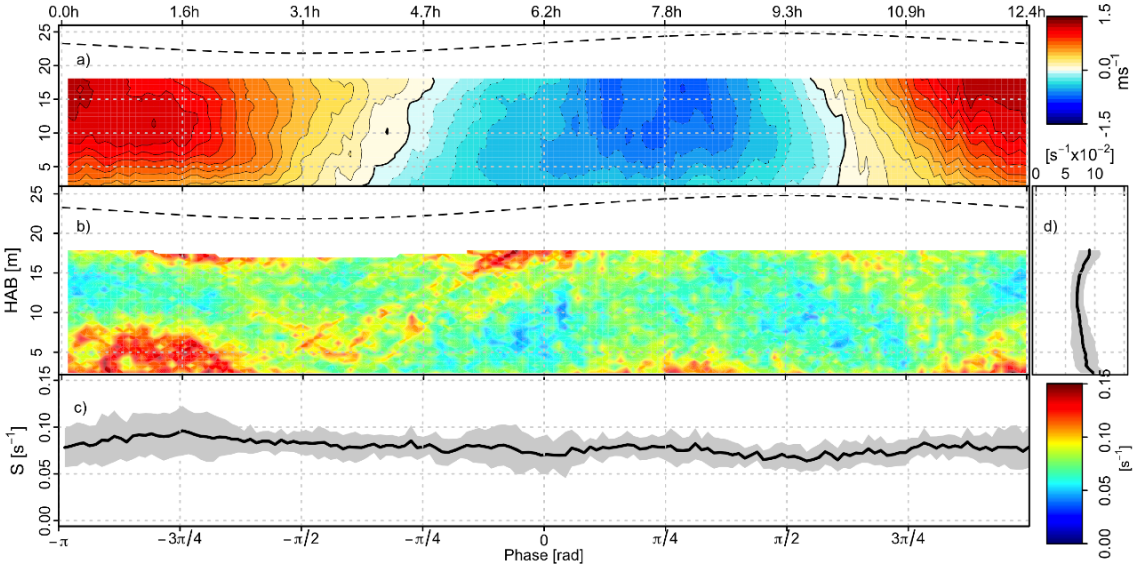

Figure 3.3: *M07* phase averaged a) alongshore current, b) vertical shear magnitude, c) depth averaged shear, and d) average shear profile. A phase of $\phi = 0$ corresponds to maximum flood, while $\phi = \pm\pi$ corresponds to maximum ebb. The dashed line in a) and b) is the location of the surface. The contour interval in a) is 0.1 m/s, and zero is indicated by the thick line. For the depth- and time-averaged shear in c) and d) the shaded regions represent the average shear ± the standard deviation. The times along the upper axis indicate hours in the M_2 tide.

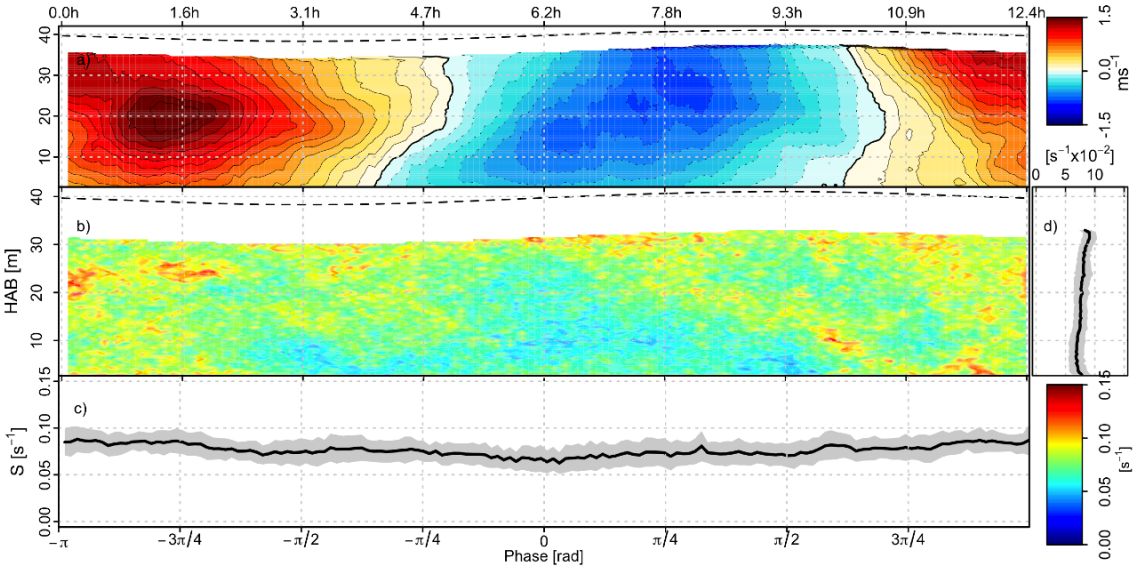

Figure 3.4: *M09* phase averaged currents and shear. Same as for 3.3

all phases and depths, there is a background shear of approximately $0.07\,\mathrm{s}^{-1}$.

3.4 Hydrography

Hydrographic data for the SLEIWEX 2008 experiment were obtained from two sources: a CTD survey performed from the *RV Coriolis II*, and the chain of TDR sensors at *M08*. This section outlines the techniques used to determine the mean and time varying water density structure for the field site.

3.4.1 CTD Survey

The temperature-salinity relationship is shown in Figure 3.5, inferred from the CTD survey carried out with the *RV Coriolis II* over a 30-hour period in the region. There is a tight relationship between T and S. Most of the recording instruments sampled T but not S, so a regression relationship $S = S(T)$ was developed to infer salinity from temperature. Trials with different polynomial fitting functions led to the choice of a 4th order polynomial of the form

$$S(T) = a_1 + a_2 T + a_3 T^2 + a_4 T^4, \tag{3.3}$$

where S is in practical salinity units and T is in °C. Equation 3.3 was fitted to the data using a nonlinear least-squares technique[1], and coefficients were found to be: $a_1 = 32.25$, $a_2 = -0.6897\,^\circ\mathrm{C}^{-1}$, $a_3 = -0.1068\,^\circ\mathrm{C}^{-2}$, and $a_4 = 3.226 \times 10^{-4}\,^\circ\mathrm{C}^{-4}$ (residual standard error 0.179 on 53446 degrees of freedom; $R^2 = 0.9981$; $p < 2\times10^{-16}$ overall and for each term). The small standard error (approximately 1% or 0.2 PSU) indicates that there is a right TS relationship at the SLEIWEX field site.

Figure 3.5 also shows the mean density profile inferred from the CTD survey. The measurements were fitted to

$$\sigma_\theta = b_1 + b_2 z + b_3 \tanh\left(\frac{z - b_4}{b_5}\right) \tag{3.4}$$

using a nonlinear least-squares technique[2], yielding residual standard error $1.3\,\mathrm{kg/m}^3$

[1] Fitting was performed using the `nls()` function in the `R` language (*R Development Core Team*, 2012)

[2] Various similar trial functions were tested. For more detail on the various functional forms see Section 3.4.2. The fit to a linear and hyperbolic tangent was almost identical to that from an exponential and hyperbolic tangent, so the simpler form was used here.

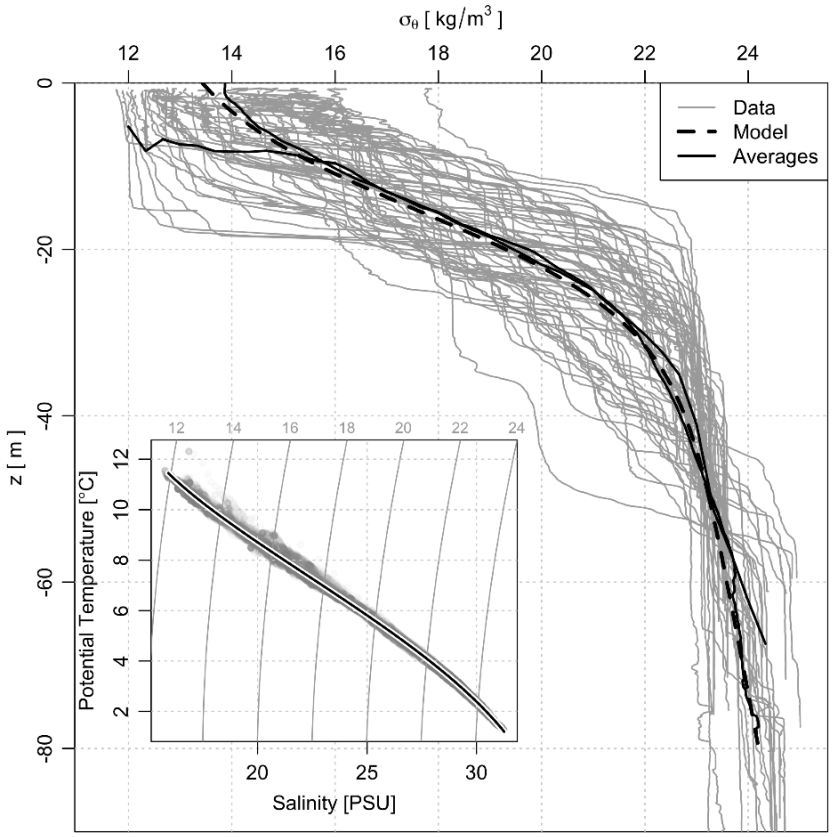

Figure 3.5: Vertical density structure in region, as indicated by a CTD survey spanning the domain indicated in Figure 2.1 and covering June 25 through June 26 2008. Gray lines indicate measured profiles, while the dashed black line is the result of a least-squares fit to a stratification model (see text), and the two solid black lines result from forming the mean density at depth, and mean depth at density. Inset is the temperature-salinity relationship. Measurements are indicated with semi-transparent dots, and the curve represents a least-squares curve fit.

on $> 5 \times 10^4$ degrees of freedom; $p < 2 \times 10^{-22}$ for each b coefficient. The resulting standard residual of $1.3\,\mathrm{kg/m^3}$ represents approximately 10% of the range of σ_θ. Values for the coefficients in the fit are: $b_1 = 17.21\,\mathrm{kg/m^3}$, $b_2 = -0.03024\,\mathrm{kg/m^4}$, $b_3 = -4.572\,\mathrm{kg/m^3}$, $b_4 = -15.54\,\mathrm{m}$, and $b_5 = 13.20\,\mathrm{m}$.

Using this relationship, a representative value of buoyancy frequency at the centre of the pycnocline is $N_p = 0.060 \pm 0.002\,\mathrm{s^{-1}}$, where the $\pm$ value results from taking the standard errors in b_2, etc., as reported by the statistical procedure, and propagating them assuming independence (*JCGM*, 2008). This analytical form of the density profile yields smooth vertical gradients, from which internal wave modes may be calculated. It should be noted that this mean profile is likely over-smoothed, due to

spatial averaging, tidal aliasing, and high frequency heaving of isopycnals.

A rough calculation of the Richardson number $Ri = N^2/\mathcal{S}^2$ (using $N = 0.06\,\mathrm{s}^{-1}$ and $\mathcal{S} = 0.07\,\mathrm{s}^{-1}$) yields a value close to 3/4, which suggests that shear instabilities may be important in this region. A more detailed discussion of stability using time varying fields will be given in Section 3.6.

3.4.2 TDR Chain

The chain of 7 TDR sensors deployed at *M08* measured temperature and pressure at 1 Hz throughout the experiment, and was used to infer the time-varying vertical temperature (and density) structure. As a result of the strong currents, especially during the falling tide, drag on the line caused it to lean with the flow, at times as much as 80° from the vertical. During the slack and rising phases of the tide, the chain was close to vertical, with the topmost TDR attached just below a surface float. Spacing between the sensors was nominally $\sim 4\,\mathrm{m}$.

The temperature recorded by the TDRs was mapped to density using Equation 3.3, and the inferred density and depth measurements were averaged into bins of 10 minutes length. Temperature measurements from the other bottom mounted sensors deployed along the slope were similarly converted and averaged. To estimate the vertical structure over the entire water column, it was assumed that lateral variations were small, and thus the density measurements from all sensors could be combined.

Density estimates from each 10 minute period were fitted to a functional form using nonlinear least squares, in a similar manner to the mean CTD profile in Section 3.4.1. Three different functional forms were used, depending on the success of the nonlinear least squares fitting procedure, and are outlined below.

First, a combined tanh and exponential form was attempted, as

$$\sigma_{\theta 1} = d_1 + d_2(1 - e^{z/d_3}) + d_4 \tanh\left(\frac{z - d_5}{d_6}\right). \tag{3.5}$$

In general, this form was preferable to the other formulae, as it constrained the density at depths greater than 50 m to realistic values. If the tanh plus exponential failed, a combined tanh and linear form, identical to Equation 3.4 was tried, as

$$\sigma_{\theta 2} = d_1 + d_2 z + d_4 \tanh\left(\frac{z - d_5}{d_6}\right). \tag{3.6}$$

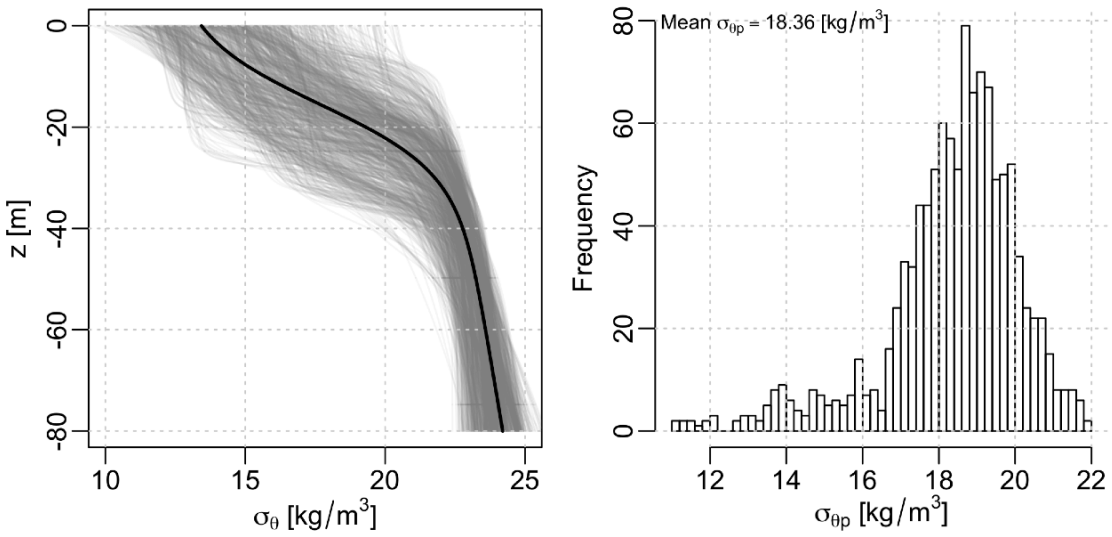

Figure 3.6: Results of the nonlinear fit to the TDR data. Left: composite of all fit profiles (gray lines). The mean density profile from Section 3.4.1 is indicated by the thick black line. Right: histogram of the value of σ_θ at the pycnocline (parameter d_5). The mean pycnocline σ_θ is 18.36 kg/m^3.

The final functional form that was attempted was a simple tanh form, as

$$\sigma_{\theta 3} = d_1 + d_4 \tanh\left(\frac{z - d_5}{d_6}\right). \tag{3.7}$$

Once a fit was obtained, the functional form allowed an extrapolation of the density field beyond the highest and lowest measurements.

Each of the 3 functional forms was attempted in turn. Starting values for the fit parameters were taken from the previous successful fit, and reasonable limits on the range of the parameters were applied. Failure to fit was determined by a failure of the nonlinear least squares algorithm to find a minimum with the given parameters. Of the entire time range between 2008-06-25 23:00:00 to 2008-07-03 18:00:00 UTC, only one profile failed to fit at least one of the three forms. A summary of all profiles, plotted with the mean profile from the CTD survey is shown in Figure 3.6 (left panel). The right panel shows a histogram of the density at the inferred pycnocline (parameter d_5), indicating a mean value of 18.36 kg/m^3.

The vertical density structure as a function of time is presented in Figure 3.7 (top panel), along with the squared buoyancy frequency N^2 (bottom panel). The nominal

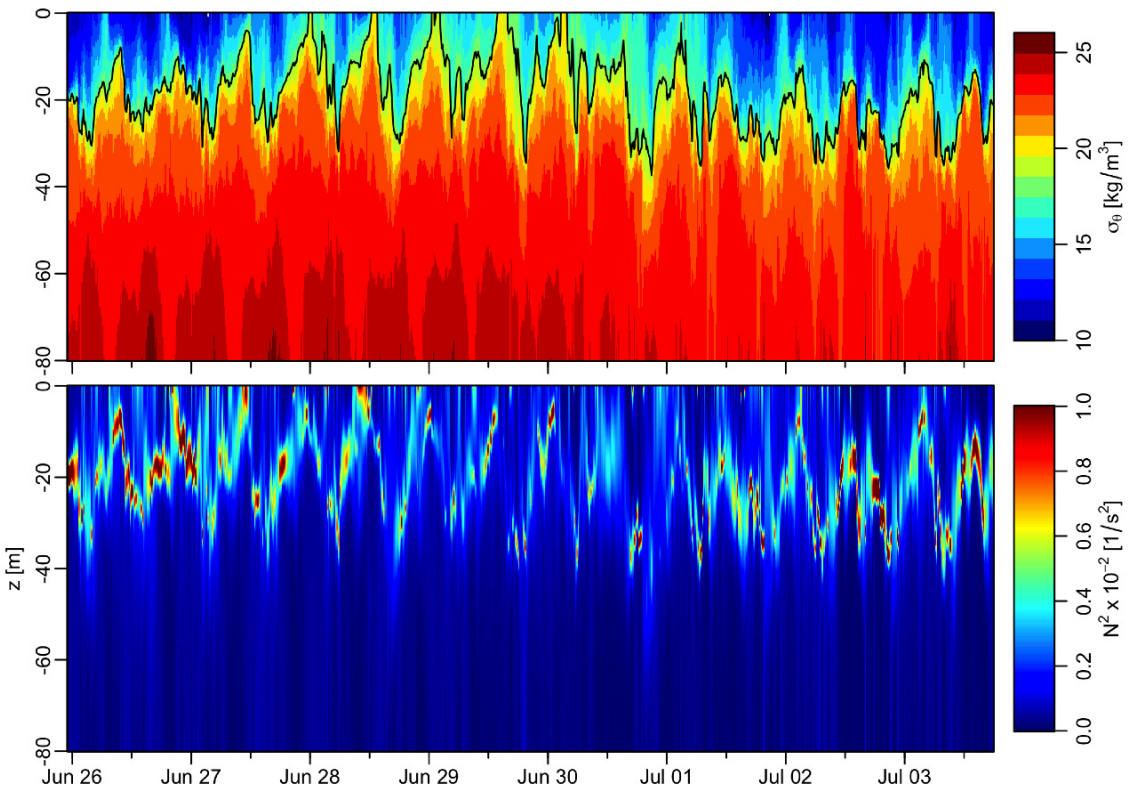

Figure 3.7: Depth-time variation of the density and buoyancy frequency. Top: σ_θ between 0 and -80 m. The solid black line highlights the 18.36 kg/m^3 isopycnal used to infer the pycnocline. Bottom: N^2 between 0 and -80 m.

pycnocline, as defined by the depth of the 18.36 kg/m^3 isopycnal, is indicated by the black line.

Figure 3.7 highlights the temporal variability of the density field, on both tidal and longer time scales. Comparing the middle portion of the experiment (2008-06-28 to 2008-07-01) with the beginning and end, it can be seen that the mean pycnocline depth is shallower. Despite the shallower pycnocline, the range of the pycnocline depth over a tidal period during the middle part of the experiment is larger. Stratification is also weaker during this period.

The cause of the sub-tidal variability in density is unclear. Possibilities include: wind-forcing, the neap/spring transition, and large-scale changes in estuarine circulation. The data necessary were not collected to permit tests of these or other scenarios. Future experiments may benefit from a broader perspective considering the large scale forcing on the local conditions.

3.5 Internal Waves

Internal waves were observed at the field site consistent with previous studies in the area (*Bourgault and Kelley*, 2003; *Bourgault et al.*, 2005, 2007; *Mirshak*, 2008; *Bourgault et al.*, 2008). As much of the rest of this thesis will focus on the details of the internal wave field, only a brief summary will be presented here.

3.5.1 Timing

Signals consistent with internal waves were observed in all moored instruments. Manual detection of internal waves was undertaken for the ADPs at *M05*, *M07*, and *M09*, using both the acoustic backscatter and the vertical velocity signal. Only waves with a maximum vertical speed larger than about 0.04 m/s were identified.

Figure 3.8 (left-hand side) shows a summary of wave events, plotted as a function of tidal phase, using a "phasor"-type plot, where the (tidal) pressure is plotted against its time derivative normalized using the M_2 period as in Equation 3.1. Individual wave events are indicated with dots, and the relative density of points is indicated by the colour scale. The highest density of events occurs during the rising tide ($\partial p/\partial t > 0$ and $p \sim 0$), consistent with previous observations in this region (*Bourgault and Kelley*, 2003; *Mirshak*, 2008). Wave events observed at *M05* and *M07* are distributed throughout the cycle more than at *M09*, possibly indicating wave fission during breaking – where one shoaling wave becomes a train of upslope propagating signals (see e.g. *Wallace and Wilkinson*, 1988; *Helfrich*, 1992).

The right-hand panels in Figure 3.8 indicate the number of observed events per M_2 tidal cycle. The overall pattern between moorings is similar, with fewer waves during the middle of the time period.

3.5.2 Wave Kinetic Energy Proxy

To construct a time series of internal-wave activity at each mooring, a proxy was devised for the kinetic energy density (per unit mass), based on the depth-averaged vertical velocity. In the presence of large background flow and shear, nonlinear high-frequency internal waves are more easily detected from the vertical velocity field than from the horizontal. The depth-averaged vertical wave velocity w_{iw} was calculated by applying a second-order forward-and-reverse band-pass Butterworth

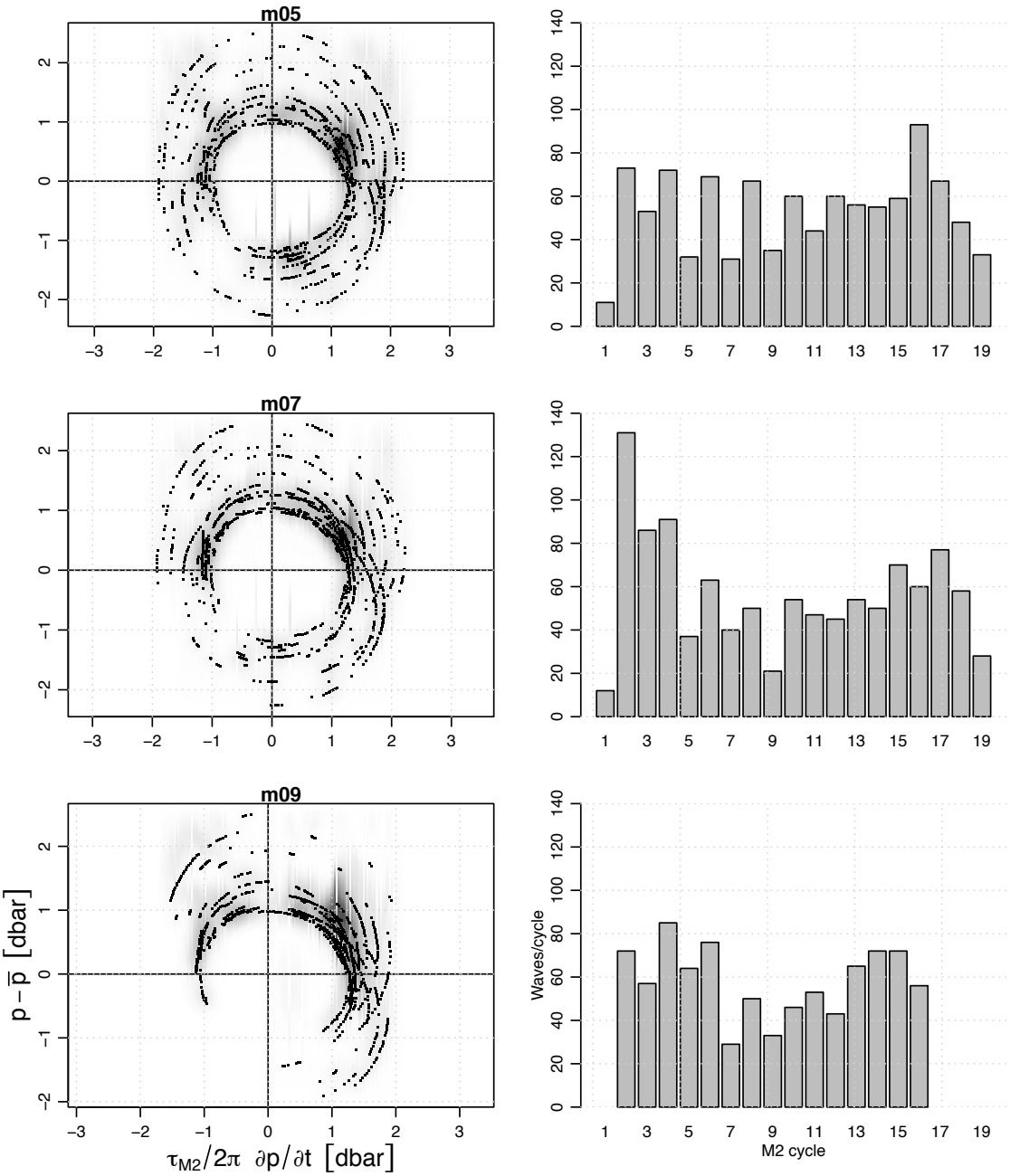

Figure 3.8: Observations of manually detected wave events. Left column: timing of waves in the M_2 cycle for each of *M05*, *M07*, *M09*. Dots indicate individual wave events, and the grey scale represents event density. Right column: number of observed waves per M_2 cycle.

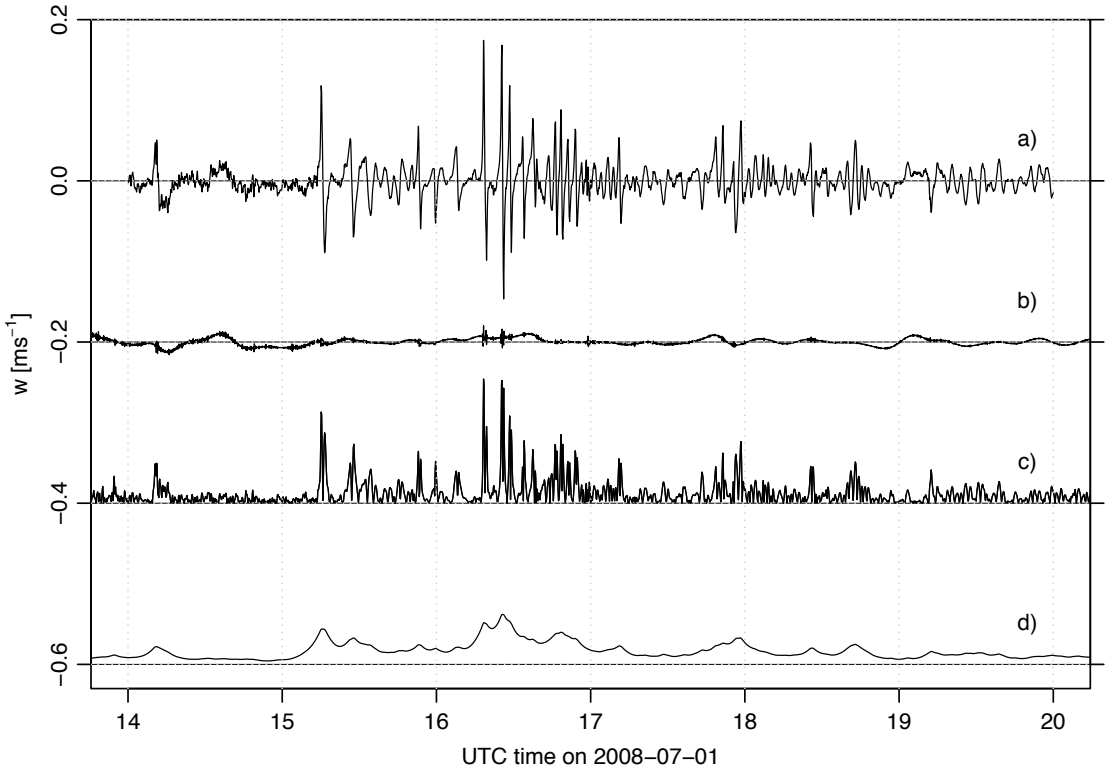

Figure 3.9: Demonstration of kinetic energy proxy for internal waves. a) Depth-averaged vertical component of velocity w inferred from ADP at *M07*, showing four hours on July 1. b) Portion of the signal that was removed using a band-pass butterworth filter of order 2, with cutoff frequencies of $10^{-1}N_p$ and $10^{1/2}N_p$. c) Band-passed wave vertical velocity w_{iw}, and d) envelope showing velocity corresponding to wave energy proxy $\sqrt{2KE_w}$.

filter, with 6 dB cutoff frequencies of $10^{-1}\,N_p$ and $10^{1/2}\,N_p$, where N_p is the average pycnocline buoyancy frequency (Section 3.4.1). The cutoff frequencies were chosen based on inspection of the filtered signal during times of internal waves. A proxy for internal wave kinetic energy density was then calculated as

$$KE_w = \frac{1}{2}\langle w_{iw}^2 \rangle_{lp}, \tag{3.8}$$

where $\langle . \rangle_{lp}$ is a low-pass filter with cutoff $10^{-1}\,N_p$. An example of the method for determining the wave kinetic energy proxy is presented in Figure 3.9, showing the depth-averaged vertical velocity (a), the high- and band-pass filtered vertical velocities (b and c), and the lowpass-filtered w corresponding to $\sqrt{2KE_w}$ (d).

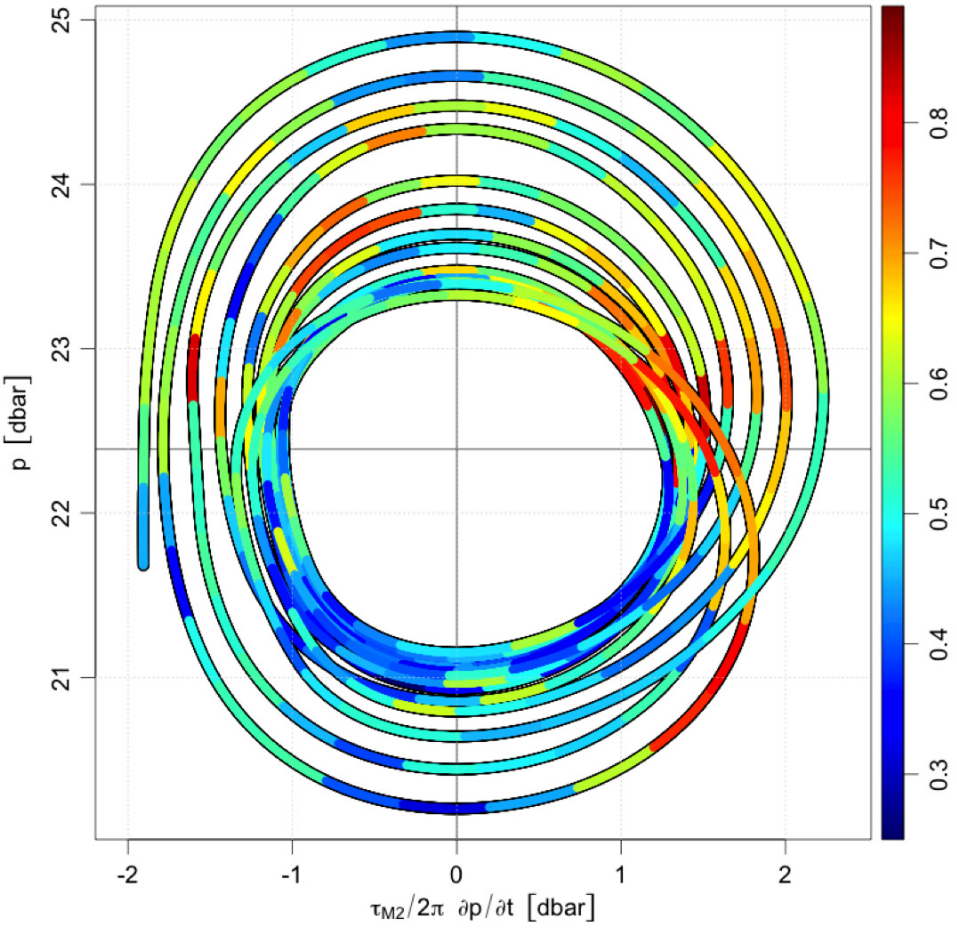

Figure 3.10: Wave energy proxy KE_w at *M07*. The axes are based on the pressure spline (as in Figure 3.8), with the multiplication by M_2 tidal period (divided by 2π) yielding a circular trace for a sinusoidal M_2 tide. The colors indicate the base-10 logarithm of wave energy proxy in J/kg, (scaled to lie between 0 and 1), averaged in 30 minute bands. Deep blue indicates low values and deep red indicates high values.

Internal wave energy at the field site was binned into 30 minute averages and plotted as a phasor (see Figure 3.10). Much of the internal-wave energy appears during the rising tide (on average twice as much as during the falling tide), suggesting either a tidal generation mechanism or tidal influences on the wave propagation. The phasor plot also highlights the temporal variability of the internal waves. In particular, KE_w during the highest tidal amplitudes is less intense, and there are indications of internal waves at other times, but they do not occur consistently on each tidal cycle.

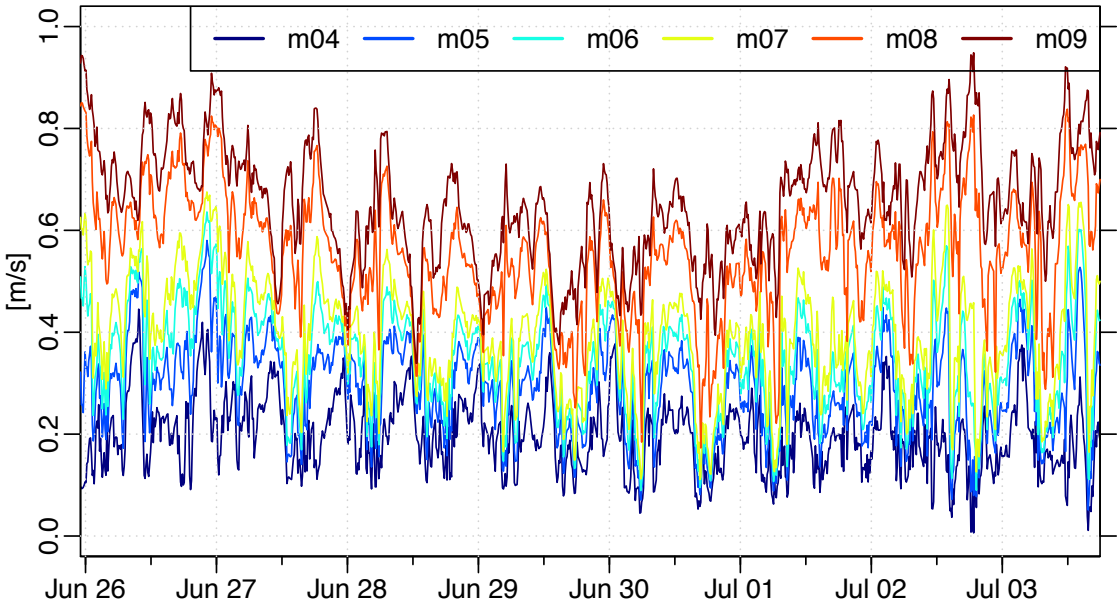

Figure 3.11: Mode-1 internal wave speeds, determined using the vertical density structure inferred from the TDR fitting procedure.

3.5.3 Baroclinic Wave Speeds

Using the time-varying vertical density structure determined in Section 3.4.2, the mode-1 baroclinic internal wave phase speeds were calculated at each mooring location. The mode-1 speeds were obtained from the vertical internal wave modes, calculated by solving the eigenvalue problem (*Gill*, 1982, Chapter 6.11):

$$\frac{d^2\Pi_n}{dz^2} + \frac{N^2}{c_n^2}\Pi_n = 0, \tag{3.9}$$

where N is the buoyancy frequency, Π_n is the vertical displacement (set to zero at the surface and the bottom), and c_n is the inferred horizontal phase speed of a given mode n.

Results are presented in Figure 3.11, for moorings *M04* to *M09*. There is a decrease in wave speed in the onshore direction, expected from the shoaling bottom. There is also an overall decrease during the middle portion of the experiment, consistent with the subtidal changes in the background density field discussed previously.

3.6 Shear Instabilities

In a stratified shear flow, the onset of instability can be described in terms of the Richardson number

$$Ri = \frac{N^2}{\mathcal{S}^2} \tag{3.10}$$

(*Miles*, 1961; *Kundu and Cohen*, 2002). Linear theory suggests that when Ri is ≤ 0.25 a stratified shear flow will be dynamically unstable, and may result in overturning and mixing (see e.g. *Gregg*, 1987). In field scenarios, this criterion can be difficult to apply, due at least in part to resolution limits of the instrumentation. The issue is further convoluted by spatial separation between density and velocity measurements, such as would occur with an ADCP and a vertically profiling CTD. Nevertheless, low values of Ri can still be used as a qualitative indicator of instability.

Bourgault et al. (2001) observed shear instabilities in the upper St. Lawrence Estuary, in the deep part of the channel near the SLEIWEX field site. The observed features took the form of Kelvin-Helmholtz (KH) instabilities, predicted to be forced by shear created when a near-bottom dense water mass flows up-estuary during flood tides.

While the KH instabilities observed by *Bourgault et al.* (2001) occurred in the deeper part of the channel to the North-West of the 2008 field site, similar features were observed in the 2008 mooring records in the shallower water on the slope. An example from *M09* is shown in Figure 3.12, with the first three panels displaying acoustic backscatter, along-channel velocity, and vertical velocity. The pattern is visible in the ADP velocities between 8:10 and 8:30 UTC, as a series of vertical bands. The backscatter shows a "braided" pattern, expected for a train of KH billows advected past a moored sensor.

The smoothed squared shear $\mathcal{S}^2$ and buoyancy frequency N^2 are shown in the bottom two panels. Shear has been normalized by a factor of 1/4, according to the linear stability criterion, to make comparison of magnitudes easier[3]. N^2 was determined from the fits to the TDR chain (e.g. Section 3.4.2). Much of the water column may be unstable during this time, a result of the large vertical shear during the falling tide.

[3]Note that $N^2/\mathcal{S}^2 < 0.25$ is a necessary, but not sufficient, condition for the formation of KH instabilities

To highlight locations where KH instabilities would be expected to form, regions where $Ri < 1$ and $N^2 > 0.001\,\mathrm{s}^{-1}$ (corresponding to a buoyancy period about half of the mean pycnocline buoyancy period) are contoured over the $\mathcal{S}^2$ and N^2 fields. The results indicate that much of the pycnocline region is unstable to shear instability during this time, supported by the observation of KH billows in the velocity record.

It should be noted that this result is crude, in that the separation in space of the velocity and density measurements (about 300 m) precludes an accurate assessment of water column stability. This argues against attempting to assess turbulence and mixing from these processes with the current measurements. It is, however, important to keep in mind that instabilities of this type may play an important role in mid-water column mixing in the St. Lawrence Estuary.

A further complication, as evidenced by the strong high-frequency velocity field associated with shear instabilities, is the overlap with the frequency band attributed to internal waves (periods of several minutes). It is likely that the wave proxy KE_w contains some signals actually associated with such instabilities, in addition to those resulting from propagating internal waves.

3.7 Summary

In this chapter the relevant background conditions during the SLEIWEX 2008 experiment were presented, highlighting the tidal dependence, variability in the currents and vertical shear, and the vertical density structure as inferred from the CTD survey and TDR chain. Temperature and salinity are found to have a tight relationship, allowing inference of one from the other.

The timing of the present observations of internal waves is consistent with previous studies in the region, with wave arrival predominantly during the rising tide. A proxy for internal waves was developed based on the depth averaged vertical velocity measured by an ADP. This proxy will be used throughout the thesis as an indication of internal wave activity.

The current meter record reveals high-frequency events believed to be Kelvin-Helmholtz shear instabilities. Such instabilities have been observed in the region previously, and a crude stability analysis supports this conclusion.

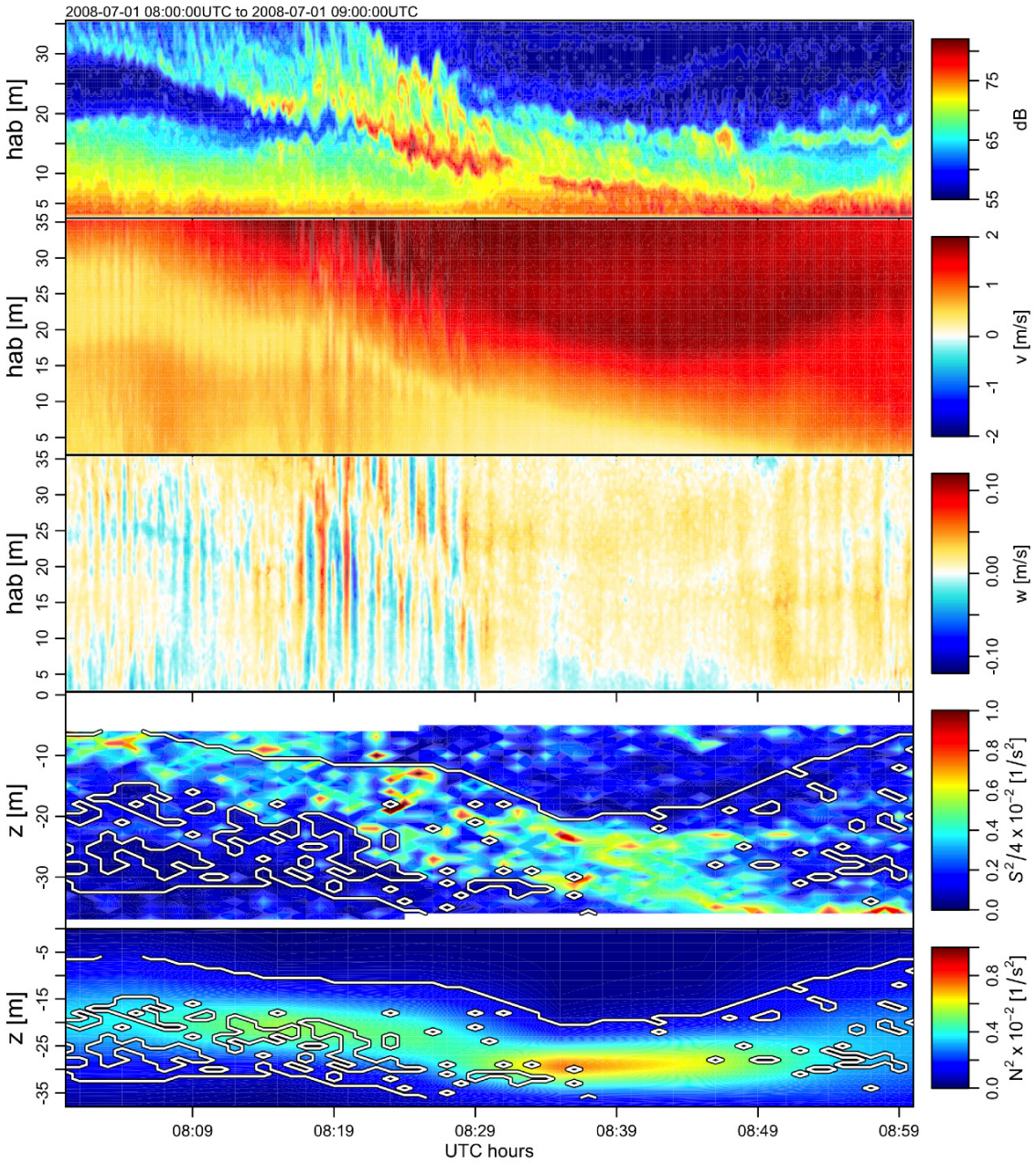

Figure 3.12: Observation of KH instabilities at *M09*. From the top: acoustic backscatter from the ADCP, along-channel velocity, vertical velocity, vertical shear squared ($\mathcal{S}^2$), and buoyancy frequency squared (N^2). The white contours in the bottom two panels highlight regions where $Ri < 1$ and $N^2 > 0.001\,\mathrm{s}^{-1}$.

Chapter 4

A Technique for Inferring Internal Wave Density Structure from a Moored Doppler Current Profiler

For high-frequency internal waves, measurements relating to energetics require knowledge of the vertical and horizontal structure of the perturbed density field. In numerical models this information is readily available. However in field measurements, obtaining the density field with sufficient temporal and spatial resolution presents many obstacles. Measurement of water properties must be performed *in situ*, and vertical profiling instruments such as CTDs remain the most common option for doing so.

For example, in the South China Sea, *Klymak et al.* (2006) sampled the water column using a custom-built fast CTD that could be cycled to 500 m depth every 6 minutes, sufficient for the resolution of the local internal waves, with periods of about 1 hour. On the New Jersey shelf, using a vertical microstructure profiler in about 60 m of water, *Shroyer et al.* (2010a) found that horizontal sampling through nonlinear internal waves (approximately 5 profiles per wave) was not sufficient to recover the heaved density field. To compensate, the horizontal amplitude structure of the wave was estimated from a shipboard echosounder and combined with an estimate of the vertical structure function, to infer the density field based on an upstream profile.

A similar method for estimating the heaved density field for internal waves was employed by *Moum and Smyth* (2006) (see also *Moum et al.*, 2007b; *Shroyer et al.*,

2009). The method involves using ADP velocity measurements to calculate the two-dimensional streamfunction for the flow, and then assuming that streamlines are parallel to isopycnals. The heaved density field may then be inferred using a single profile of the vertical structure upstream of the wave. The advantage to this approach is that it eliminates the effort involved in rapid vertical profiling, and that the density estimates are co-located and contemporaneous with the velocity estimates.

In this chapter, an extension to the streamfunction method used by *Moum and Smyth* (2006) is proposed. The new method, utilizing a relaxation scheme, will be shown to be resistant to noise and background velocity shear using test fields for a synthetic nonlinear internal wave. The method will then applied to data from the SLEIWEX 2008 experiment, to demonstrate the improvement over the method of *Moum and Smyth* (2006). This will establish the validity of the method for use in the energy measurements presented in Chapter 5.

4.1 Theory

Conservation of mass can be expressed as

$$\frac{D\rho}{Dt} + \rho\nabla \cdot \mathbf{u} = 0, \tag{4.1}$$

where $\frac{D}{Dt}$ is the material derivative, corresponding to the rate of change following a fluid element. In two-dimensional incompressible flow a streamfunction, ψ, can be defined by

$$u = \frac{\partial\psi}{\partial z}, \quad w = -\frac{\partial\psi}{\partial x}. \tag{4.2}$$

For the limiting case of a feature propagating at a constant speed c, and without change of form, one may write $\psi = \psi(x - ct)$, so that time derivatives can be replaced by spatial derivatives using

$$\frac{\partial}{\partial t} = -c\frac{\partial}{\partial x}. \tag{4.3}$$

Substituting Equations 4.2 and 4.3 into Equation 4.1 yields

$$(u - c)\frac{\partial\rho}{\partial x} + w\frac{\partial\rho}{\partial z} = 0 \tag{4.4}$$

and

$$\frac{\partial \psi}{\partial z} \Big/ \frac{\partial \psi}{\partial x} = \frac{\partial \rho}{\partial z} \Big/ \frac{\partial \rho}{\partial x} \,, \tag{4.5}$$

where the substitution $\frac{\partial \psi}{\partial z} = u - c$ has been made for the horizontal velocity in a frame of reference moving at constant speed c. The implication of Equation 4.5 is that in the wave frame of reference, isopycnals are parallel to streamlines. Therefore, an estimate of the density structure upstream of the wave can be extended along streamlines to give an estimate of the wave-heaved density structure within the wave.

4.2 The *Moum and Smyth* (2006) Method

In their paper discussing the various contributions to the pressure field associated with a nonlinear internal wave, *Moum and Smyth* (2006) make use of Equation 4.5 and calculate a streamfunction from their bottom mounted ADCP velocity records. Their procedure (abbreviated as MS) is as follows.

First the streamfunction is estimated by vertical integration of the horizontal velocity in a frame of reference moving with the wave

$$\psi_u(x,z) = \int_0^z (u(x,z') - c)\, dz',$$

where $x = -ct$. Next, another estimate of the streamfunction is created by integrating the vertical velocities using ψ_u as a boundary condition, yielding

$$\psi_{w_D}(x,z) = \psi_u(x_D,z) - \int_{x_D}^{x} w(x',z)\, dx'$$

and

$$\psi_{w_U}(x,z) = \psi_u(x_U,z) + \int_{x}^{x_U} w(x',z)\, dx',$$

where x_D and x_U are locations downstream and upstream of the wave. For a non-divergent field with no measurement errors, the three estimates would be the same. *Moum and Smyth* (2006) regard ψ_{w_D} and ψ_{w_U} as less reliable because they use ψ_u as a boundary condition, so they construct averages

$$\psi_w = 0.5(\psi_{w_D} + \psi_{w_U})$$

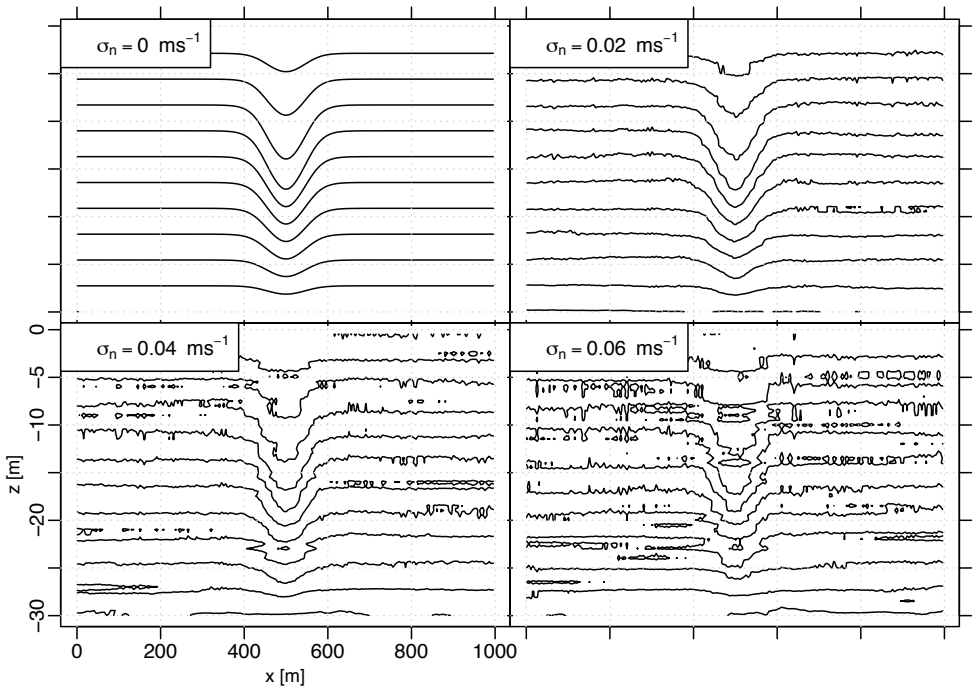

Figure 4.1: Streamfunction ψ from the MS technique for a synthetically generated internal solitary wave. Top: ψ solution with increasing amounts of Gaussian noise added. The standard deviation of the noise is indicated in the upper left corner of each panel. The amount of noise added to the w field was 1/5 that added to the u field (the approximate ratio of maximum velocities in each field), and was uncorrelated.

and

$$\psi_{MS} = 0.5(\psi_u + \psi_w). \tag{4.6}$$

Moum and Smyth (2006) find that velocity components derived from this streamfunction generally match measured velocities to within 2–3 cm/s.

4.2.1 Evaluation of the MS Method

The implementation of the MS technique, and its limitations, were explored using synthetic data of an internal solitary wave, generated using the model of *Stastna and Lamb* (2002) (Appendix B). The test data used here were for a wave in a constant depth of 30 m (the model cannot calculate waves for a sloped bottom), using a hyperbolic tangent density profile with an undisturbed pycnocline at $z = -10$ m and a wave amplitude of about 7 m.

Figure 4.1 highlights the sensitivity of the MS method when Gaussian noise

(uncorrelated in u and w) is added to the velocity fields, with the streamfunction appearing increasingly jagged as the standard deviation of the noise is increased (top panel).

Predictably, the estimate of ψ is adversely affected when various amounts of noise are added to a wave with a background shear field (Figure 4.2, top panel). The velocity profile used for the background was of the form

$$u_b(z) = \frac{\Delta u}{2} \tanh\left(\frac{z - z_{pyc}}{\delta z}\right), \tag{4.7}$$

where the shear layer depth z_{pyc} and width δz were chosen to match the density profile, and Δu is the total velocity difference between the upper and lower layers. The background velocity is prescribed as input to the wave model, and the resulting wave field is therefore slightly different for each value of Δu. In addition, the total velocity field is divergence-free. Tests using a background field for which $\nabla \cdot \mathbf{u} \neq 0$ (by extending Equation 4.7 along isopycnals) produced streamlines that differed markedly from the true field.

To assess the performance of the MS technique when moderate amounts of noise are present, the inferred streamfunction was used with Equation 4.2 to reconstruct the velocity fields (Figure 4.2, bottom panel). Although the inferred w-field shows reasonably good agreement (rms error of 0.01 m/s), the u-field associated with the wave is swamped by the noise in ψ (rms error of 0.21 m/s).

Initial tests using the MS technique with data from the SLEIWEX 2008 measurements brought into question the applicability of the technique in this domain. In particular, the ψ estimates appeared to be heavily influenced by noisy data, by background shear, and by divergence in the flow. The maximum velocities in the waves sampled by *Moum and Smyth* (2006) are approximately 5 times larger than the background flow, which is relatively uniform over the depth (see *Moum and Smyth*, 2006, their Figure 6).

This result is different from that observed by *Moum and Smyth* (2006) in their application, and indicates that one should be cautious when applying the technique to data which may contain noise or vertical shear of the horizontal current. Note that noise here may include any feature that introduces gradients to the velocity fields, beyond simply randomness in the flow or sampling errors from the ADP.

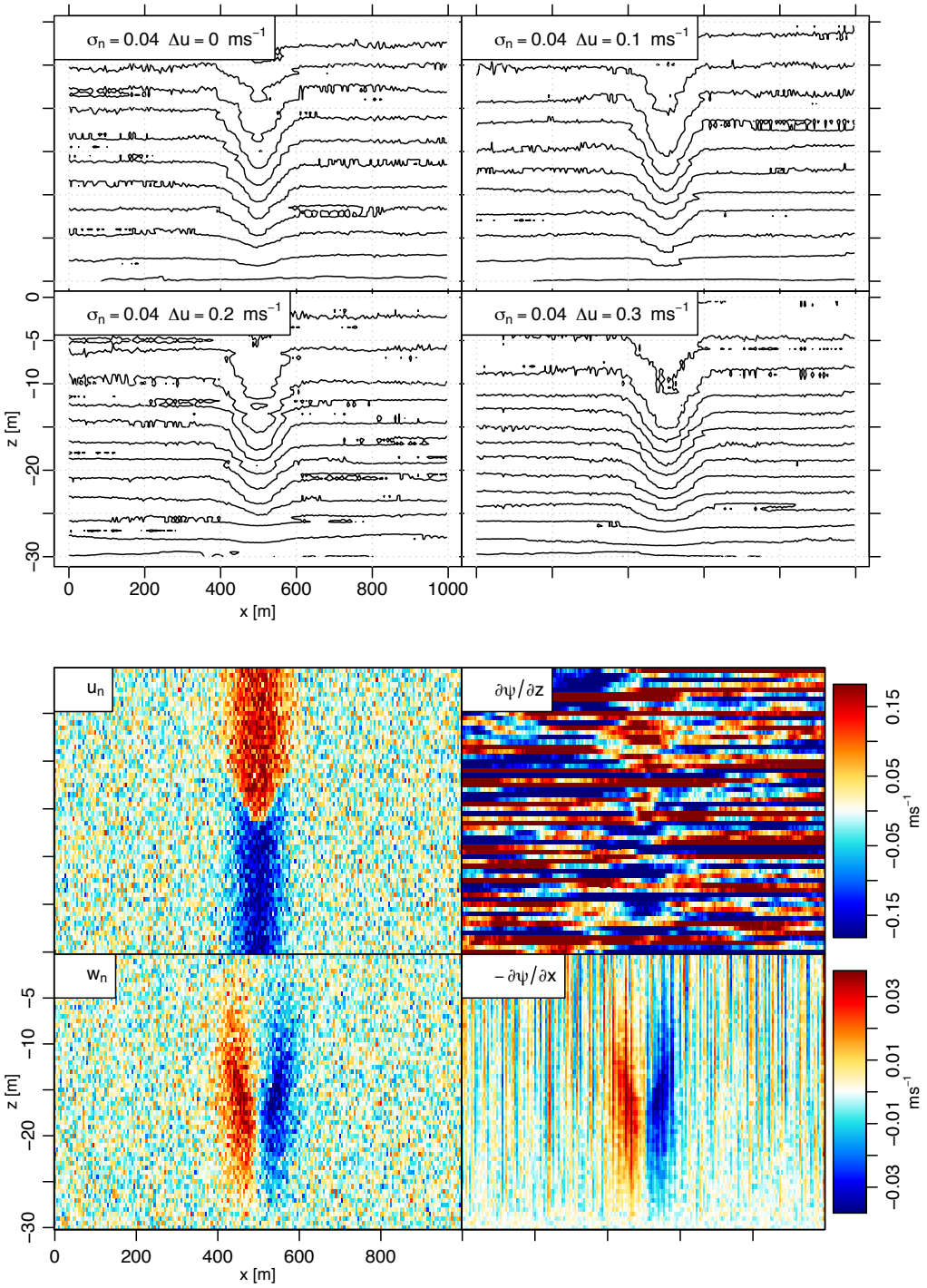

Figure 4.2: Top: As in Figure 4.1 but with a constant noise of 0.04 m/s and increasing amounts of background shear. Bottom: The comparison between the u and w velocity fields with noise (left column), and the velocities derived from the inferred streamfunction (right column).

The effect of noise and shear on the inferred streamfunction for the MS technique may be a consequence of calculating integrals in one direction at a time. Errors in the velocity field accumulate under integration much like a random walk. The direction of integration (whether to first integrate u vertically or w horizontally) affects the result, as will the choice of different estimates to average. In addition, the combination of u and w to ψ is only effected through the averaging of the various estimates (ψ_u, ψ_{w_D}, and ψ_{w_U}), and thus adjacent rows (or columns) of ψ may have very different values.

4.3 The Relaxation Method

Another method for determining streamfunctions, used within the meteorology and satellite communities, is to solve a Poisson equation for ψ. Starting with the definitions in Equation 4.2, a Poisson equation for ψ can be constructed as

$$\frac{\partial^2 \psi}{\partial x^2} + \frac{\partial^2 \psi}{\partial z^2} = \zeta(x, z), \tag{4.8}$$

where $\zeta(x, z) = \frac{\partial u}{\partial z} - \frac{\partial w}{\partial x}$ is the vorticity in two dimensions.

Techniques for solving Poisson equations on a regular grid have been in use for many years (see e.g. *Young*, 1971; *Press et al.*, 2007). One method is to solve the matrix system directly, e.g.

$$\mathbf{A} \cdot \psi = \mathbf{b}.$$

The biggest disadvantage of this technique is that it is inefficient when ψ is large. If ψ is of size $I \times J$, where I is the number of rows and J is the number of columns, the matrix $\mathbf{A}$ is of size $IJ \times IJ$. For a typical dataset here, ψ might of of size 1000×100 elements, giving an $\mathbf{A}$ of size $(IJ)^2 = 10^{10}$. If the elements of $\mathbf{A}$ are stored as a 4-byte floating point numbers, the storage required is greater than 40 gigabytes.

A more efficient way of solving such a system is to use a relaxation method. To do so, we construct a time-dependent diffusion equation

$$A\frac{\partial \psi}{\partial t} = \frac{\partial^2 \psi}{\partial x^2} + \frac{\partial^2 \psi}{\partial z^2} - \hat{\zeta}, \tag{4.9}$$

on the grid, where A is an arbitrary constant with dimensions of m^2/s and $\hat{\zeta}$ is the

vorticity estimated from the velocity data. Iterating the solution of Equation 4.9 by updating the values for ψ at each iteration implies that an initial guess will "relax" to a solution as $t \to \infty$ and the $\frac{\partial \psi}{\partial t}$ term vanishes (*Press et al.*, 2007). In practice, the solution only needs to be iterated until a convergence criterion is reached – e.g. until the difference between successive solutions is below a predefined threshold. The relaxation solution converges for matrices $\mathbf{A}$ that are diagonally dominant, which is typically the case for those derived from finite differencing (*Press et al.*, 2007).

The most straightforward method for solving relaxation problems dates back to Carl Gustav Jacobi, and is called "Jacobi relaxation" (*Press et al.*, 2007). Using forward in time, centred in space differencing (FTCS), equation 4.9 yields

$$\psi_{i,j}^{(t+1)} = \psi_{i,j}^{(t)} + \frac{\Delta t}{A\Delta x^2}\left(\psi_{i+1} + \psi_{i-1} - 2\psi_i\right)_j^{(t)} + \frac{\Delta t}{A\Delta z^2}\left(\psi_{j+1} + \psi_{j-1} - 2\psi_j\right)_i^{(t)} - \frac{\Delta t}{A}\hat{\zeta}_{i,j} \tag{4.10}$$

where (i, j) are indices for the (x, z) directions, t is the time index, Δt is the time step, and $(\Delta x, \Delta z)$ are the horizontal and vertical grid spacings. For the FTCS scheme in two dimensions, the numerical stability is determined by

$$\frac{\Delta t}{A\Delta z^2} \leq \frac{1}{4},$$

(*Press et al.*, 2007), where $\Delta z < \Delta x$. The maximum time step is therefore $\Delta t = A\Delta z^2/4$, and the finite difference equation can now be written as

$$\psi_{i,j}^{(t+1)} = \psi_{i,j}^{(t)} + \frac{\Delta z^2}{4\Delta x^2}\left(\psi_{i+1} + \psi_{i-1} - 2\psi_i\right)_j^{(t)} + \frac{1}{4}\left(\psi_{j+1} + \psi_{j-1} - 2\psi_j\right)_i^{(t)} - \frac{\Delta z^2}{4}\zeta_{i,j}. \tag{4.11}$$

To find the solution, an initial guess $\psi^{(0)}$ is used for $\psi^{(t)}$ (usually just $\psi_{i,j} = 0$), and the finite differencing is repeated until the difference between $\psi^{(t+1)}$ and $\psi^{(t)}$ is below a desired threshold.

It can be shown that the number of iterations r to reduce the error by a factor of $10^{-\mathcal{F}}$ is

$$r \simeq \frac{1}{2}\mathcal{F}J^2$$

for a $J \times J$ grid (*Press et al.*, 2007). Depending on the size of the matrices and available computer speed, it may be preferable to use a "successive over-relaxation" (SOR) scheme, in which the value of ψ at a given time step is *over-corrected*, in

anticipation of future changes. It can be shown that convergence for this method is proportional to $\mathcal{F}J$ (*Press et al.*, 2007). For the fields encountered in this study, it was found that the Jacobi method achieved satisfactory convergence ($\mathcal{F} \sim 4$) in wall-clock times less than 1 s, generally corresponding to approximately 10000 iterations. For this reason, the simpler method was used here.

A possible advantage of the relaxation method over direct integration methods such as MS, is that the solution in the domain is computed from velocity gradients in both the x and z directions simultaneously. This may produce smoother gradients in the presence of noise, a matter to be tested in Section 4.3.2. On the other hand, the finite differencing scheme requires boundary conditions on the initial guess $\psi^{(0)}$, which are not updated at each iteration, and therefore have a significant effect on the solution throughout the domain. The advantage of this is that it constrains the solution near the boundaries to be continuous, unlike the MS method. The disadvantage is that a poor choice of a boundary condition will mask the solution in the interior and produce unphysical results and long convergence times.

4.3.1 Implementation of the Relaxation Method

In some applications it can be assumed that $\psi = 0$ on the boundary, effectively implying that the streamlines are everywhere parallel to it. Such an assumption would be reasonable in a closed domain such as an ocean basin or laboratory tank. It is clearly unphysical in the current context, however, given that even with no wave features and a background flow that is everywhere 0 the streamlines should be horizontal as a result of the moving frame of reference, and therefore perpendicular to the boundary at either end of the domain.

A second method for obtaining boundary values of ψ (i.e. ψ_b), is to use the definitions in Equation 4.2 and integrate the normal velocities around the boundary, according to

$$\psi_b = -\int V_n \, ds \tag{4.12}$$

where V_n is the outward velocity normal to the boundary and $\int() \, ds$ is an integral along the boundary (in the tangential direction s). See Figure 4.3 for a definition sketch.

The boundary integration described in Equation 4.12 suffers from issues similar to those described for the MS method – that errors in the boundary velocity will

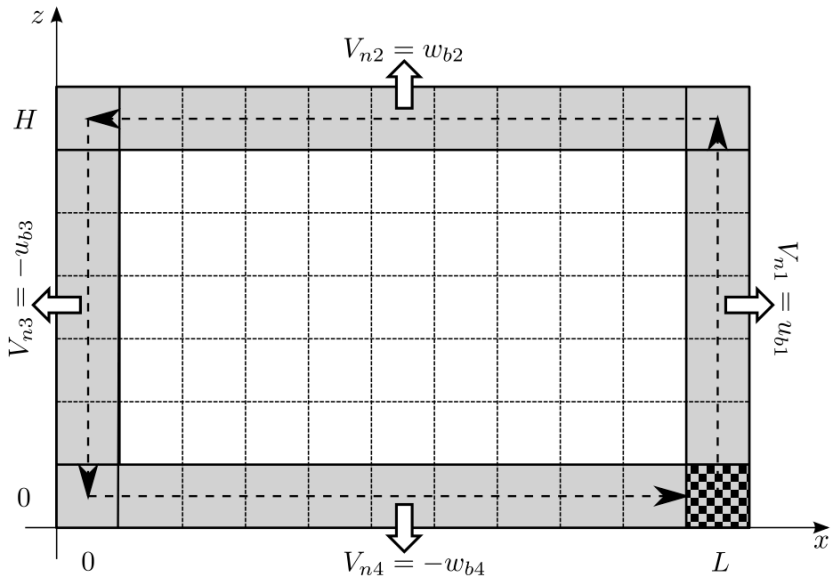

Figure 4.3: Definition sketch for the boundary velocity integration to determine ψ_b. The checkered cell is the starting location for the integration, which proceeds counterclockwise following the dashed arrows. Outward normal velocities at each boundary are indicated by the white arrows.

accumulate under the integral. A further issue is related to the assumption of zero divergence in the flow. Consider a two-dimensional surface $\mathcal{A}$, bounded by the curve $\mathcal{C}$. If $L(x, z)$ and $M(x, z)$ are continuous functions defined on an open region containing $\mathcal{A}$ and have continuous derivatives, Green's theorem states that

$$\oint_{\mathcal{C}} (L\,dx + M\,dz) = \iint_{\mathcal{A}} \left(\frac{\partial M}{\partial x} - \frac{\partial L}{\partial z} \right) dx\,dz \tag{4.13}$$

(*Jeffreys and Jeffreys*, 1956). Substituting $M = u$ and $L = -w$, yields

$$\oint_{\mathcal{C}} V_n\,ds = \iint_{\mathcal{A}} \left(\frac{\partial u}{\partial x} + \frac{\partial w}{\partial z} \right) dx\,dz. \tag{4.14}$$

For a non-divergent velocity field, Equation 4.14 will evaluate to zero. In the presence of some divergence, however, it can be seen that using Equation 4.12 to determine ψ_b will result in a mismatch between the starting and ending values (i.e. $\oint V_n\,ds \neq 0$).

The effect of the mismatch when evaluating ψ_b numerically is to introduce a large gradient of ψ at the location where the boundary integration is started. When

used as an initial condition for the relaxation solution, the anomalous gradient is propagated throughout the domain, producing unphysical results. In implementations of this technique within the meteorological community (see e.g. *Shukla and Saha*, 1974, and references therein), the boundary velocities are corrected for any mismatch by compensating for any residual from Equation 4.14, equally along the path. This procedure should also account for errors introduced through a numerical approximation of the derivative.

In summary, the relaxation method described thus far, termed the *simple-relaxation* (or SR) method, consists of several steps:

1. Use the (u, w) velocity field to calculate the vorticity, $\hat{\zeta}(x, z)$.

2. Choose a starting location arbitrarily – here it is the lower right corner of the (x, z) domain, i.e. $(L, 0)$. Set $\psi = 0$ at this location.

3. Integrate the normal boundary velocities around the boundary (here, using the trapezoidal approximation). This amounts to four separate integrals, evaluated in a counterclockwise direction, and with the starting value of each successive integral taken from the final value from the previous boundary, e.g.

$$\begin{aligned}
\psi_{b1}(z) &= -\int_0^z u(L, z')\, dz' \\
\psi_{b2}(x) &= -\int_L^x w(x', H)\, dx' + \psi_{b1}(H) \\
\psi_{b3}(z) &= -\int_H^z -u(0, z')\, dz' + \psi_{b2}(0) \\
\psi_{b4}(x) &= -\int_0^x -w(x', 0)\, dx' + \psi_{b3}(0).
\end{aligned}$$

4. Determine the residual from the difference between the starting and ending values. In this case, because the starting value is chosen as 0, the residual is simply the final value of ψ_{b4}. Dividing this residual by the total length of the boundary yields an outgoing velocity correction to be added back to the boundary velocities.

5. The boundary integral is then repeated, using the corrected velocities, to get a new estimate of ψ_b.

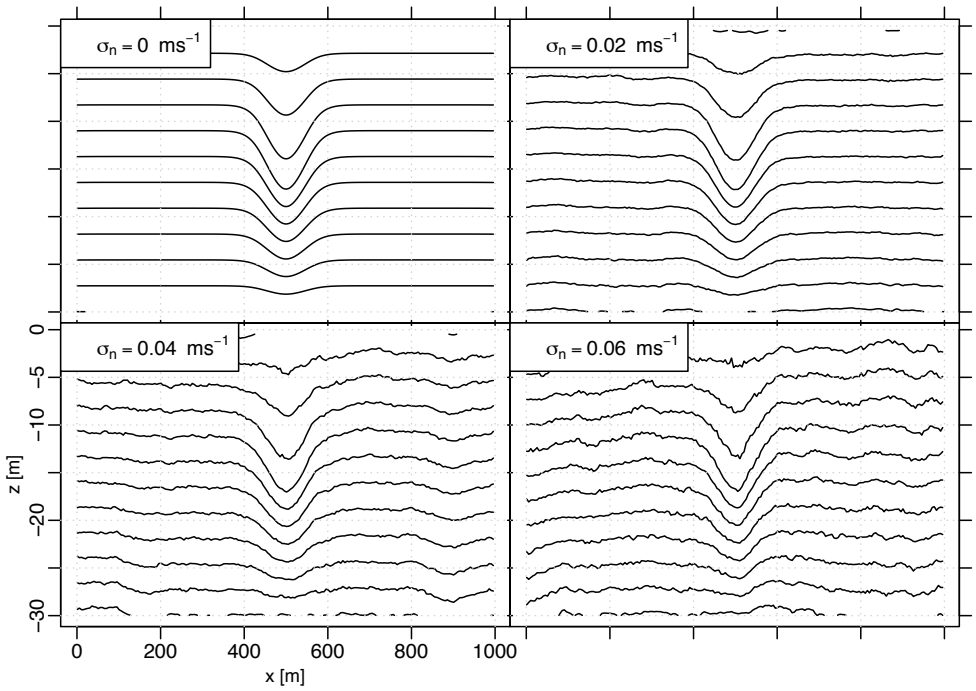

Figure 4.4: As Figure 4.1 but for the SR method

6. The boundary conditions are inserted into an initial guess array $\psi^{(0)}$, with $\psi = 0$ everywhere but the boundary.

7. The solution is then found by solving 4.8 using the relaxation scheme.

4.3.2 Evaluation of the SR Method

The SR method was evaluated similarly to the MS method, using identical wave fields, and Gaussian noise with the same statistical properties. Results for the inferred streamfunction including random noise and background shear are presented in Figures 4.4 and 4.5.

The improvement over the MS method is evident in a comparison of Figure 4.4 and Figure 4.1. While the effect of increasing noise in the velocities is to produce similarly noisy streamlines, the wave solution remains the prominent feature. This may be attributed to smoothing by the two dimensional centred differences in the relaxation solver; the value of ψ at any given point is constructed from the four values immediately surrounding it.

When noise and vertical shear are combined, the results for ψ maintain their consistency using the SR method (Figure 4.5, top panel). The streamlines above

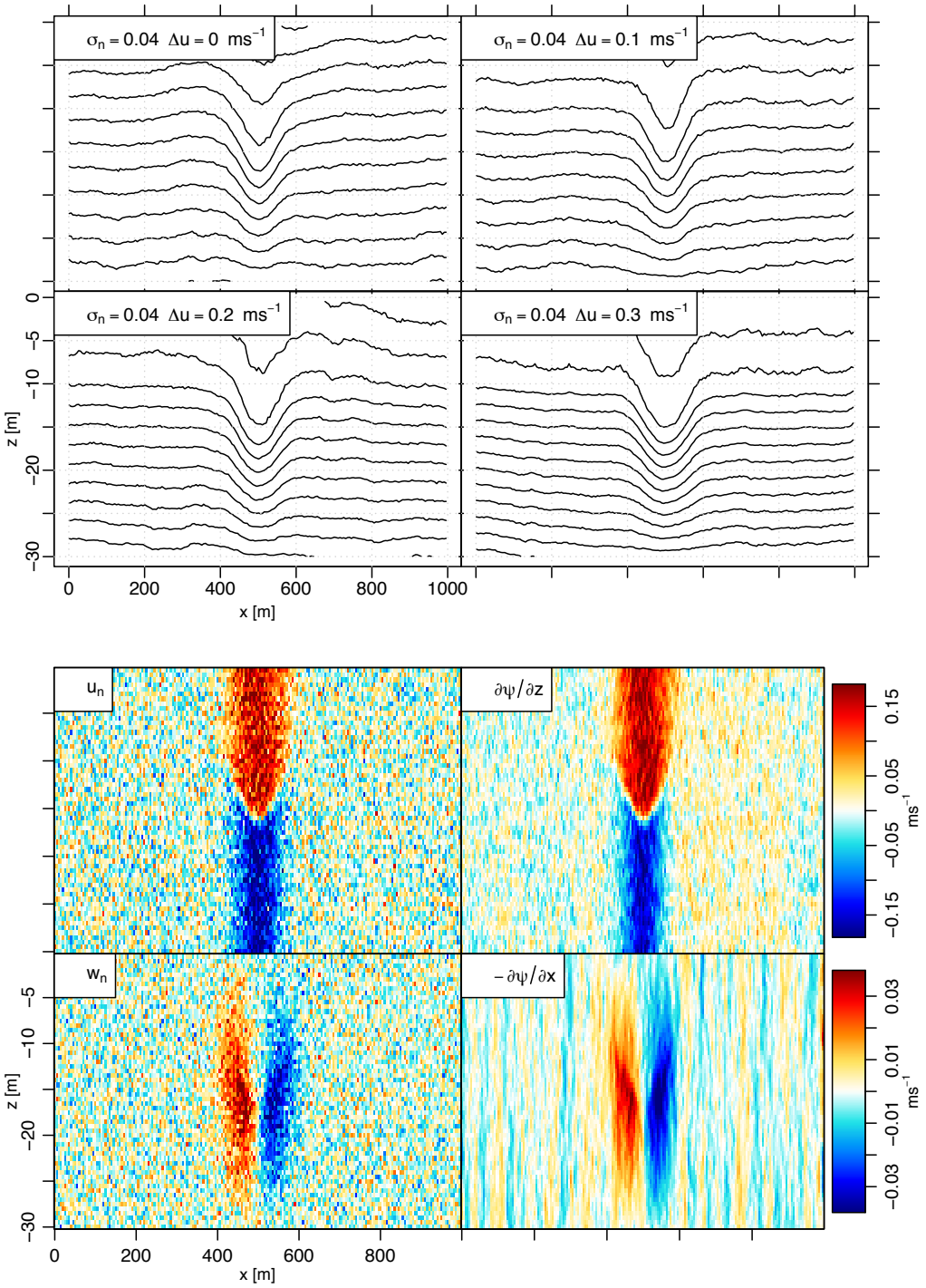

Figure 4.5: As in Figure 4.2 but for the SR method.

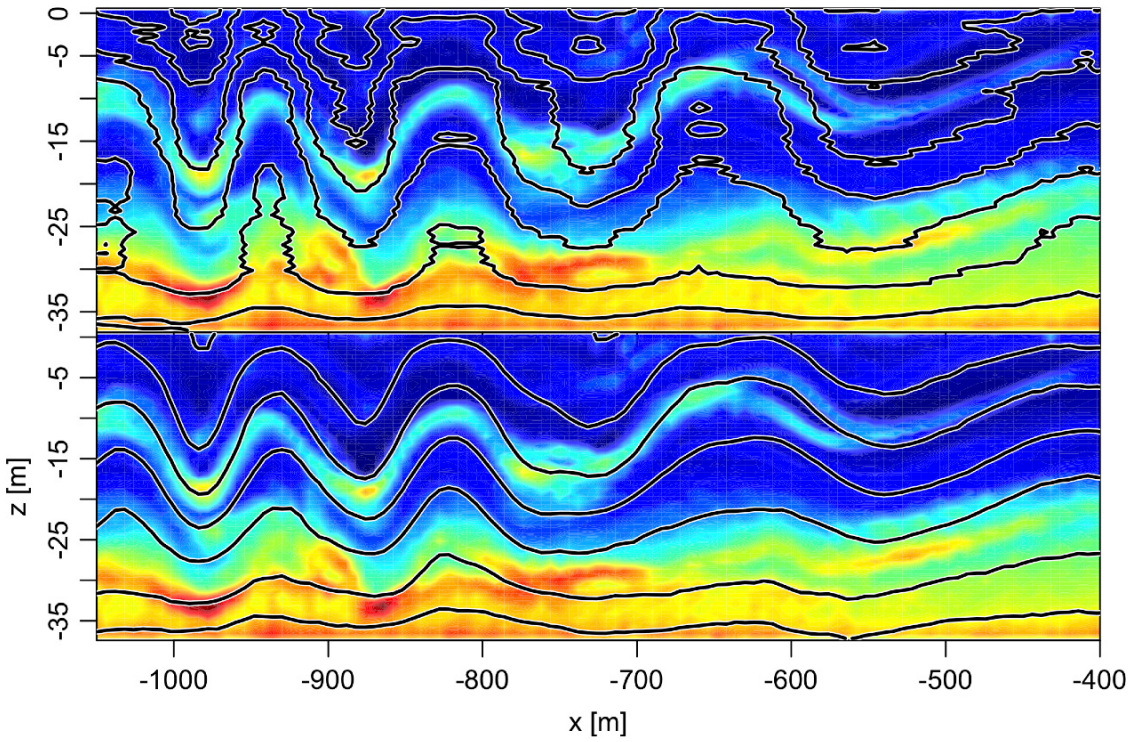

Figure 4.6: Comparison between the MS (top) and SR (bottom) methods for inferring ψ, using ADCP data from *M09*. Acoustic backscatter (arbitrary units) is represented by the colour scale, and the solid contours indicate inferred streamlines. The time series has been converted to a spatial series in x using the wave speed, and the 3 dimensional water velocities have been rotated to a coordinate system aligned with the direction of propagation. The corresponding time period is from 2008-06-30 15:00 to 15:30 UTC.

the pycnocline, in the region of positive background velocity, are most affected by the added noise. This would have little effect on the inferred density structure for this example, as the vertical gradient is nearly zero in the upper water column. The rms errors for the u and w fields reconstructed from ψ in Figure 4.5 are 0.034 m/s and 0.01 m/s, respectively. Note that the rms error for u is approximately 7 times smaller than with the MS method (see Figure 4.2).

4.4 Application to SLEIWEX 2008 Data

As a final test of the SR method (and for further comparison with the MS method), some examples of internal waves were selected from the SLEIWEX 2008 data[1]. In the case of the observations, there is of course no "true" field with which to compare the solutions. One possibility is to compare the streamline displacements with depth variations of strong backscatter layers appearing in the ADP record. Previous studies in the region have observed a correlation between such layers and the pycnocline (*Bourgault et al.*, 2001, 2007). The layers could be caused by biology aggregating at density interfaces, nepheloid layers stirred up by internal waves breaking farther inshore, or by turbulence. The source of the backscatter is unknown, but is not important provided it remains at a constant density for the duration of the passing waves.

Two time periods were chosen for two different moorings: 2008-06-30 15:00 to 15:30 UTC for *M09*, and 2008-07-01 16:15 to 16:45 UTC for *M07*, with results presented in Figures 4.6 and 4.7 respectively. Unlike *Moum and Smyth* (2006), no pre-processing was performed on the velocity data (low-pass filter to remove signals associated with swell), other than the coordinate rotation and interpolating missing values (fewer than 5 in *M09*). The physical regimes of the two examples are different: the waves at *M09* are propagating along the pycnocline at about mid-depth in a relatively strong background shear ($\Delta u \simeq 0.4\,\mathrm{m/s}$ over the water column), while the waves at *M07* are propagating up-slope above the mean pycnocline as waves of elevation (or boluses) in weak background shear ($\Delta u \simeq 0.1\,\mathrm{m/s}$).

While the overall ψ field contains similar features, it is clear from both examples that the SR method produces streamlines that better follow the isopycnals inferred from the backscatter (averaged from all four ADCP beams). In 4.6, a strong mid-depth backscatter layer is followed (to within a few metres) by one of the streamlines, with good agreement in vertical position at both ends of the domain. The MS method is clearly more affected by noise in the data, producing jagged streamlines. The wave steepness is also exaggerated, possibly due to the background shear or divergence in the 2 dimensional flow fields.

[1]Required for the ψ calculation are wave propagation direction and speed. The methods used to obtain these quantities are discussed in Section 5.2.1.

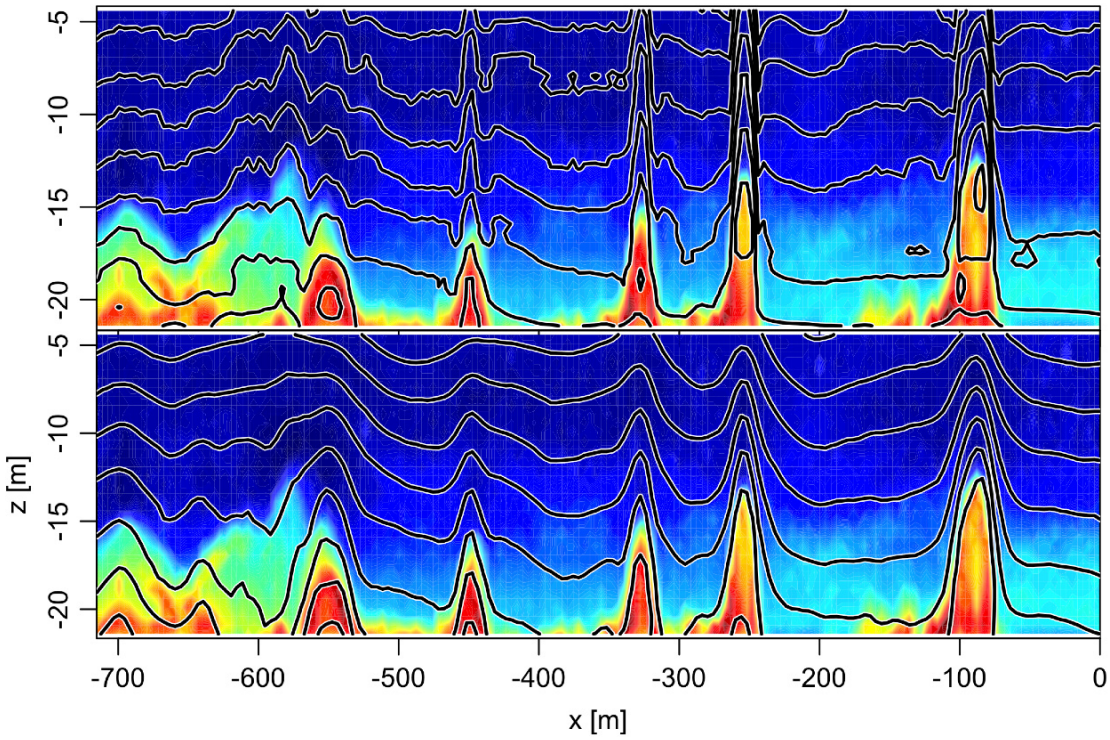

Figure 4.7: As for Figure 4.6, but with a train of elevation waves observed by the *M07* ADCP. The data is from the time period 2008-07-01 16:15 to 16:45 UTC.

Another presumed disadvantage to the MS method is the tendency to produce closed streamlines within the waves. The presence of closed streamlines indicates a recirculating (or trapped) core. Trapped cores are not an uncommon feature in shoaling internal waves, and have been observed in field measurements (see e.g. *Klymak and Moum*, 2003; *Scotti and Pineda*, 2004; *Moum et al.*, 2007b; *Lien et al.*, 2012), laboratory experiments (*Wallace and Wilkinson*, 1988; *Helfrich*, 1992), and numerical models (*Lamb*, 2002; *Venayagamoorthy and Fringer*, 2007; *Helfrich and White*, 2010). Whether the trapped cores inferred by the MS method are physically realistic is difficult to determine. A simple method for assessing if a wave contains a trapped core is if fluid velocities within the wave are greater than the propagation speed (*Lamb*, 2002). For the waves shown in Figure 4.6, analysis of the horizontal velocities indicates that the wave-induced flow is everywhere less than the estimated propagation speed of 0.6 m/s. Based on this, it is concluded that the trapped cores inferred by the MS method are unphysical in this instance.

In Figure 4.7, there is no strong backscatter layer to compare with. Instead, the waves themselves have a strong backscatter signal, the shape of which is matched quite closely by the streamlines determined with the SR method. Again the MS method produces noisier streamlines, overestimates the wave amplitude, and infers a trapped core for each of the 5 waves observed. Analysis of the horizontal current indicates that the flow within the first 3 waves is locally greater than the propagation speed of 0.4 m/s, suggesting that in this instance the presence of a trapped core is likely. This is supported by other observations of similar elevation waves (*Klymak and Moum*, 2003), and by the temperature record of the ADCP, which recorded near-bottom pulses of water $\sim 3\,^{\circ}$C colder than the surrounding fluid during wave passage.

In contrast, the SR method predicts closed streamlines only for the first wave in Figure 4.7. This may be in part because the regions of high u associated with the second and third waves extend close to, or beyond, the bottom of the range sampled by the ADCP.

4.5 Conclusions

In this chapter, a new method for inferring isopycnal displacement resulting from internal waves propagating past a fixed ADP was developed. The method is based on the solution of a Poisson equation for the streamfunction using a relaxation technique.

Comparisons with the streamfunction method of *Moum and Smyth* (2006) were performed, using a test internal solitary wave field. The new method is more robust to added noise and velocity shear, with rms error for a reconstructed horizontal velocity field more than a factor of 5 smaller than with the MS method in one example. Further tests examining the effect on the methods of background fields with divergence are warranted.

Tests with data from SLEIWEX 2008 indicate that the new method produces a realistic density field, determined by comparing with heaved acoustic backscatter layers. In contrast, the MS method was prone to producing closed streamlines, even in instances where a trapped core was not suspected.

Chapter 5

Measurements of Internal Wave Energy And Energy Flux

Building on the last two chapters, this chapter will focus on the details of the waves themselves, in particular their energetics.

In a region influenced by internal waves, spatial variations in horizontal energy flux may contribute to turbulent dissipation, and potentially act as a non-local source of energy that can be used for mixing. Recent estimates of the energy flux of linear internal waves have typically been accomplished by estimating the pressure-velocity correlations associated with the wave field (e.g. *Kunze et al.*, 2002; *Alford*, 2003; *Nash et al.*, 2005). This approach has also been applied to large-amplitude internal waves (*Chang et al.*, 2006).

For nonlinear internal waves, the linear energy flux contributes only a portion of the total energy flux. Recent studies have shown that for such waves, the nonlinear portion of the energy flux can be of similar magnitude to the linear portion, and thus cannot be ignored (*Venayagamoorthy and Fringer*, 2005; *Scotti et al.*, 2006; *Lamb*, 2007; *Lamb and Nguyen*, 2009). One approach is to estimate nonlinear fluxes using weakly nonlinear theory, where there is an equipartition of kinetic and available potential energy (*Bogucki and Garrett*, 1993; *Bourgault and Kelley*, 2003, 2007). Other studies have combined separate estimates of kinetic and available potential energy, as inferred from densely measured velocity and density observations (*Klymak et al.*, 2006; *Scotti et al.*, 2006; *Moum et al.*, 2007b; *Shroyer et al.*, 2010a). Numerical studies have also shed light on the issue, further confirming the necessity to account for both linear and nonlinear fluxes (*Venayagamoorthy and Fringer*,

2005; *Lamb*, 2007; *Lamb and Nguyen*, 2009). Further to this, in the presence of nonhydrostatic internal waves, the contributions to the pressure-velocity correlation must be divided accordingly between hydrostatic and nonhydrostatic fluxes (*Moum and Smyth*, 2006).

The aim of the present chapter is to measure the components of the horizontal internal wave energy flux field using the SLEIWEX 2008 data. This builds on previous SLEIWEX studies, which assumed an equipartition of the kinetic and available potential energy fluxes (*Bourgault and Kelley*, 2003, 2007), and which suffered from incomplete measurements of the true wave induced density perturbation field (*Mirshak*, 2008). Section 5.1 will review the theory of the energy equations, with a discussion of available potential energy (APE), while Section 5.2 will provide an overview of the methods, with examples using synthetic nonlinear internal wave fields. Results are presented in Section 5.3.

5.1 Theory

Following *Venayagamoorthy and Fringer* (2005) and *Lamb and Nguyen* (2009), the governing equations for an incompressible fluid subject to the Boussinesq approximation are

$$\frac{\partial \mathbf{u}}{\partial t} + \mathbf{u} \cdot \nabla \mathbf{u} = -\frac{1}{\rho_0} \nabla p + \nabla \cdot (\nu \nabla \mathbf{u}) - \frac{g\rho}{\rho_0} \mathbf{k} \tag{5.1}$$

$$\frac{\partial \rho}{\partial t} + \mathbf{u} \cdot \nabla \rho = \nabla \cdot (\kappa_\rho \nabla \rho) \tag{5.2}$$

$$\nabla \cdot \mathbf{u} = 0 \tag{5.3}$$

where $\mathbf{u} = (u, v, w)$ is the velocity, g is the gravitational acceleration, p and ρ are the pressure and density fields, ρ_0 is a reference density, $\nu = \mu/\rho$ is the kinematic viscosity and κ_ρ is a diffusivity for density, assumed isotropic and spatially invariant.

An equation for the kinetic energy density (per unit volume) E_k can be obtained by taking the dot product of $\mathbf{u}$ and Equation 5.1, to give

$$\frac{\partial E_k}{\partial t} + \mathbf{u} \cdot \nabla E_k + \nabla \cdot (\mathbf{u} p) = -\rho g w + \nabla \cdot (\nu \nabla E_k) - \rho \epsilon, \tag{5.4}$$

where $E_k = \frac{\rho_0}{2} \mathbf{u} \cdot \mathbf{u}$, and $\epsilon = 2\nu e_{ij} e_{ij}$ is the viscous dissipation rate of kinetic energy,

where

$$e_{ij} = \frac{1}{2}\left(\frac{\partial u_i}{\partial x_j} + \frac{\partial u_j}{\partial x_i}\right).$$

is the strain rate tensor, written using summation notation.

An equation for the potential energy density $E_p = \rho g z$ can be obtained by multiplying Equation 5.2 by gz, yielding

$$\frac{\partial E_p}{\partial t} + \mathbf{u} \cdot \nabla E_p - \rho g w = \nabla \cdot (\kappa_\rho \nabla E_p) - 2\kappa_\rho g \frac{\partial \rho}{\partial z}. \tag{5.5}$$

Adding Equations 5.4 and 5.5 gives an equation for the total energy

$$\frac{\partial}{\partial t}(E_k+E_p)+\mathbf{u}\cdot\nabla(E_k+E_p)+\nabla\cdot(\mathbf{u}p) = \nabla\cdot(\nu\nabla E_k)+\nabla\cdot(\kappa_\rho\nabla E_p)-2\kappa_\rho g\frac{\partial\rho}{\partial z}-\rho\epsilon, \tag{5.6}$$

which can be simplified by recognizing that

$$\mathbf{u} \cdot \nabla E_{k,p} = \nabla \cdot (\mathbf{u} E_{k,p}),$$

using Equation 5.3. Collecting all the divergence terms gives the final form of the energy equation as

$$\frac{\partial E}{\partial t} + \nabla \cdot \mathbf{F} = -\rho\epsilon - 2\kappa_\rho g \frac{\partial \rho}{\partial z}, \tag{5.7}$$

where $E = E_k + E_p$ is the total energy density, and $\mathbf{F} = \mathbf{u}p + \mathbf{u}E - \nu\nabla E_k - \kappa_\rho \nabla E_p$ is the total energy flux density. The terms in $\mathbf{F}$ represent: the flux of energy due to work done by pressure forces, the nonlinear flux of energy, and the diffusive fluxes of kinetic and potential energy. The terms on the right hand side of equation 5.7 are the rate of dissipation of kinetic energy by molecular viscosity and the work done against gravity by diffusive processes.

5.1.1 Available Potential Energy

The potential energy density, E_p, describes the energy stored in a system due to its presence in a gravitational field. It is a measure of the work done against gravitational forces to move fluid vertically, and to be meaningful must be defined relative to a reference level. It is therefore *differences* in the potential energy from the reference that are dynamically important. Consider a mass m raised from a level $z = 0$ to a height $z = h$. The potential energy of m relative to the reference level is then mgh.

For a stratified fluid, an appropriate base state has horizontal isopycnals and $\mathbf{u} = 0$. The potential energy with respect to this base state is then referred to as the *available potential energy* (APE). The APE represents the amount of potential energy in the system that may be converted to other forms, such as kinetic, and ultimately used to mix the fluid (*Lorenz*, 1955).

A straightforward method for obtaining the APE is to calculate the difference between the potential energy of the perturbed and the reference states. Written in terms of a perturbation potential energy density $E_w = \rho_w g z$, this becomes

$$APE = \int_V E_w \, dV, \tag{5.8}$$

where $\rho_w = \rho - \rho_r(z)$ is the perturbation density field, and ρ_r is a hypothetical reference density profile, obtained by adiabatically rearranging the observed density field to that with the minimum potential energy (e.g. *Hebert*, 1988; *Winters et al.*, 1995). E_w can assume both positive and negative values, depending on the sign of the density difference. Effectively this method amounts to calculating the total and background potential energy (BPE), and subtracting them to get the APE.

Another method for calculating APE involves integrating the available potential energy density, E_a, as

$$APE = \int_V E_a \, dV. \tag{5.9}$$

E_a is given by

$$E_a = g \int_z^{z^*(\mathbf{x},t)} \left(\overline{\rho}(s) - \rho(\mathbf{x},t)\right) \, ds, \tag{5.10}$$

where $z^*(\mathbf{x},t)$ is the height of the fluid parcel at $(\mathbf{x},t)$ in a reference state $\overline{\rho}$, and s is a dummy variable of integration. E_a is the work per unit volume done on a fluid element to move it from a height z^* to height z against the buoyancy force in the undisturbed fluid. If $\overline{\rho}$ decreases monotonically with z, it can be seen from Equation 5.10 that E_a is positive definite (see e.g. *Lamb*, 2008, for a thorough discussion of E_a and its relation to E_w).

Integrating either E_w or E_a over the volume of interest will give the total APE (*Lamb*, 2008). Use of E_a, however, has several advantages over E_w, including: it gives information about the spatial distribution of APE, it is independent of the coordinate system used, and combined with the kinetic energy density E_k it satisfies

a conservation law similar to Equation 5.7. The combination of kinetic and available potential energy is known as the pseudoenergy, defined as

$$\mathcal{E} = E_k + E_a \tag{5.11}$$

(see e.g. *Shepherd*, 1993; *Scotti et al.*, 2006; *Lamb and Nguyen*, 2009). If the effects of mixing are ignored and the reference state is independent of time, the pseudoenergy conservation equation is

$$\frac{\partial \mathcal{E}}{\partial t} + \nabla \cdot [\mathbf{u}\,(\mathcal{E} + p_w)] = -\rho_0 \epsilon. \tag{5.12}$$

A further advantage to using E_a, pointed out by *Scotti et al.* (2006), is that calculating APE via E_w amounts to calculating a small quantity by subtracting two large ones (total PE and BPE), potentially introducing numerical errors.

The details of APE calculations for different scenarios have been the subject of many studies. *Lamb* (2008) discusses the calculation of APE using either E_w or E_a for an isolated feature, such as an internal solitary wave, building on related studies (*Hebert*, 1988; *Winters et al.*, 1995). In particular it is noted that when using E_a, the far-field density can be used for a reference density, eliminating the need for an adiabatic redistribution. This is of great utility to laboratory and numerical studies, where the far-field density is known. However, in open or semi-open systems the proper reference state is less clear. In contrast, when using E_w the far-field density is not the appropriate reference density, and instead the APE must be calculated by sorting the density field in a finite domain and then taking the limit as the domain is extended to infinity and the calculated APE values converge (see also *Hebert*, 1988).

Example APE Calculation

The asymptotic nature of APE calculated from E_w is illustrated in Figure 5.1. For this example, a two-dimensional solitary internal wave density field was used (see Appendix B and *Stastna and Lamb* (2002)). The domain was $L_o = 1000\,\text{m}$ long by $H = 100\,\text{m}$ deep.

The APE was calculated by sorting the density field numerically, starting with the heaviest elements on the bottom and filling to the top. Due to the finite size of each of the numerical elements, the sorted density field generally consists of layers of slightly

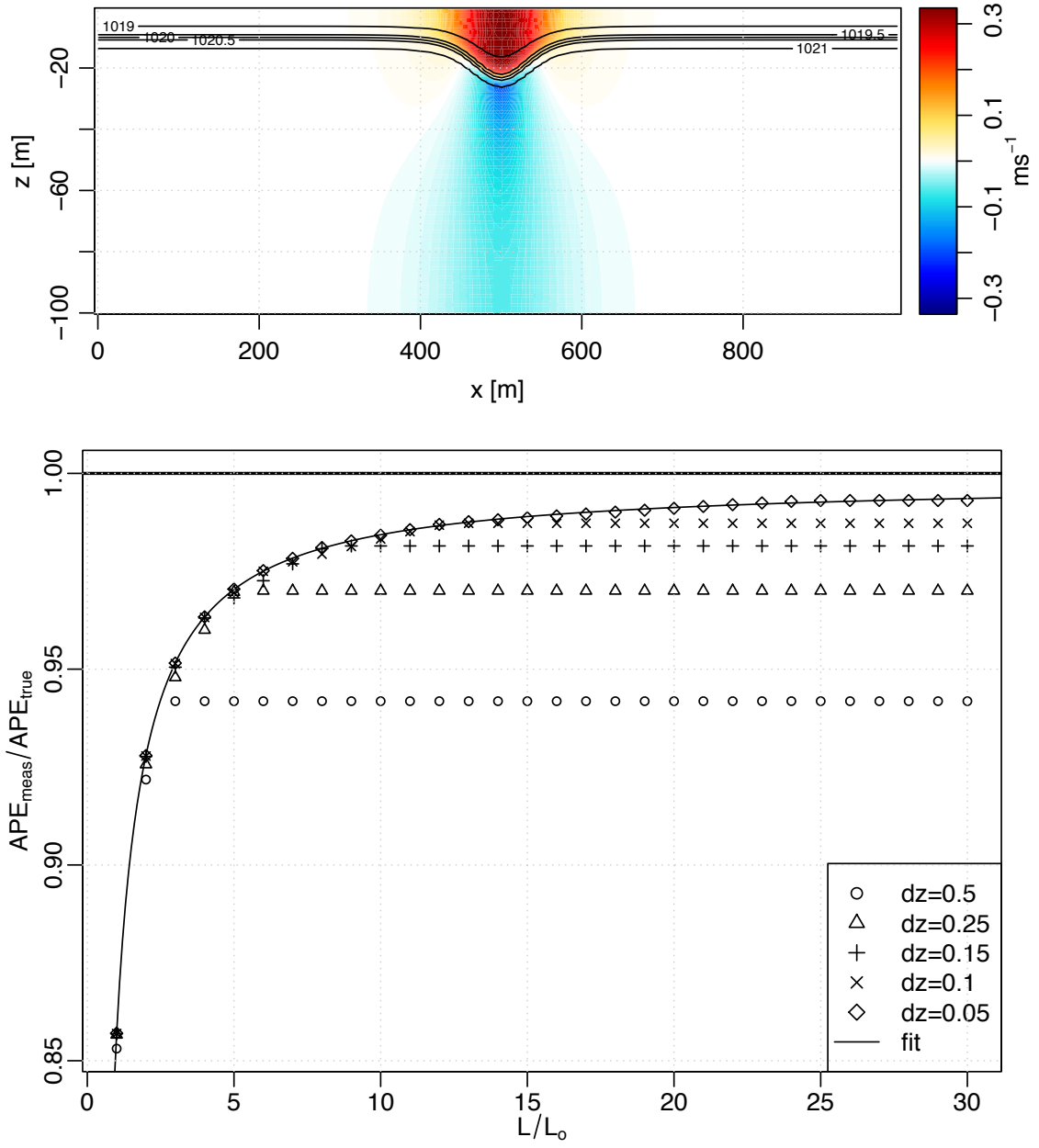

Figure 5.1: Top: synthetic wave field used for APE calculation. Isopycnals are indicated by the contours and the horizontal velocity by the colour scale. Bottom: fraction of full APE estimated by integrating E_w as a function of the length of the sorted density field and of the vertical grid size. L is the length of the extended domain and $L_o = 1000\,\mathrm{m}$ is the original domain width. The various vertical grid spacings are given by the symbols and the solid line is a fit to a functional form, discussed in the text.

different density values. *Winters et al.* (1995) addressed this by interpolating to a finer grid and then calculating the APE remaining in the sorted field as an estimate of the error. They concluded that when the rms displacements exceed the vertical grid spacing, the error in the APE is negligible. Here the sorted field was averaged along depth levels to produce horizontal isopycnals, following *Klymak et al.* (2006) and *Shroyer et al.* (2010a). The domain was then extended by an increasing amount (between 1 and 30 times L_o), with the sorting and APE calculation performed each time.

As shown in Figure 5.1, the APE calculated for each L is less than the true APE. Also apparent is a dependence on the vertical grid size, with finer grids (produced by interpolating the density field) reaching an asymptote closer to the true APE value. The asymptotic relationship was fitted to a functional form, corresponding to

$$\frac{APE_{meas}}{APE_{true}} = a_1 \left(1 - \left(\frac{a_2 L_o}{L}\right)^{a_3}\right), \tag{5.13}$$

using nonlinear least squares. Coefficients of the fit were: $a_1 = 0.998$, $a_2 = 0.141$, and $a_3 = 1.010$ (residual standard error 0.000169 on 12 degrees of freedom, p-value $< 2 \times 10^{-16}$ for each term). Note that with $a_1 = 0.998$ the true APE will not be reached using this method, however the error is small enough to be considered negligible considering other uncertainties associated with field measurements.

In practice, when using field measurements in an open system, the appropriate reference density profile to use is somewhat ambiguous. *Moum et al.* (2007b) estimate the reference profile by extending the domain on either side of their observed waves by 25 times before adiabatically redistributing the density field, while *Shroyer et al.* (2010a) extended the domain ahead of the wave by 10 times. Alternatively, *Scotti et al.* (2006) defined a time varying reference state using a combination of ship-based surveys and average values from moorings during the period immediately preceding the arrival of waves.

In a dynamic and semi-open domain such as the St. Lawrence Estuary, determining an appropriate reference density is even less clear. An adiabatic redistribution in an extended domain is complicated by the fact that an "infinite" domain size is unphysical, and thus a far-field density profile does not exist. At the SLEIWEX field site, the bottom shallows nearly linearly in the region in which waves are observed

to shoal (see Figure 2.2). One might expect that the adiabatic redistribution should be performed in a domain that mimics this profile shoreward of the measurement location, however, this would only apply to waves which propagate orthogonal to the shoreline. Tests comparing the redistribution in a sloped domain to a rectangular one indicated that the result was not overly sensitive to the presence of the slope (less than 1% difference in APE). In addition, waves are often observed in groups, contrary to the assumption that they can be treated as "isolated features", as in *Hebert* (1988) and *Lamb* (2008). Further than this, the background density field may change on time scales comparable to wave shoaling times, due to tides, passing fronts, or other mesoscale features. An exact definition for the appropriate base state for systems such as the St. Lawrence Estuary remains an open question.

5.2 Measuring Wave Energy and Energy Flux

With both the velocity and density fields, an estimate can be made of the internal wave kinetic and available potential energies. Together with a measure of energy advection, these in turn can be used to estimate the horizontal energy flux. In this section, the technique used to estimate the energy and energy flux of internal waves from the SLEIWEX site will be discussed.

For flow in the (x, z) plane, if the viscous and diffusive transport terms are ignored, Equation 5.7 can be rewritten as

$$\frac{\partial \mathcal{E}}{\partial t} + \frac{\partial f_E}{\partial x} + \frac{\partial}{\partial z}[w(p + \mathcal{E})] = -\rho\epsilon, \tag{5.14}$$

where $f_E = up + u\mathcal{E}$ is the horizontal pseudoenergy flux. The terms in the z-derivative represent internal redistribution of energy, and therefore disappear under a vertical integral (*Moum et al.*, 2007b).

For a linear internal wave, it can be shown that the integrated energy flux is given by

$$\langle f_E \rangle = c_g \langle \mathcal{E} \rangle, \tag{5.15}$$

(*Kundu and Cohen*, 2002, Chapter 7.21), where

$$\langle\, \rangle = \int_{t_0}^{t_1} \int_{-H}^{0} (\,)\, dz\, dt, \tag{5.16}$$

and c_g is the group velocity. For nondispersive waves, such as internal solitary waves, Equation 5.15 is also expected to hold for field observations if dissipation is negligible over short distances (*Moum et al.*, 2007b). This relationship will be examined for the wave fields measured in the SLEIWEX 2008 experiment. Note that for a nondispersive wave there is no distinction between phase and group velocity, and in what follows c is used as simply the wave velocity.

The kinetic energy density E_k for a wave is evaluated from the ADP data directly as $E_k = \rho_0/2(u^2 + w^2)$, and the available potential energy density is calculated following Equation 5.10. Spatial integrals (i.e. in x and z) of these two quantities are denoted as

$$KE = \int_{x_1}^{x_2} \int_{-H}^{0} E_k \, dx \, dz \tag{5.17}$$

$$APE = \int_{x_1}^{x_2} \int_{-H}^{0} E_a \, dx \, dz, \tag{5.18}$$

where x_1 and x_2 encompass the entire wave.

5.2.1 Wave Speed and Direction

Central to the assumptions involved in the streamline-to-isopycnal conversion (Chapter 4) is the assumption that the waves are two-dimensional, and propagate at a constant speed in a known direction. If the wave speed and direction are known, it is a simple matter to rotate the geographically referenced velocities from the ADP to a coordinate system aligned with the wave, and to apply the ψ-technique of choice.

Mirshak and Kelley (2009) discuss three methods for inferring nonlinear internal wave propagation direction from ADP measurements, focusing on the effect of vertical shear and depth-average background flow. The methods are: a "filtering" method, based on high-pass filtering the velocities; a "beamwise" method, first presented by *Scotti et al.* (2005) and utilizing lagged correlations between the ADP beams; and a "modal" method, where the high-pass filtered velocities are regressed onto a normal-mode model using an estimate of the stratification. *Mirshak* (2008), and *Mirshak and Kelley* (2009) found that the modal method performed the best when wave amplitudes and vertical shear were large and when depth-averaged background currents were nonzero. These background conditions hold in the present application, so the modal method is used here.

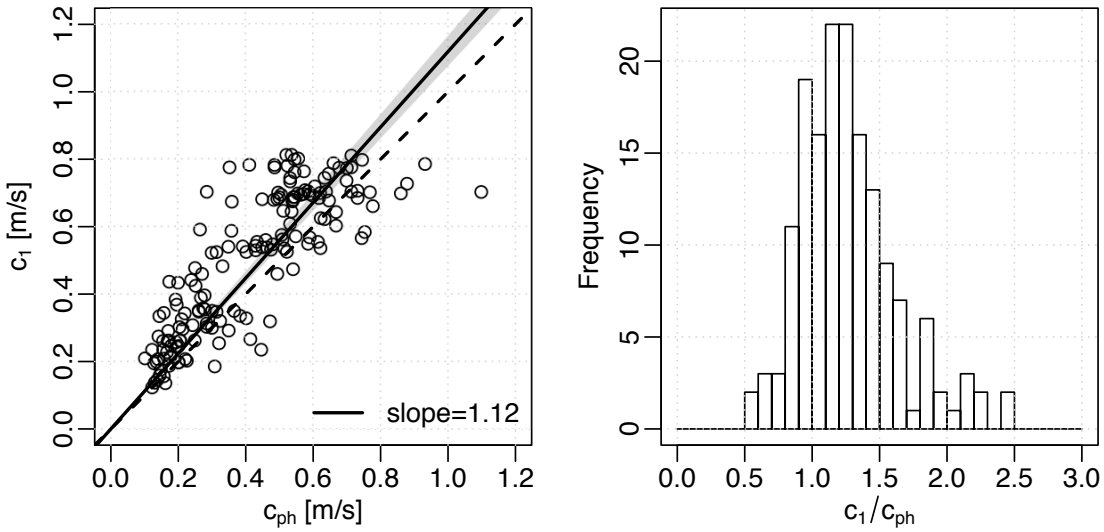

Figure 5.2: Comparison of wave speeds measured from photogrammetry with mode-1 phase speed. Left: scatterplot of c_1 and c_{ph}. The solid line is a linear fit through the origin, with slope indicated in the legend, and the grey region shows the 95% confidence interval. The dashed line indicates a 1:1 relationship. Right: histogram of c_1/c_{ph}.

To estimate the wave speed, the time-varying baroclinic mode-1 phase speed was estimated using density stratification from the TDR chain. The use of the mode-1 speed was justified by comparison with waves speeds (c_{ph}) measured from surface signatures in the shore-based photogrammetry (see e.g. Figures 2.3, 6.6, and 6.9) on July 1st and 2nd, presented in Figure 5.2. There is some scatter in the graph, and a linear regression through the origin gives a relationship of $c_1 = 1.12c_{ph}$ (residual standard error 0.134 on 159 degrees of freedom, R^2 of 0.94, p-value $< 1 \times 10^{-16}$). Overall, the mode-1 speeds are slightly larger than the photogrammetry speeds.

Alternatively, *Moum and Smyth* (2006) use the phase speed of the first baroclinic mode from weakly nonlinear theory, corresponding to

$$c_{wnl} = c_1 + \frac{1}{3}\gamma a, \tag{5.19}$$

where a is the wave amplitude, and γ is a nonlinearity parameter defined by

$$\gamma = \frac{3c_1}{2} \frac{\int_{-H}^{0} (d\Pi_1/dz)^3 \, dz}{\int_{-H}^{0} (d\Pi_1/dz)^2 \, dz}, \tag{5.20}$$

and Π_n is the structure function for the first vertical mode (i.e. a solution of Equation 3.9). Tests using Equation 5.20 with typical stratifications and depths for the SLEIWEX site indicated that the difference between c_1 and c_{wnl} was small ($\lesssim 0.03\,\mathrm{m/s}$ for a 5-10 m wave in $< 40\,\mathrm{m}$ of water), and so the linear wave speed was used here.

5.2.2 Pressure Field of a Nonlinear Internal Wave

To this point, methods for obtaining the kinetic and available potential energy densities have been described, including the inference of the wave-heaved density field required for the APE calculation. To calculate energy flux, the wave-heaved density field must also be used for the pressure-velocity correlations in the linear energy flux.

Moum and Smyth (2006) describe the partitioning of the perturbation pressure field of a nonlinear internal wave into three components: the internal hydrostatic pressure associated with heaved isopycnals; the external hydrostatic pressure associated with surface displacements; and the nonhydrostatic pressure caused by large vertical accelerations. For nonlinear waves, they show that all three components can contribute significantly to the total pressure field, and hence the total linear energy flux. A brief summary of their development is provided in this section.

The vertical component of the momentum equations for a non-rotating inviscid Boussinesq fluid is

$$\frac{\partial p}{\partial z} = -\rho g - \rho_0 \frac{Dw}{Dt}, \tag{5.21}$$

where the two terms on the RHS are taken to be the hydrostatic and the nonhydrostatic pressure, respectively, with the mean free surface defined to be at $z = 0$ and the bottom at $z = -H$. If the surface displacement is small, the pressure at $z = 0$

can be written as a Taylor expansion, where

$$p|_{z=0} = -\eta_0 \left.\frac{\partial p}{\partial z}\right|_{z=\eta_0} = \rho_0 \eta_0 \left.\left(g + \frac{Dw}{Dt}\right)\right|_{z=\eta_0} = \rho_0 g \eta_0,$$

and it is assumed that Dw/Dt is small compared to g. The surface displacement associated with the wave is denoted by η_o, and the pressure at the water surface ($z = \eta_0$) is taken to be zero (equal to atmospheric pressure).

If η_0 is unknown, which in general it will be for moored ADP data, it can be estimated by integrating the inviscid horizontal momentum equation

$$\frac{\partial p}{\partial x} = -\rho_0 \frac{Du}{Dt} \tag{5.22}$$

in the x direction, at $z = 0$. Assuming that the surface displacement vanishes at $x = \pm\infty$, η_0 is

$$\eta_0 = -\frac{1}{g} \int_{-\infty}^{x} \frac{Du_0}{Dt}\, dx' \tag{5.23}$$

where u_0 is the horizontal velocity at the surface. $\rho_0 g \eta_0$ is termed the "external" hydrostatic pressure, as it results from sea surface changes caused by the wave and is independent of depth.

The hydrostatic contribution to the pressure signal is therefore

$$p_h = \int_z^0 \rho_w g\, dz', \tag{5.24}$$

where ρ_w is the density perturbation of the wave from a background density field, as already defined in Section 5.1.1. Similarly, the nonhydrostatic pressure perturbation is then

$$p_{nh} = \rho_0 \int_z^0 \frac{Dw}{Dt} dz'. \tag{5.25}$$

The total pressure perturbation associated with the wave is therefore

$$p_w = p_h + \rho_0 g \eta_0 + p_{nh}. \tag{5.26}$$

Some assumptions and approximations must be included when using real data in Equation 5.26. First, because the measurements are collected at a fixed point, the time-to-space conversion for a wave with constant form is invoked, e.g. $\partial/\partial t =$

$-c\,\partial/\partial x$, as in Section 4.1. Second, because a bottom mounted ADP cannot sample all the way to the surface, assumptions are needed for the horizontal velocities above the highest bin. In general, an assumption of constant near-surface velocities may contribute little error, provided the highest bin is above the mean pycnocline depth. As an example, consider the wave in Figure 5.1, where the horizontal velocities above the pycnocline can be seen to be relatively uniform. Finally, the spread of the ADP beams with height above the bottom will contribute some uncertainty to the estimate of u_0, and hence η_0. For an ADP with beams 20° from the vertical, the surface beam separation in water 40 m deep is about 30 m. *Moum and Smyth* (2006) estimate that η_0 will be underestimated by about 20% for waves with a similar wavelength to beam separation ratio as the ones observed in the St. Lawrence Estuary.

5.2.3 Nonlinear Internal Wave Example

To illustrate the concepts presented in the previous section, and to examine the form of the energy fluxes for a simple case, the formulae were applied to the same solitary internal wave field used for the streamfunction tests in Section 4.1.

Wave Pressure Field

Figure 5.3 highlights the contribution to the total wave induced pressure signal by each of the terms discussed previously. The largest signals arise from the internal hydrostatic pressure p_h, resulting in a negative perturbation due to the downward advection of lighter fluid due to the wave. p_h only has a signal below the pycnocline, as a result of the uniform upper layer due to the hyperbolic tangent density profile. The external hydrostatic pressure, $\rho_0 g\eta_0$, has the opposite sign to p_h, indicating that a wave of depression will have a positive sea surface anomaly η_0. The magnitude of $\rho_0 g\eta_0$ is approximately half that of p_h, indicating that this term will likely be important in natural systems.

The nonhydrostatic pressure perturbation p_{nh} is the smallest of the three components. Because of the opposite sign of p_h and $\rho_0 g\eta_0$, p_{nh} has a magnitude that is approximately 10% of the total pressure perturbation. For more strongly nonlinear waves, p_{nh} is expected to be even larger, as the vertical accelerations of the wave face and tail increase.

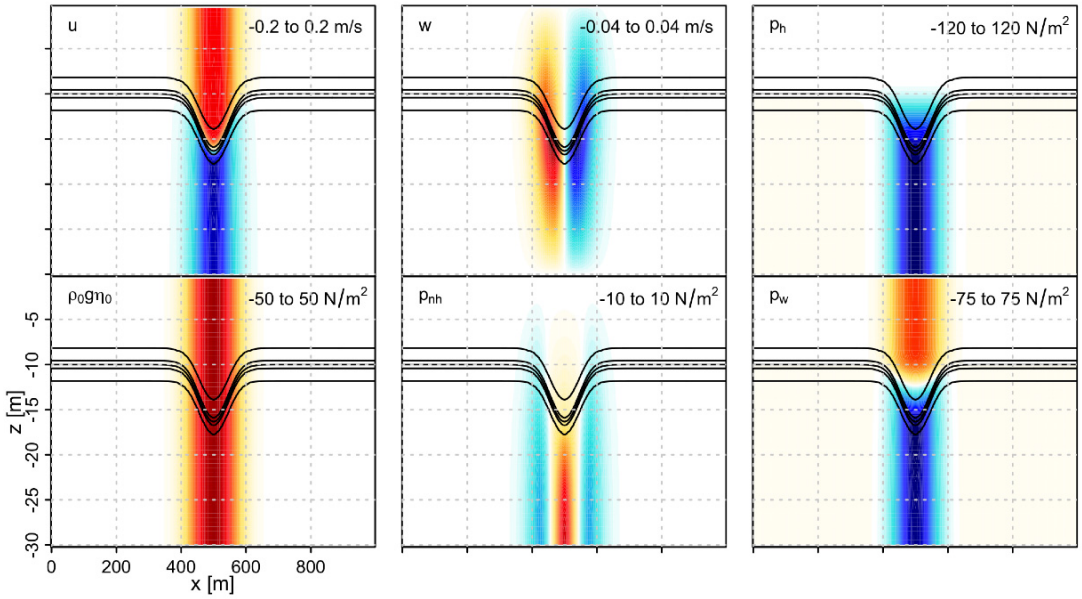

Figure 5.3: Velocity and pressure fields for a solitary internal wave. Top row: horizontal velocity u, vertical velocity w, internal hydrostatic pressure p_h (Equation 5.24). Bottom row: external hydrostatic pressure $\rho_0 g\eta_0$, nonhydrostatic pressure p_{nh} (Equation 5.25), and total pressure p_w (Equation 5.26). The solid lines indicate isopycnals between 1019 and 1021 kg/m^3 in 0.5 kg/m^3 intervals. The range of the color scale in each panel is indicated in the upper right corner, with blue (red) representing low (high) values.

Wave Energy and Energy Flux Field

Next the energy densities and fluxes for the example wave field are examined (Figure 5.4). Of interest here are the horizontal and vertical distributions of E_k and E_a, as well as the linear and nonlinear horizontal fluxes up_w and $u\mathcal{E}$. The horizontal energy flux terms are created by multiplying the various panels from Figures 5.3 and 5.4. Time and depth integrated flux values are displayed in the lower right corners, calculated according to Equation 5.16. Note that for a wave of elevation, the structure of the energies and fluxes will be largely the same as for a wave of depression, only reflected about the pycnocline.

The kinetic energy flux is distributed over the full water column, with positive values above the pycnocline (where both u and E_k are positive) and negative values below. The asymmetric distribution of the kinetic energy flux results in a small negative net contribution to the total flux. In contrast, the APE density and density

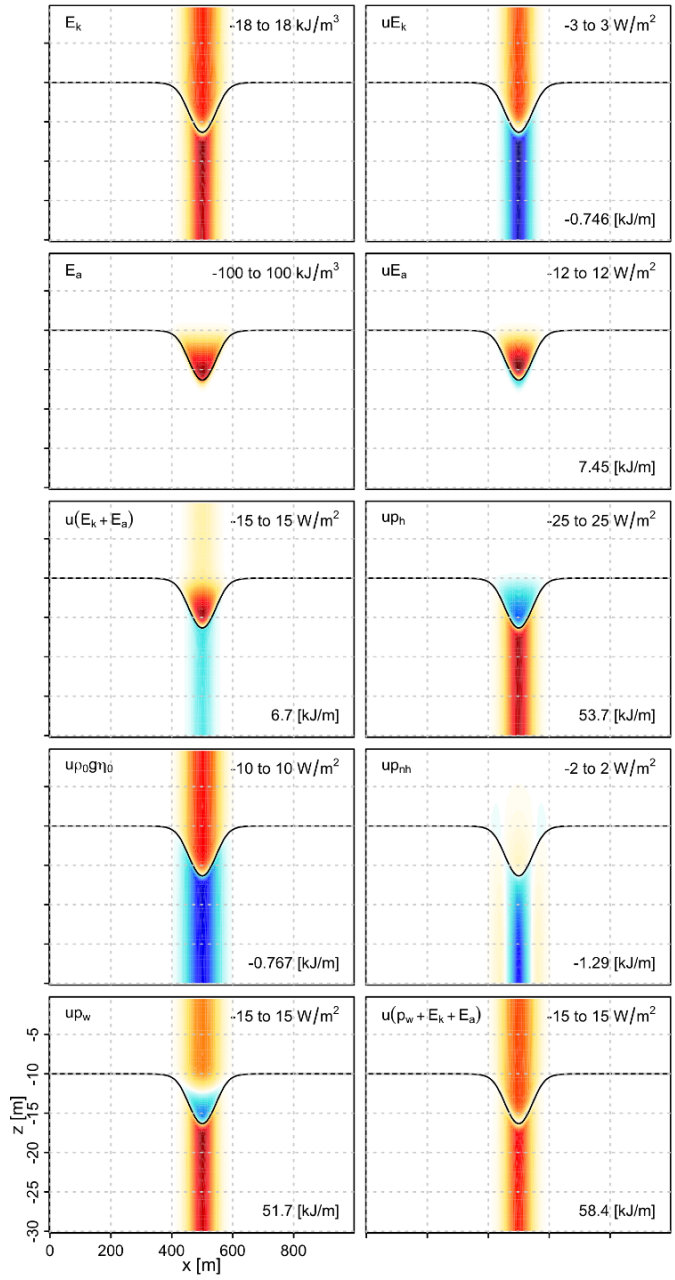

Figure 5.4: Components of energy density and energy flux for an internal solitary wave. From top left, proceeding across rows: the kinetic energy density E_k, the kinetic energy density flux uE_k, the APE density E_a, the APE density flux uE_a, the total nonlinear pseudoenergy flux $u\mathcal{E}$, the internal hydrostatic flux up_h, the external hydrostatic flux $u\rho_0 g\eta_0$, the nonhydrostatic flux up_{nh}, the total pressure-velocity flux up_w, and the total energy flux $u(p_w + \mathcal{E})$. Energy densities are in units of kJ/m^3, energy density fluxes are in units of W/m^2, and integrated fluxes (bottom right) are in units of kJ/m. The solid line indicates the centre of the pycnocline, and the range of the color scales are given in the upper right corner.

flux are concentrated within the vicinity of the heaved pycnocline, with fluxes being mostly positive. For this particular example, the integrated contribution of the APE flux is 7 times greater than the KE flux. The integrated KE flux increases as the pycnocline is placed farther away from the middepth (see *Lamb and Nguyen*, 2009, for more detail).

The fluxes due to the various pressure terms contain similar vertical structure. The hydrostatic pressure velocity flux is nonzero only below the undisturbed pycnocline, with the negative pressure perturbation creating a positive flux contribution in the lower layer. Figure 5.4 shows that for this case the internal hydrostatic pressure velocity flux is the largest contributor to the total flux, containing approximately 54 of the total 58 kJ/m. Net contributions from the external hydrostatic and nonhydrostatic pressures are small and negative – the former due to the asymmetric vertical distribution and the latter to relatively small vertical velocities.

The total contribution from the pressure-velocity flux can be seen to be 89%, with the remainder coming from the nonlinear energy fluxes. It should be noted that this is not a general result, as the density difference, location of the undisturbed pycnocline, and wave amplitude will all have an effect on the relative contributions of each term.

5.2.4 Effects of Limited Range

One shortcoming of using ADP data for inferring internal wave energies and energy fluxes arises due to the near-surface sampling limitations. As a result of the angled beams, velocity estimates close to a boundary will be contaminated by acoustic returns from the transducer sidelobes, and must be discarded (*RD Instruments*, 1996). For an upward-looking instrument with beam angles 15° from the vertical, this corresponds to the top 6% of the water column. Non-zero pitch and roll will also have an effect on the near boundary contamination, potentially increasing it beyond the nominal 6%. For waves of depression, the strongest horizontal velocities occur near the surface, and will therefore be missed by the instrument.

In addition, the first bin of the ADP is centred at a height above the bottom that depends on the mooring frame, the frequency of the transducers, and the specified vertical resolution. For most of the SLEIWEX 2008 ADPs, the first bin was between one and two metres above the bottom.

The result is that the ADP only samples a fraction of the full water column. This may potentially have an effect on the energy and energy flux measurements, through both the accuracy of the measured currents, and the inference of isopycnals using the streamfunction technique.

To investigate this effect, tests were performed on the same solitary internal wave field used for the example energy flux calculation, including both a depression and an elevation wave[1]. In each case, the full wave field was trimmed to a distance above the bottom corresponding to between 40 and 100% of the full depth, and the energies and fluxes were calculated using the techniques described previously.

For a wave of depression (see Figure 5.5) the inferred energies and fluxes are always smaller than the true values. The total energy flux f_E is approximately 40% of its true value when only about half of the water column is sampled, and increases approximately linearly as the sampled fraction increases. Kinetic energy and the linear energy flux up_w follow a similar pattern while the APE asymptotes to the true value when approximately 70% of the water column is sampled. The reason is that the APE density E_a is concentrated in the region of heaved isopycnals, and there is little improvement gained by sampling farther above the bottom. On the other hand, the total nonlinear energy flux is strongly affected by the truncated sampling, with the method producing fluxes of opposite sign to the true value when the sampled fraction is less than approximately 65%. The effect of the negative nonlinear fluxes on the total flux is not large, as a result of the relatively small contribution of the nonlinear fluxes observed previously (see e.g. Figure 5.4)

The effect of a limited sampling range is similar for a wave of elevation, with KE, $\langle up_w \rangle$, and $\langle f_E \rangle$ all increasing linearly toward the true values (Figure 5.6). APE asymptotes to its true value even sooner than in the depression wave case, as the heaved isopycnals are concentrated close to the ADP. The effect on the nonlinear fluxes is opposite in this case, however, as the strong positive near-bottom wave velocities cause the total flux to be overestimated. $\langle uE \rangle$ peaks at about 1.75 times the true value, and then decreases linearly when more than half of the water column is sampled.

For both the depression and elevation waves, the energy flux measured by $\langle c\mathcal{E} \rangle$ is

[1]To create the elevation wave, the same vertical density profile was specified, but with the pycnocline centred at $z = -20\,\mathrm{m}$ instead of $z = -10\,\mathrm{m}$

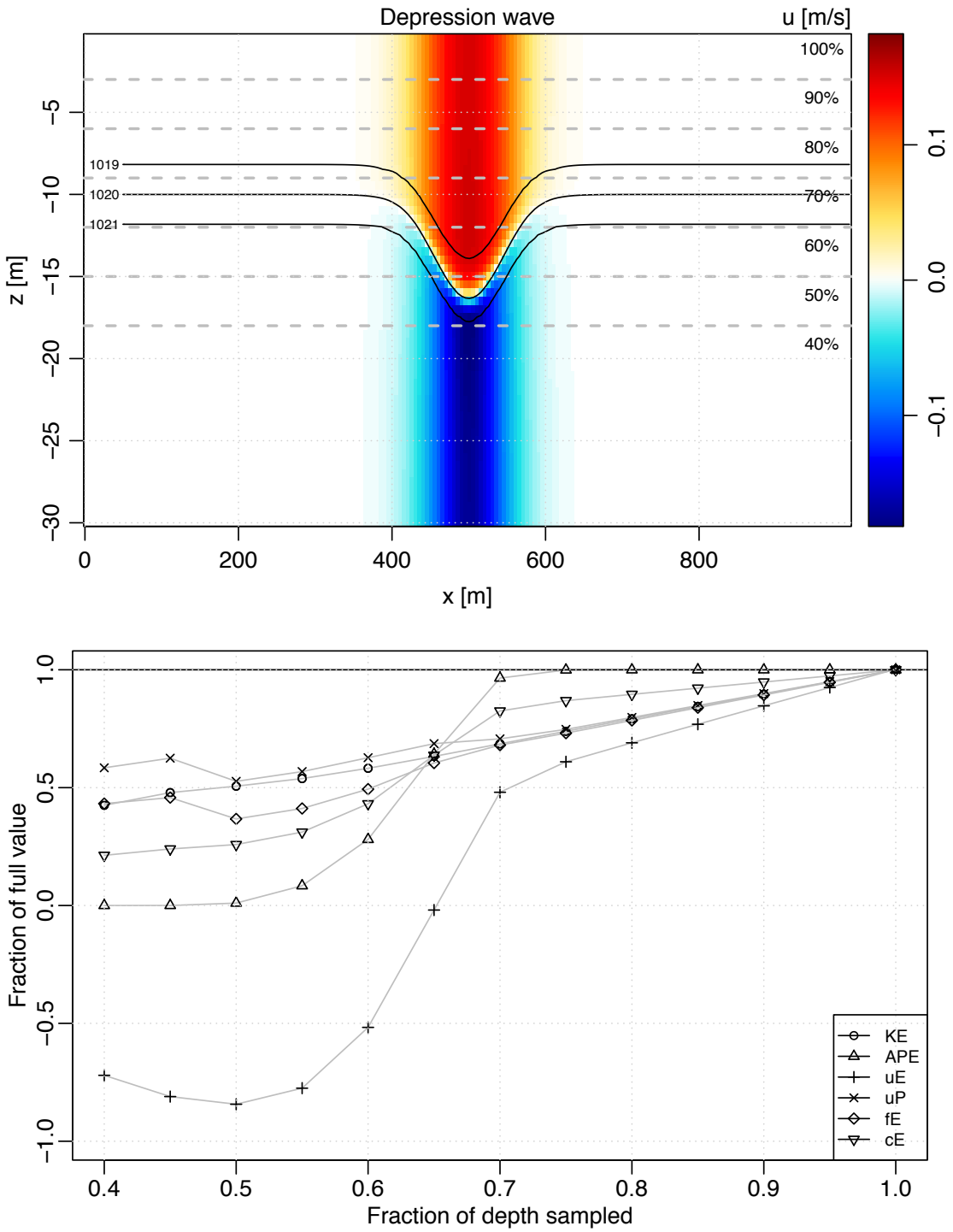

Figure 5.5: Under-sampling effect for an internal solitary wave of depression. Top: u velocity field, with density contours indicated by the solid lines. The dashed grey lines indicate the levels at which the full field was subsampled for estimating the error in energies and energy fluxes. Bottom: effect on energy and energy fluxes of incomplete sampling of the water column.

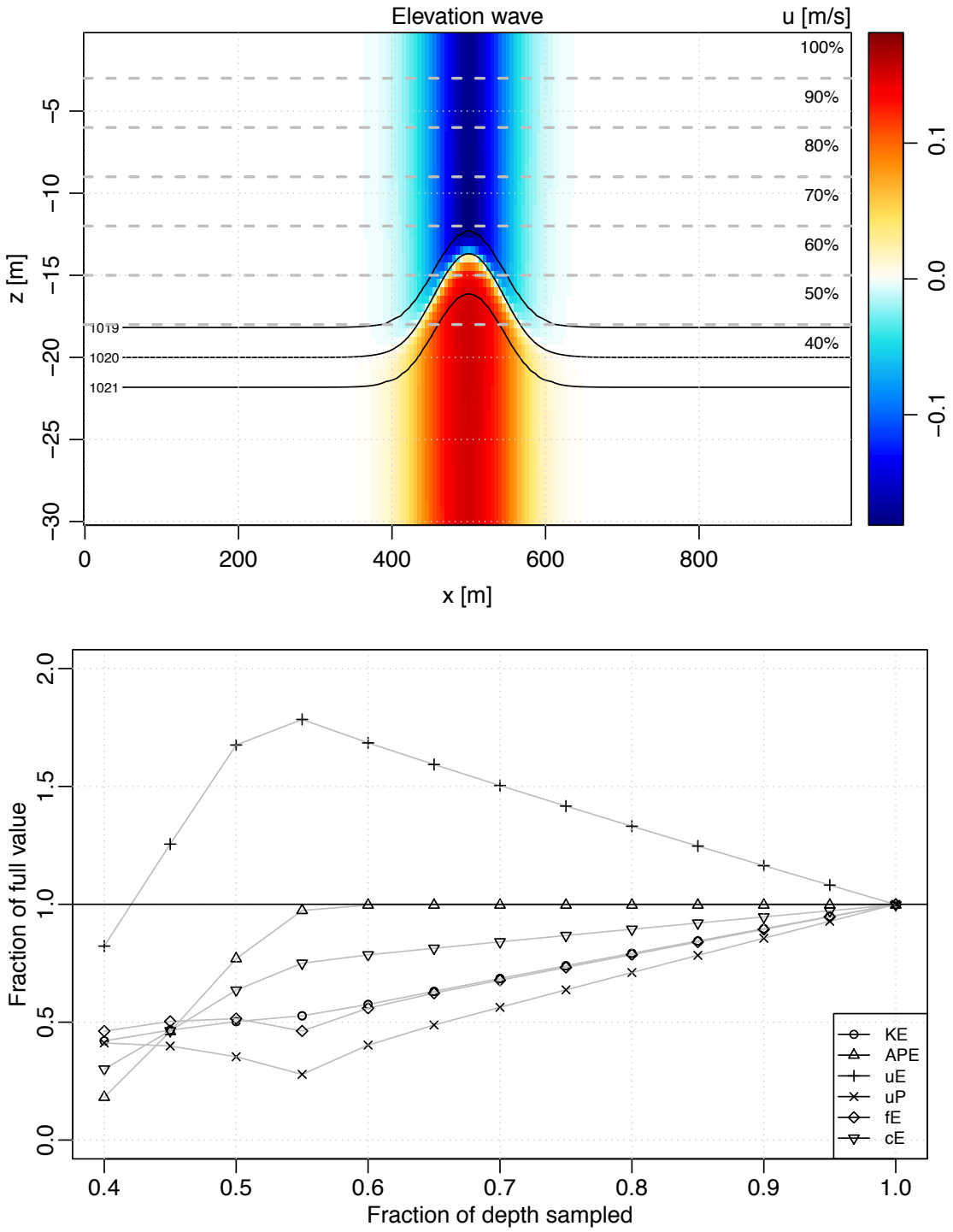

Figure 5.6: Under-sampling effect for an internal solitary wave of elevation. Top and bottom as in Figure 5.5.

always closer to the true value when the measurements extend above the pycnocline. This is a useful result, as measuring the total energy of a wave requires only resolving E_k and E_a, and is not limited by the assumptions involved in reconstructing the wave-induced pressure field. Particularly problematic for a dataset that is limited in the vertical will be the calculation of the external hydrostatic pressure, which requires knowledge of the near surface horizontal velocity (i.e. Equation 5.22). For the example presented in Section 5.2.3, the energy flux due to the external hydrostatic pressure is the only contributing term to the linear flux above the pycnocline, with a maximum magnitude approximately 2/3 of the total.

The implications for SLEIWEX moorings are most pronounced for the *M07* RDI ADCP, which was configured to sample to a distance of 18.25 m above the instrument. The water depth, determined from the pressure measured by the instrument, ranges between 20 and 25 m, corresponding to a coverage of 90% to 73%, respectively. The phase at which most waves are observed is during the rising tide (see Figure 3.10), corresponding to approximately 80–85% coverage. Using Figures 5.5 and 5.6 as a guide suggests that estimates of KE, APE, and $\langle f_E \rangle$ will be within 15–20% of the true values, in the absence of other sources of uncertainty.

Correction for Under-Sampling

In cases where the truncated sampling was believed to be most prominent, several schemes for correcting the measurements were attempted. The procedure settled on, described below, involved extrapolating both the velocities and the streamfunction separately.

The horizontal velocity was extended to the boundaries by extending the values from the topmost (bottommost) to the surface (bottom). This is an approximation to using the horizontal structure function for a first mode internal wave, however, the difference was found to be negligible and so the simpler method was implemented here. The vertical velocities were extended from the outermost bins using a linear extrapolation to zero at the boundary – again an approximation to using the vertical structure function.

As the density field is inferred from the streamfunction, it must also be extended to match the domain of the extended velocity field. The simplest method to achieve this is to use the extended velocities for the ψ relaxation. Effectively, setting $w = 0$

on the upper and lower boundary imposes constant values for the streamfunction there. This result is physically realistic for a flat-bottom case, as streamlines should not intersect either of the boundaries (which would imply flow into or out of the boundary). For a sloped bottom setting $w = 0$ on the lower boundary is questionable. Beyond this, experiments revealed that when applied to data, this method produced distorted streamlines, due primarily to the boundary integration correction discussed in Section 4.3.1. The effect of doing the boundary value correction to ensure that ψ is continuous around the boundary changes the constant value along the upper and lower boundaries to be linear in x. The overall effect on the inferred streamlines is to produced a slant that is unphysical.

An alternative method is to calculate the streamfunction using the truncated velocities, and then extend it to the boundaries independently. This eliminates the boundary value correction problem, but it has the disadvantage that the extrapolated streamfunction is dependent on the method used to extend it. Various methods were tested, among them: constant value extrapolation, simple linear extrapolation, and extrapolation using the vertical structure function. The method that produced the most sensible streamfunction field was to use linear extrapolation on every ψ profile to determine the value at the boundary ($z = 0$ or $-H$), and then extrapolate each profile to the maximum (or minimum) value. This has the effect of retaining horizontal streamlines (and therefore isopycnals) along the boundaries, without introducing any unrealistic spatial gradients to the ψ field.

5.3 Application to SLEIWEX 2008 Data

In this section, the methods described thus far are applied to ADP data from the SLEIWEX 2008 experiment, beginning with a discussion of the sources of uncertainty. The results presented this section aim to characterize the spatial structure of the observed internal wave fields (including energies and energy fluxes), and to compare the overall energetics with waves sampled in other regions. Finally, a particular wave event will be discussed, highlighting the utility of the developed techniques for assessing internal wave energies.

5.3.1 Measurement Uncertainties

It was found that an estimate of the uncertainties involved in calculating the various energy and flux fields from ADP data is difficult to determine accurately for individual events. In cases where many measurements are used together to fit a relationship (see later sections, in particular Sections 5.3.2 and 5.3.4), the uncertainties in the fit can be assessed through the scatter in the data.

Some of the uncertainty can be estimated using Figures 5.5 and 5.6, if it is assumed that under-sampling of the velocity field dominates the error. From Section 5.2.4 it is expected that the integrated flux $\langle f_E \rangle$ will be within about 15-25% of the true value, though the specific contributions from each term will varying depending on the wave. The uncertainty due to under-sampling for $\langle c\mathcal{E} \rangle$ should be smaller than that for $\langle f_E \rangle$ (approximately 5–10%).

The ambiguity of the proper reference state for the calculation of available potential energy also contributes some uncertainty. This was explored by calculating the range of APE determined by sorting in either a closed or "infinite" domain, yielding variations in APE of about $\pm 10\%$. Based on Section 5.2.4, uncertainty in KE should be too small by about 10%, though incomplete removal of the background flow will tend to increase KE.

Errors in the inferred wave speed and direction may contribute to the overall uncertainty, as they are used with the streamfunction method to infer $\rho_w(x, z)$, which in turn is used to calculate the wave-induced hydrostatic pressure field, the available potential energy, and the heaved background velocity. Tests with the speed and direction altered by $\pm 10\%$ did not visibly affect the inferred streamlines, and from the days for which photogrammetry was available (July 1st and 2nd), the propagation direction measured using the modal method (*Mirshak and Kelley*, 2009) was generally 5° of the true direction. Uncertainty from the wave speed and direction is therefore considered to be small relative to the other sources discussed above.

5.3.2 Measurement Methods

The method described thus far was applied to distinct internal wave and internal wave group signals observed in the SLEIWEX 2008 mooring data. It was not possible to apply the procedure generally to every wave visible in the data, due to a variety of reasons, summarized below.

1. Small amplitude waves: Waves for which the amplitude was below a certain level were unsuitable for the method, due to a failure of the streamfunction technique. This level was determined through trial and error, and a rough criterion was developed for the wave amplitude to exceed the vertical bin separation by a factor of about 10. This varied somewhat depending on the depth of the pycnocline, due to the beam spreading effect.

2. Severely under sampled waves: as discussed in Section 5.2.4, the method could not be applied to waves for which the pycnocline was beyond the range of the ADP. In some cases the data extension methods were applied, though in many instances, especially when the pycnocline was near the surface (e.g. see Figure 3.7) the energy and flux measurements were clearly erroneous.

3. Difficulty in separating the background flow from the wave field: This generally occurred when the background was changing on a time scale short relative to the times of the waves, and the velocities measured prior to wave arrival could not be considered constant over the duration of the wave.

4. Difficulty separating adjacent waves: In some cases the horizontal separation between waves was small enough that velocity signals were smeared between them. This may be caused by the beam separation, but also potentially by the overlapping of wave signals (either during shoaling as they slow down, or due to interacting waves of different origins). One consequence of this is that the wave velocity signals become convoluted, which affects the estimate of E_k and the flux terms involving u. Further, because of the use of velocity data to derive the streamlines, the inferred isopycnals may be a poor representation of the true heaved field. This was generally inferred qualitatively by examining the backscatter signal from the ADP, however one indication that this was occurring was when the measured KE was significantly larger than the APE, often by a factor or 5 or 10.

5. Poor temporal and vertical resolution: For the ADPs deployed in the shallowest regions (i.e. *M04*, *M05*, and *M06*), the limited vertical and temporal resolution affected the reliability of the energy measurements. For example, *M05* (a Sontek ADP) was set to an ensemble averaging period of 20 s and a vertical bin size of

1 m. With a mean water depth of 18 m, the instrument height above bottom and rejection of near-surface bins meant that there were typically only about 10 bins remaining with usable data. For a 3 to 10 m amplitude wave signal, this was found to be inadequate to accurately measure all the fields required.

In total the method was applied to approximately 70 waves and wave groups, consisting of data from *M07* and *M09*. In cases where the method was applied to a signal consisting of more than one wave, it was assumed that the wave properties such as speed and direction were constant over the group.

Wave signals were isolated from the ADP data by manually identifying the locations where isopycnals returned to the level observed prior to wave passage. This was not always possible within a group of waves, and so in such cases the limits were chosen by selecting the time at which the isopycnals were closest to their pre-wave level before heaving by the next wave began. Background flow was removed by heaving an average velocity profile along the isopycnals, assuming that it remained constant for the duration of the wave. The background was determined using an average of the velocity field between one and two minutes before wave arrival, except cases where the waves were too close together and a shorter average of 30 s was used.

The upstream density profile was estimated from the background field derived from the TDR chain (see Section 3.4.2, Figures 3.6 and 3.7). Located at *M08*, it was approximately equidistant between *M07* and *M09*. For *M09*, the vertical structure from the TDR chain at the time of arrival of the wave was assumed to be the correct one. At *M07*, however, the TDR data were lagged according to the propagation speed of the wave, so that the profile used would be representative of the density structure before the arrival of the wave.

5.3.3 Spatial Structure of Energy Fluxes

Several recent studies have focussed on the detailed spatial structure of nonlinear internal waves, emphasizing the inapplicability of linear or weakly-nonlinear theories (*Moum et al.*, 2007b; *Lamb and Nguyen*, 2009; *Kang and Fringer*, 2010). In this section, a similar analysis of internal waves observed at the SLEIWEX site will be presented, along with a discussion of the applicability of the techniques.

To illustrate the application of the techniques to data from SLEIWEX 2008, a single wave of elevation observed by the ADCP at *M09* was examined in detail

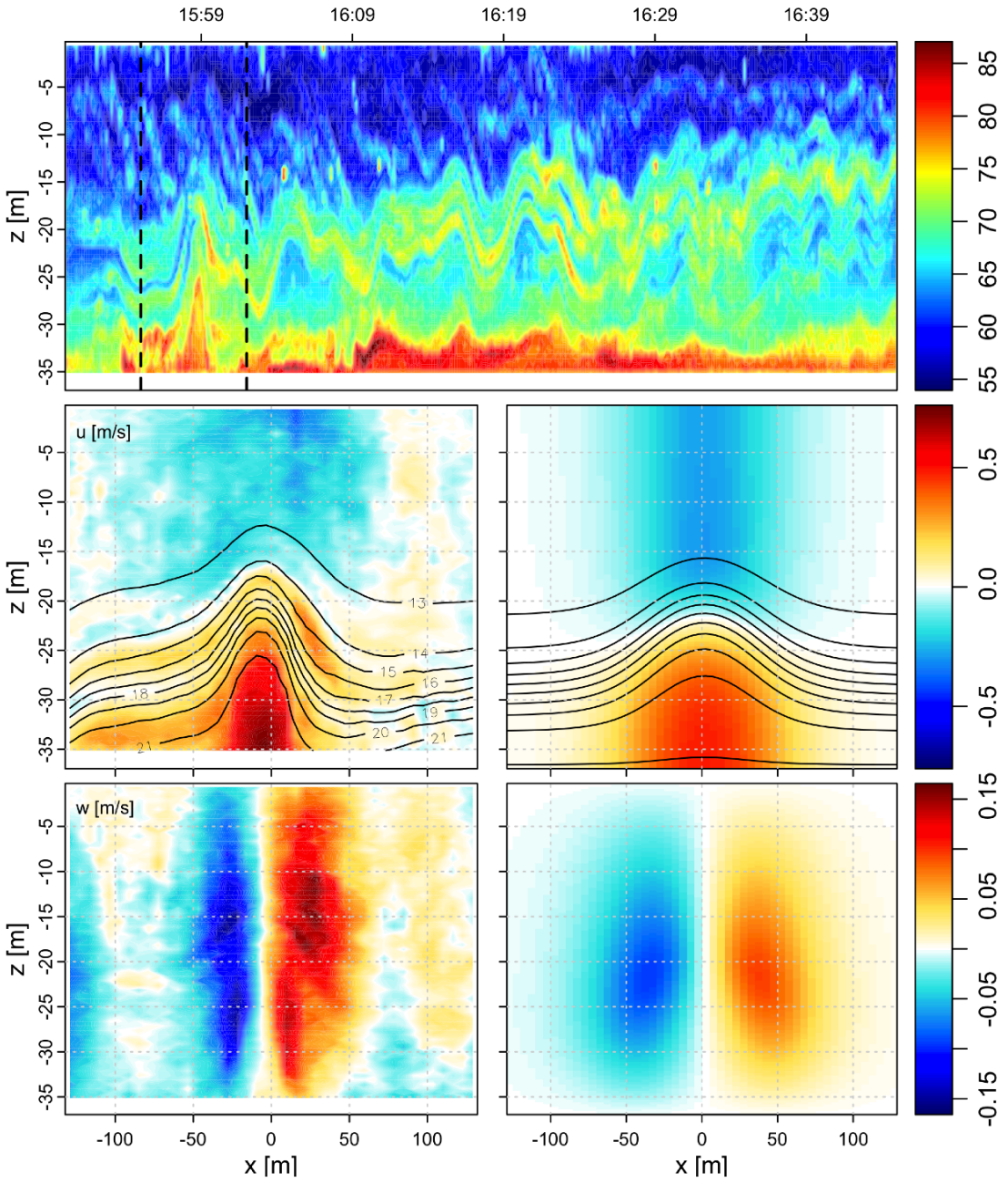

Figure 5.7: Backscatter and velocity fields for a wave of elevation. Top: acoustic backscatter for *M09* between 15:50 and 16:50 UTC on 2008-07-02. The dashed lines highlight the extent of the example wave in the lower panels. Bottom: u and w fields measured by the ADP (left), and as simulated by the nonlinear model of *Stastna and Lamb* (2002) (right). Contours of σ_θ are indicated by the solid lines.

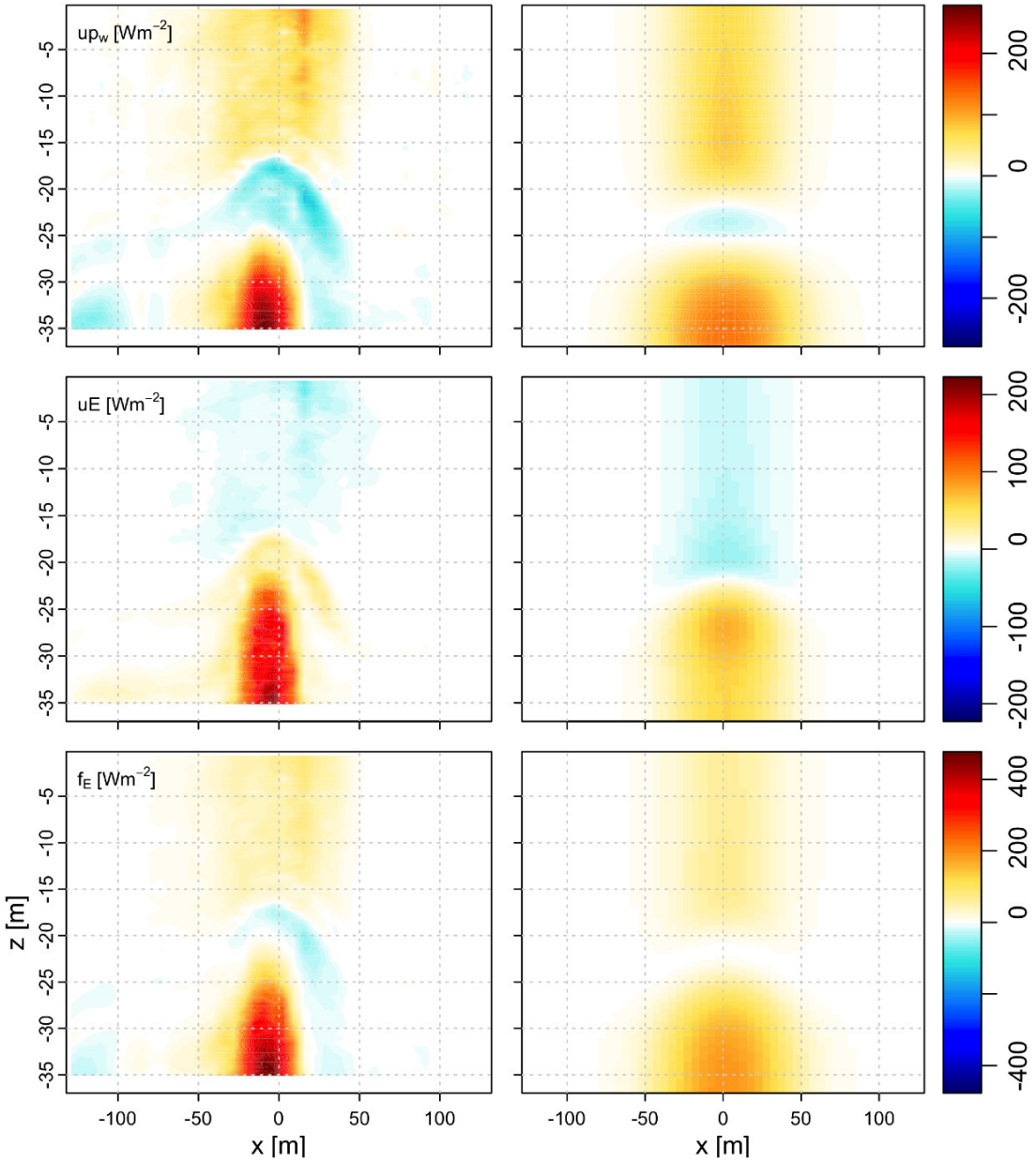

Figure 5.8: Energy flux fields for the wave of elevation in Figure 5.7. Fields for the observed wave are on the left and those of the modelled wave are on the right. Top: the linear energy flux up_w, middle: the nonlinear energy flux $u\mathcal{E}$, and bottom: the total horizontal energy flux f_E.

	Observed	Modelled
KE [kJ/m]	158 ± 8	144
APE [kJ/m]	129 ± 13	132
KE/APE	1.2 ± 0.1	1.1
$\langle up_w \rangle$ [kJ/m]	184 ± 19	232
$\langle u\mathcal{E} \rangle$ [kJ/m]	107 ± 11	48
$\langle f_E \rangle$ [kJ/m]	290 ± 30	280
$\langle c\mathcal{E} \rangle$ [kJ/m]	287 ± 14	278

Table 5.1: Summary of energy and energy transport for the observed and modelled waves in Figures 5.7 and 5.8. The uncertainties are approximate, based on Section 5.3.1.

(Figure 5.7). Arriving at *M09* at about 16:00 UTC on July 3 2008, the wave was the leading feature in an intense and complicated train of shoaling waves. The chosen wave is reasonably well separated from signals following it. Vertical density structure as inferred from the TDR chain is indicated in Figure 5.7, plotted as contours of σ_θ over the horizontal velocity. The pycnocline was located at about 27 m depth, with a nearly uniform upper layer. The density difference between the upper and lower layers was approximately $8\,\mathrm{kg/m^3}$.

For comparison, a solitary internal wave field with similar available potential energy was generated using the model of *Stastna and Lamb* (2002), with a vertical density structure nearly identical to the observed profile (see Appendix B). In comparing the velocity and density fields of the observed and modelled waves, there are clearly some differences. Although the heaving amplitudes of the waves are similar, the observed wave is inferred to be narrower than predicted by the nonlinear theory. Accordingly, the horizontal and vertical velocities of the observed wave are more intense (See Figure 5.7, second and third rows). The reason for the difference between the two waves may be due to the sloping bottom (not accounted for in the model) or to the the interaction with the weak (but nonzero) background current.

The spatial structure of the various fluxes for both the observed and modelled

waves are presented in Figure 5.8, including the linear, nonlinear, and total flux terms (up_w, $u\mathcal{E}$, and f_E respectively). The fields are similar between the two waves, with the main difference being that the magnitude of the fluxes are enhanced within the observed wave core. The linear energy flux is negative in the interface and positive above and below. The nonlinear energy flux has the reverse pattern, being asymmetric around the interface, with positive fluxes in the wave core and weak negative fluxes above.

Integrating over time and depth to obtain the total energy transport reveals some differences, summarized in Table 5.1. The total energy transported by $\langle f_E \rangle$ for the two waves is almost identical, despite the fact that the linear and nonlinear portions are distributed differently. While the integrated linear energy transport $\langle up_w \rangle$ makes up the bulk of the total in both cases, for the observed wave the contribution from the nonlinear energy transport $\langle u\mathcal{E} \rangle$ is more than double that of the modelled wave (38% and 17% respectively). This is perhaps not surprising given the previously noted differences in wave steepness and velocity magnitude – a steeper wave with stronger velocities will tend to be more nonlinear. Correspondingly, while the APE values are approximately the same, the KE of the observed wave is higher than the modelled one.

The agreement in the distributions of the fluxes (and to some degree the integrated values) between the two fields lends confidence to the measurements using the ADP data.

5.3.4 Energy Partition

Recent studies of nonlinear internal waves have sought to characterize the partitioning of energy between kinetic and available potential energy, and also to assess the nonlinear contribution to the energy flux (see e.g. *Klymak and Moum*, 2003; *Klymak et al.*, 2006; *Scotti et al.*, 2006; *Moum et al.*, 2007b; *Lamb and Nguyen*, 2009). In this section, the properties of the waves observed at the SLEIWEX site are examined, focusing on the distribution of energy and energy flux.

Figure 5.9 (left panel) compares the measured kinetic and available potential energies. After removal of one outlier from the regression analysis[2], the data support

[2]Leverage of the point to the regression is significant, changing the inferred slope by a factor of

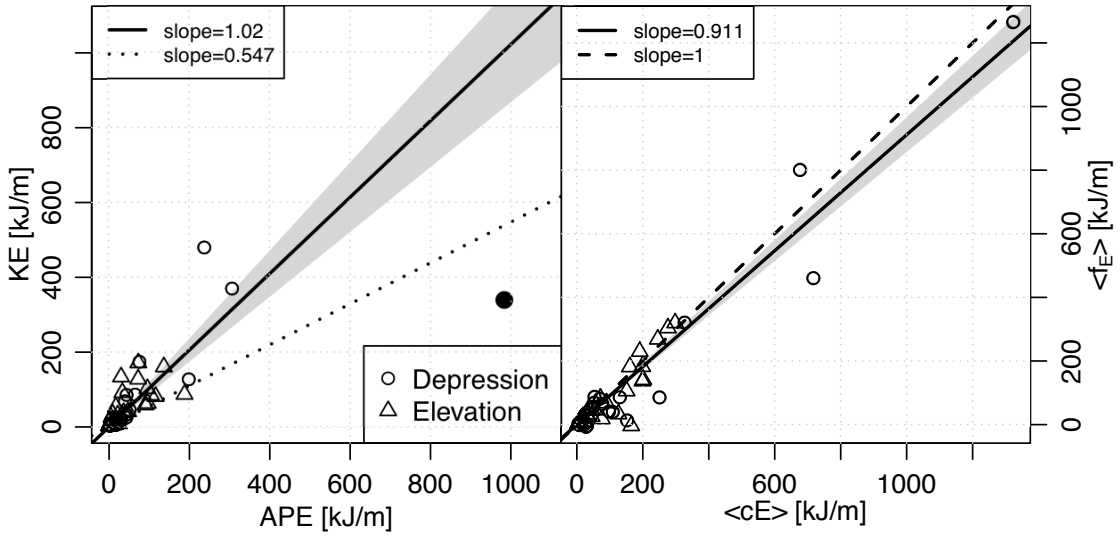

Figure 5.9: Measured internal wave energies and fluxes. Left: kinetic vs available potential energy for all observed waves. Circles represent waves of depression and triangles waves of elevation. The solid line indicates a least-squares fit through the origin, excluding the outlier discussed in the text, indicated by the filled circle. The dotted line indicates the linear fit with the outlier included. Right: the integrated energy flux $\langle f_E \rangle$ vs $\langle c\mathcal{E} \rangle$. The solid line is a linear fit through the origin and the dashed line indicates a slope of unity. The grey shaded areas indicate 95% confidence limits on the prediction from the fit.

an approximate equipartition between KE and APE. However, there is a large amount of scatter. A best-fit line through the origin results in a slope of 1.02 ± 0.15 (R^2 of 0.73, $p < 2 \times 10^{-16}$, where the $\pm$ represents the 95% confidence interval). The results are consistent with previous observations of nonlinear internal waves from different oceanic locations, including Massachusetts Bay (*Scotti et al.*, 2006), the New Jersey and Oregon continental shelves (*Shroyer et al.*, 2010a; *Moum et al.*, 2007b), and the South China Sea (*Klymak et al.*, 2006). The variability observed here is possibly a consequence of the fact that the waves sampled by the moorings will be observed during different stages of propagation and shoaling, depending on the depth of the pycnocline relative to the mooring. This concept will be explored further in Section 5.3.5.

Comparing the integrated energy flux $\langle f_E \rangle$ with $\langle c\mathcal{E} \rangle$ reveals that overall the two quantities are well correlated (Figure 5.9, right panel). A linear regression through

2. Closer examination of the point in question reveals that it is a train of near-surface depression waves at *M09*, suggesting that the KE is likely underestimated.

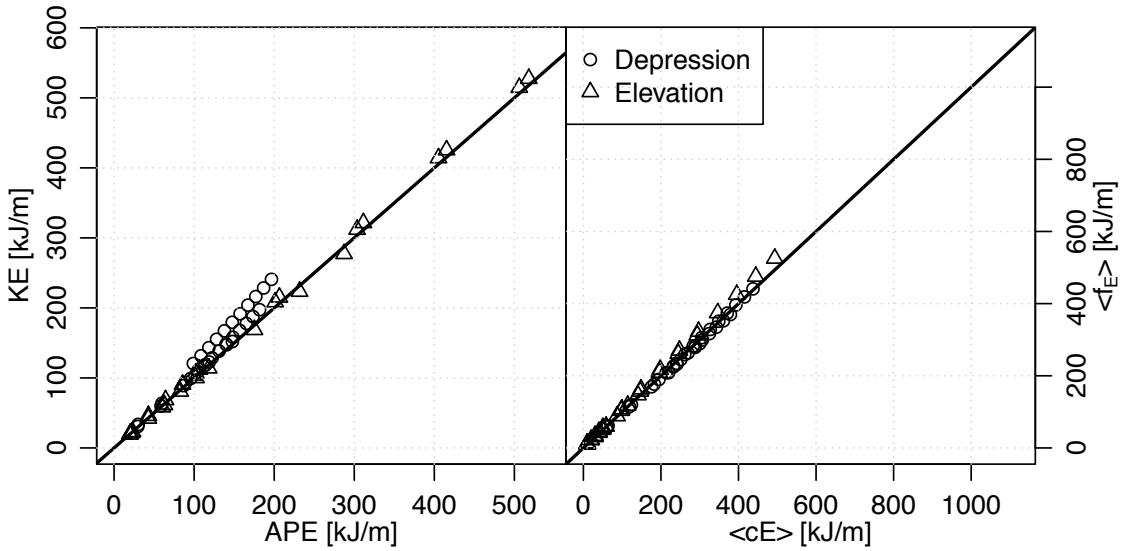

Figure 5.10: Modelled internal wave energies and fluxes. As in Figure 5.9 but for data generated using the fully nonlinear model of *Stastna and Lamb* (2002). The solid lines indicate a slope of unity.

the origin produces a line of slope 0.91 ± 0.05 (R^2 of 0.941, $p < 2 \times 10^{-16}$). Estimates of the energy transport using $\langle c\mathcal{E} \rangle$ typically exceed those using $\langle f_E \rangle$, as expected based on the tests with incomplete data in Section 5.2.4.

For comparison, Figure 5.10 presents the same quantities as Figure 5.9 but for a series of modelled wave fields generated using the model of *Stastna and Lamb* (2002). For certain stratifications and wave energies, KE is predicted to be slightly larger than APE but overall a 1:1 relationship is a good approximation. Figure 5.10 also highlights that the integrated energy flux measured using $\langle c\mathcal{E} \rangle$ is identical to $\langle f_E \rangle$.

5.3.5 Evolution of Wave Properties During a Shoaling Event

In this section, a specific shoaling event will be examined in detail, from the context of the measured energies and fluxes. The example highlights the skill of the stream-function technique for inferring isopycnals, and also the variability of KE and APE over short time scales.

The event to be focussed on in this section, presented in Figure 5.11, occurred on June 26 between 10:05 and 10:53 UTC, observed by the ADCP at *M07* (see Figure 5.11). Initially the pycnocline was centred at $z = -10\,\mathrm{m}$, with a density difference across it of about $6\,\mathrm{kg/m^3}$ and relatively uniform layers above and below. As the

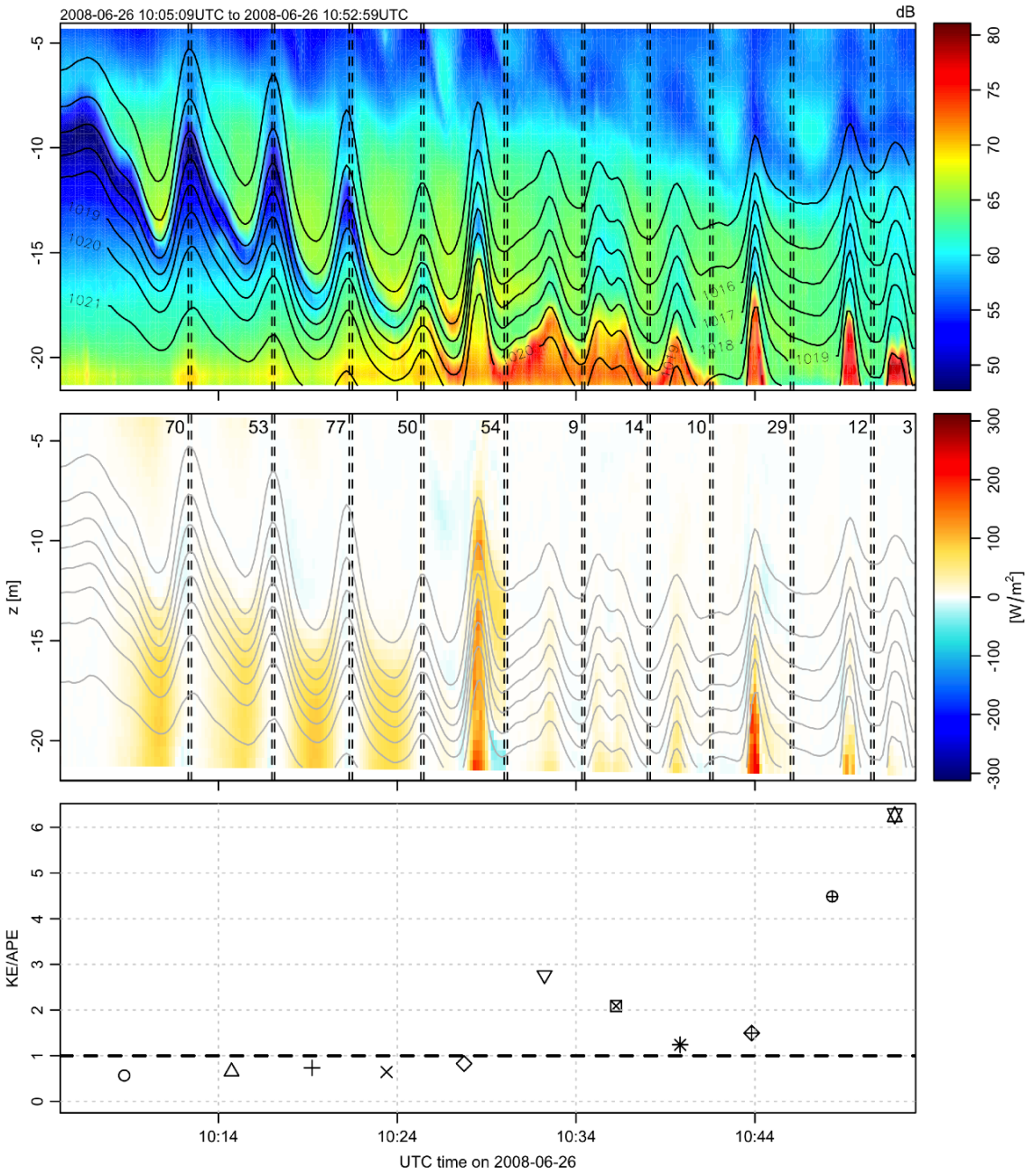

Figure 5.11: A shoaling wave event observed on June 26 at *M07*. Top: mean acoustic backscatter from the ADCP, with density contours determined using the streamfunction method overlain. Vertical dashed lines indicate the limits of the observed waves. Middle: energy density flux in f_E (in W/m^2), with the values integrated over each wave indicated in the upper corners (in kJ/m). Bottom: time series of the ratio of kinetic to available potential energy KE/APE. The symbols identify individual waves for reference in Figure 5.12

first large amplitude waves of depression arrived, the pycnocline began to deepen and by 10:25 was at $z = -18\,\mathrm{m}$. After this time, passing wave signals were observed as waves of elevation, propagating on the near-bottom waveguide.

The first 5 waves, propagating on the descending pycnocline, are visibly asymmetric, with a broad leading face and a steep, sharp trailing face (Figure 5.11, top panel). The shape of the waves observed at this time is consistent with waves of depression undergoing a transformation to waves of elevation as they pass through the "turning point" at which the nonlinearity parameter in the KdV equation passes through zero. This process has been observed in detail in numerical models (see e.g. *Mirshak*, 2008; *Aghsaee et al.*, 2010, their figures 5.7 and 16, respectively), but is difficult to observe in the field owing to an unpredictability in the turning point location and short time scales associated with the overturning. *Shroyer et al.* (2009) observed the process by tracking waves from a ship as they approached and passed the turning point. They describe a transformation that begins with increased speed in the front edge of the wave, causing asymmetry to develop which eventually gives way to a series of waves of elevation. They quantified the process in terms of the wave vorticity (depression waves have positive vorticity and elevation waves negative vorticity), the value of the KdV nonlinearity parameter (i.e. Equation 5.20), and by measuring the differential speeds and slopes of the front and rear faces. The leading face continues to broaden as the wave approaches the turning point, and eventually it becomes indistinguishable from zero, at which point the steep rear face emerges as a wave of elevation.

While *Shroyer et al.* (2009) were able to track the waves, and thus obtain repeated measurements of the same feature through time, here the measurements are limited to a fixed time series representation. The rapid transformation of the waves means that the assumption of constant form is likely only valid for the short time period as the wave crosses the mooring. It is impossible therefore to obtain a picture of the spatial patterns involved in the overturning in this manner.

Examination of Figure 5.11 however, reveals that the changing background conditions permit a slightly different view of the shoaling process. Effectively, as the pycnocline deepens over the course of the time period, the mooring sees a different portion of the shoaling wave train. In other words, the deepening pycnocline causes

the turning point to move farther offshore, permitting a view at the fixed point of all stages of the transformation process. Between 10:05 and 10:25 UTC, while the pycnocline is close to mid-depth, the observed waves correspond to the asymmetric disturbances leading up to the turning point – which at this time must be inshore of the mooring location. The near-bottom wave observed around 10:28 is distinct from the previous 4 waves in that the rear face is extremely steep, and the isopycnal displacement of the rear face is higher than the leading face. This wave may have passed the mooring very close to the instant at which the first of the developing elevation waves were forming. After 10:30, the observed signals are all near-bottom elevation waves, propagating along a wave-guide which is now closer to the bottom than the surface. By this time, the turning point is offshore of the mooring, and the observed signals are exclusively waves of elevation.

The second panel of Figure 5.11 shows the temporal structure of the inferred energy flux f_E, with the isopycnals super imposed for reference. Vertical dashed lines indicate the limits used for each wave signal and the numbers in the upper right corner of each box indicate the integrated energy flux $\langle c\mathcal{E} \rangle$ (in kJ/m) for each wave. The 5 waves leading the train contain between about 50 and 80 kJ/m each, compared to the trailing elevation waves which contain between 3 and 30 kJ/m. This may indicate the tendency of a depression wave to fission into a series of elevation waves as it overturns, with its energy being distributed accordingly.

Further details of the shoaling process are revealed by considering the partition of KE and APE, shown in the bottom panel of Figure 5.11, plotted as the ratio KE/APE. For the first 5 waves, for which overturning has yet to occur, there is seen to be an excess of APE ($KE/APE < 1$), possibly indicative of a conversion of kinetic to potential energy as the wave slows down and steepens, causing isopycnals at the rear face to steepen. Once the turning point has migrated offshore of the mooring location however, the ratio of KE to APE increases to be greater than 1. The exact reason for this excess of KE is unclear, though it is possible that the elevation waves observed here may already contain trapped cores. While the streamfunction technique didn't indicate any closed streamlines for this wave field, maximum velocities in the wave cores were observed to be larger than the wave propagation speed.

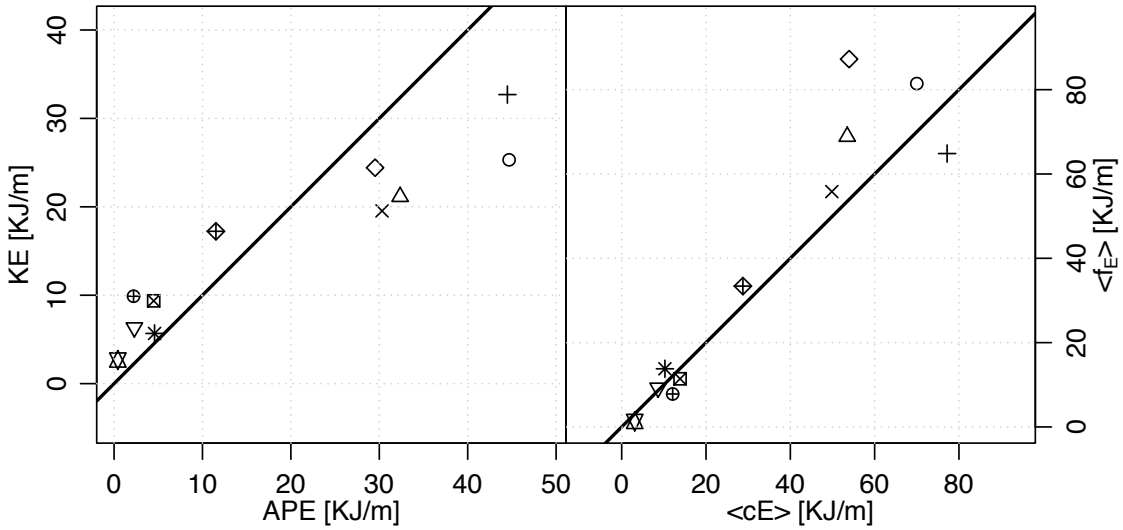

Figure 5.12: Measured internal wave energies and fluxes during the June 26 shoaling event. As in Figures 5.9 and 5.10, but for the 11 waves observed between 10:05 and 10:55 UTC. The solid lines indicate a slope of unity, and the symbols identify the individual waves, as seen in Figure 5.11.

This view is supported by Figure 5.12 (left panel), which presents the KE and APE values in scatterplot format similar to Figure 5.9. Further, the agreement between the integrated energy flux measured by $\langle f_E \rangle$ and $\langle c\mathcal{E} \rangle$ (Figure 5.12 right panel) lends credibility to the energy and flux measurements for this case.

5.4 Conclusions

In this chapter, the energetics of the internal wave field at the SLEIWEX site were examined in detail, making use of the streamfunction technique developed in Chapter 4 to infer the heaved density field.

The effects on the energy and energy flux measurements due to a limited sampling range were examined using synthetic datasets consisting of depression and elevation waves. Results indicate that although the measurements underestimate the energies and fluxes, reasonable values can be obtained when the ADP samples at least 3/4 of the water column and when the pycnocline is contained within the sampled region.

The spatial structure of various components of the energy flux was explored for a wave of elevation observed at *M09*. Comparison with a modelled wave of approximately the same available potential energy suggests that the energy and

flux measurements are reasonable, and reveals some differences from theoretical predictions. The observed wave is inferred to be narrower than the modelled wave, and the associated currents are correspondingly stronger. This is reflected in the energy flux measurements, where the nonlinear energy flux $\langle u\mathcal{E} \rangle$ makes up a greater proportion of the total flux than the modelled wave.

The energy in the wave field is approximately equally partitioned between kinetic and available potential energy on average, however there is considerable variability in this relationship. Examination of a short time scale event consisting of a shoaling internal wave train highlights this variability, which may result from evolution of the background waveguide relative to the fixed mooring.

The relation $\langle f_E \rangle = \langle c\mathcal{E} \rangle$ appears to hold for the waves observed in this study, implying that over short timescales $\rho\epsilon$ is negligible compared to $\partial f_E / \partial x$. The uncertainty in $\langle c\mathcal{E} \rangle$ due to limited sampling is less than for $\langle f_E \rangle$, which when combined with the fact that the measurement uncertainties for $\langle f_E \rangle$ are generally larger, indicates that $\langle c\mathcal{E} \rangle$ is a better estimate of the horizontal internal wave energy flux.

Chapter 6

Measurements of Turbulence

Many recent advances in the understanding of nonlinear internal waves and turbulence have arisen from field observations on continental shelves. The measurements reveal a complicated picture of the shoaling process and the effects on mixing and lateral transport of both fluid and turbulence. *Klymak and Moum* (2003) observed near-bottom waves of elevation on the Oregon continental shelf, with high values of turbulence dissipation within the waves. A more detailed study by *Moum et al.* (2007b), including time series and vertical profiles of turbulence, revealed that turbulence decayed more rapidly than the local buoyancy time scale, and those authors concluded that turbulent fluid was transported within the wave cores and not being left behind to decay. On the New Jersey shelf, shoaling nonlinear internal waves have been observed to undergo polarity reversal from waves of depression to waves of elevation (*Shroyer et al.*, 2009), while experiencing dissipative losses during propagation (*Shroyer et al.*, 2010a). Vertical heat flux associated with the waves was observed to be an order of magnitude larger than the background, due to enhanced diffusivities at the pycnocline (*Shroyer et al.*, 2010b). Farther inshore from the continental shelf, over a rough barrier reef, *Davis and Monismith* (2011) observed elevated near-bottom turbulence associated with passing internal waves, concluding that the waves significantly modified the structure of the turbulent bottom boundary layer on the reef.

Near the SLEIWEX 2008 field site, *Bourgault et al.* (2008) observed a series of up-slope propagating waves in detail using a vertical microstructure profiler, but measurement limitations prevented identifying the source of the turbulence. More

recently, in the lower St. Lawrence Estuary, *Cyr et al.* (2011) found that boundary mixing was important in the decay of a cold intermediate layer. The source of the boundary mixing, either from shoaling internal waves or bottom-boundary layer processes, is unknown.

In this chapter, measurements of turbulence inferred from the bottom-mounted ADVs will be presented, with emphasis on the turbulence associated with internal waves. Relevant theory is reviewed in Section 6.1. The method used for estimating ϵ is discussed in Section 6.2 along with criteria for assessing the quality of the data. Results are presented in Section 6.3.

6.1 Theory

This section will introduce and review the foundations of turbulence theory, to shed light on the methods behind such measurements in the ocean. The primary quantity of interest is ϵ, the rate of dissipation of turbulence kinetic energy per unit mass (often called simply the dissipation rate). The following subsections will present a derivation of the turbulence kinetic energy (TKE) equation, followed by a spectral representation that is the basis for measuring ϵ used in this thesis.

6.1.1 Turbulence Kinetic Energy Equation

An equation for the total kinetic energy of a flow can be obtained by taking the dot product of the Navier-Stokes equations under the Boussinesq approximation,

$$\frac{\partial u_i}{\partial t} + u_j \frac{\partial u_i}{\partial x_j} = -\frac{1}{\rho_0}\frac{\partial p}{\partial x_i} - g\frac{\rho}{\rho_0}\delta_{i3} + \nu\frac{\partial^2 u_i}{\partial x_j^2}, \tag{6.1}$$

and u_i, where (u, v, w) are indicated by the subscripts $i = 1, 2, 3$ using the summation convention. The velocity, pressure, and density are expressed as a Reynolds decomposition into time-mean (overbar) and fluctuating parts (prime), according to

$$u_i = \overline{u}_i + u_i' \tag{6.2}$$

$$p = \overline{p} + p' \tag{6.3}$$

$$\rho = \overline{\rho} + \rho'. \tag{6.4}$$

An equation for the kinetic energy of the mean flow can be constructed similarly,

by first taking a time average of Equation 6.1 and then multiplying by $\overline{u}_i$. Subtracting the mean kinetic energy equation from the total gives an equation for the turbulence kinetic energy, or TKE, as

$$\frac{D}{Dt}\left(\frac{1}{2}\overline{u_i'u_i'}\right) = -\frac{\partial}{\partial x_j}\overbrace{\left(\frac{1}{\rho_0}\overline{p'u_j'}}^{1} - \overbrace{\frac{1}{2}\overline{u_i'u_i'u_j'}}^{2} + \overbrace{2\nu\overline{u_i'e_{ij}}}^{3}\right) \underbrace{- \overline{u_i'u_j'}\frac{\partial\overline{u}_i}{\partial x_j}}_{4} \underbrace{- \frac{g}{\rho_0}\overline{u_3'\rho'}}_{5} - \underbrace{2\nu\overline{e_{ij}e_{ij}}}_{6} \tag{6.5}$$

where e_{ij} is the strain rate tensor for the fluctuating component, defined by

$$e_{ij} = \frac{1}{2}\left(\frac{\partial u_i'}{\partial x_j} + \frac{\partial u_j'}{\partial x_i}\right). \tag{6.6}$$

The first 3 terms on the RHS of Equation 6.6 represent spatial redistribution of TKE, the first two by the turbulence itself and the third via viscous transport. The fourth term on the RHS represents the shear production of TKE by interaction of the Reynolds stress $\overline{u_i'u_j'}$ with the mean velocity gradient. It is usually negative, implying a gain of TKE at the expense of the mean flow. The fifth term is the buoyant production (or destruction, depending on the sign) of TKE, also called the buoyancy flux.

The final term $2\nu\overline{e_{ij}e_{ij}}$ is the rate of dissipation of TKE (per unit mass), usually represented by ϵ. It represents a loss of TKE to viscous dissipation, and is the main quantity of interest used throughout this chapter for characterizing turbulence.

For steady-state homogeneous stratified shear flow turbulence, the TKE equation can be reduced to

$$\overline{u'w'}\frac{\partial\overline{u}}{\partial z} + \overline{v'w'}\frac{\partial\overline{v}}{\partial z} = -J_b - \epsilon, \tag{6.7}$$

where the terms on the RHS represent shear production of turbulence P, and J_b is the vertical turbulent buoyancy flux, equal to $\frac{g}{\rho_0}\overline{w'\rho'}$. If the buoyancy flux is small, such as in unstratified conditions, then Equation 6.6 reduces to a balance between shear production and viscous dissipation of TKE.

6.1.2 Length Scales of Turbulence

There exist a variety of spatial scales which are used to characterize aspects of a turbulent field. The largest is l, the energy production scale, which is a measure of the size of the turbulent eddies which contain a majority of the TKE. As a turbulent flow develops, energy input at the larger scales is transferred through nonlinear interactions to successively smaller scales. There is no general form for l, as it depends on the physical processes which are responsible for creating the turbulent flow.

A second relevant length scale is the Kolmogorov scale (*Kundu and Cohen*, 2002, Chapter 13.8), corresponding to the scale at which molecular viscosity dissipates the energy passed from larger scales. By dimensional considerations, the Kolmogorov scale l_k is

$$l_k = \left(\frac{\nu^3}{\epsilon}\right)^{1/4}. \tag{6.8}$$

Another relevant length scale, which exists only in the presence of stratification, is known as the Ozmidov scale (see e.g. *Kantha and Clayson*, 2000)

$$l_o = \left(\frac{\epsilon}{N^3}\right)^{1/2}, \tag{6.9}$$

which describes the scale of the largest isotropic eddies in steady-state stratified turbulence.

6.1.3 The Spectrum of Turbulence

A spectrum for the velocity field can be defined, $S(\mathbf{k})$, which describes the TKE as a function of the wavenumber vector, $\mathbf{k}$. If the turbulence is isotropic, the spectrum will be independent of the orientation of $\mathbf{k}$, and will depend only on its magnitude $k = |\mathbf{k}|$, giving

$$\overline{u'^2} = \int_0^\infty S(k)\, dk, \tag{6.10}$$

(*Kundu and Cohen*, 2002, Chapter 13.9).

For wavenumbers $k \gg l^{-1}$, there is no direct interaction between the turbulence and the motion of the large eddies. The form of the spectrum therefore does not depend on how much energy is present at large scales, where most of the energy is. If the spectrum in this range is assumed to depend only on the parameters of the

small scale flow, we can write

$$S = S(k, \epsilon, \nu), \quad k \gg l^{-1}$$

This range of wavenumbers is often called the *equilibrium range*. For $k > {l_k}^{-1}$, dissipation of energy by viscosity causes a sharp drop of $S(k)$. The range $l^{-1} \ll k \ll {l_k}^{-1}$, is called the *inertial subrange*, as in this range inertial forces dominate (*Kundu and Cohen*, 2002, Chapter 13.9). In this range the energy eventually dissipated by viscosity is passed from low to high wavenumbers through nonlinear interactions, and therefore the spectrum depends on ϵ but is independent of ν, i.e.

$$S = S(k, \epsilon), \quad l^{-1} \ll k \ll {l_k}^{-1}.$$

Dimensional analysis gives

$$S = A\epsilon^{2/3}k^{-5/3}, \quad l^{-1} \ll k \ll {l_k}^{-1}, \tag{6.11}$$

where $A \simeq 1.5$ is a universal constant determined experimentally. This result was first proposed by *Kolmogorov* (1941a,b), and as such is often referred to as *Kolmogorov's universal spectrum* (see *Batchelor*, 1953; *Tennekes and Lumley*, 1972; *Monin and Yaglom*, 1975, for further details and discussion). Equation 6.11 will be the basis for measurements of ϵ in this thesis, to be outlined in the following section.

6.2 Measuring ϵ

6.2.1 The Inertial Dissipation Method

Near-bottom turbulence dissipation rates were calculated from the high frequency velocity measured by the ADVs using the inertial dissipation method (see, e.g. *Huntley*, 1988; *Green*, 1992; *Kim et al.*, 2000). Assuming a balance between shear production of turbulence and viscous dissipation, a spectrum of the three-dimensional velocity variations will contain an inertial subrange provided there is sufficient scale separation between the two processes.

In practice, turbulence measurements generally make use of a one-dimensional spectrum (i.e. calculated from a single velocity component), which is a function

of the wavenumber in the direction of the mean flow k_1. In this case the energy spectrum can be written in a one-dimensional form, using the notation of *Huntley* (1988), as

$$\Phi_{ii}(k_1) = \alpha_i \epsilon^{2/3} k_1^{-5/3}. \tag{6.12}$$

Here i corresponds to the direction of the turbulent fluctuations (with $i = 1$ for longitudinal and $i = 3$ for transverse), and α_i is the corresponding one-dimensional Kolmogorov constant. For isotropic turbulence, α_3 is found to be 0.69 (*Green*, 1992; *Sreenivasan*, 1995).

A wavenumber spectrum $\Phi_{ii}(k)$ is developed from the frequency spectrum $\varphi_{ii}(f)$ using Taylor's "frozen turbulence" hypothesis which posits that the turbulence is advected past the sensor by the mean flow as a frozen eddy field, giving

$$\Phi_{ii}(k) = \frac{\varphi_{ii}(f)}{2\pi/\overline{U}}, \tag{6.13}$$

(*Tennekes and Lumley*, 1972; *Monin and Yaglom*, 1975), where $\overline{U} = (\overline{u}^2 + \overline{v}^2)^{1/2}$, (u, v) are the two horizontal velocity components, $k = 2\pi f/\overline{U}$ is the inferred wavenumber, and the overbar represents the mean over the time period used for the spectrum. *Huntley* (1988) suggests that this assumption is valid provided that $k\Phi_{ii}(k)/\overline{U}^2 \ll 1$.

In this study the spectrum of the vertical velocity component ($i = 3$) was used to estimate ϵ, for two reasons. First, because of the geometry of the transducer and receiver in the ADVs, the noise floor of the vertical component of velocity at high frequencies is lower than for horizontal velocities. Except perhaps at *M03* (see Figure 6.4), the noise floor of the ADVs was not observed in the vertical velocity spectra, given that the sampling rates (either 8 or 10 Hz) were well below the maximum sampling rate of the instruments. Second, in combined surface wave and mean flow conditions, the vertical velocities will be less contaminated by wave motion in the inertial subrange (*Stapleton and Huntley*, 1995). The fitting procedure and quality control tests are discussed in the next section.

6.2.2 Quality Control

The functional form of Equation 6.12 was fitted to the raw periodogram of vertical velocity calculated using a 1 minute period, which corresponds to either 480 or 600 data points, depending on the sampling rate (see Table 2.1). For periods longer than

1 minute, the validity of the frozen turbulence assumption is questionable, especially during times when internal waves were present. For shorter periods, the limited wavenumber range and the bias to the spectrum (see *Priestley*, 1981, Section 6.2.4) made it difficult to fit the functional form reliably. Consistent fits were obtained with lengths between 30 s and 2 minutes, and so a 1 minute period was chosen as a compromise.

The value of the slope, and the associated confidence interval of the fit were determined with a linear fit in log space using least squares. A "fit confidence" parameter was calculated as

$$QC_{ci} = \left| \frac{m + 5/3}{c_i} \right| \tag{6.14}$$

where m is the slope determined from the least squares fit, and c_i is the 95% confidence interval for the fit. A value of $QC_{ci} \leq 1$ indicates that a slope of $-5/3$ is within the 95% confidence interval of the fit. This approach is similar to one taken by *Feddersen* (2010) who rejected spectra if the best fit slope fell outside the range

$$m - 2\sigma_b - \beta < -5/3 < m + 2\sigma_b + \beta.$$

Here σ_b is the standard error of the fit, and β is a factor allowing for some leeway given that the statistics of the log spectra may not be Gaussian. Setting $\beta = 0$ corresponds to 95% confidence limits, much like the parameter QC_{ci} discussed above.

In addition to the fit confidence parameter, a "fit anomaly" parameter QC_{fa} was calculated as the percent difference between the fit slope and $-5/3$, i.e.

$$QC_{fa} = \frac{5/3 + m}{5/3} \times 100. \tag{6.15}$$

A qualitative visual inspection of a large number of spectra believed to be turbulent led to a quality threshold $QC_{fa} < 40$.

Two other test parameters, related to the quality of the velocity data used to calculate the spectrum are the "amplitude" and "correlation" parameters, QC_a and QC_c. If too few scatterers are present within the ADV sample volume, the strength of the return signal will be close to the system noise, and the corresponding velocity

ADV	f_s [Hz]	**Min. Corr. [%]**	**Min. Ampl. [counts]**
*M03*s	6	0.50	55
*M05*n	8	0.53	72
*M05*s	10	0.55	46
*M07*n	8	0.53	44
*M08*n	8	0.53	43
*M08*s	10	0.55	82

Table 6.1: Sampling frequencies and minimum correlation and backscatter amplitude thresholds for SLEIWEX 2008 velocimeters.

measurement will be inaccurate. The noise level of a particular device varies between manufacturers, and even between instruments. To determine the noise level for the ADVs used here, we examined time series of backscatter amplitude from times when the instrument was known to be operating in air. *Elgar et al.* (2005) rejected any data runs if more than 0.81% of the values were below the determined threshold. *Feddersen* (2010) used a less conservative value of 10% to retain more data, but used further techniques to patch or interpolate data points flagged as suspect before calculating the spectrum. The entire spectrum was rejected if $QC_a < 0.01$, based on *Elgar et al.* (2005), rather than make use of data replacement techniques (see, e.g. *Goring and Nikora*, 2002).

The backscatter correlation for each beam, ranging from 0 to 100, is a measure of the degree of coherence between the return signal from the pulse pairs used to determine the water velocity, and can be used to assess data quality (*Zedel et al.*, 1996; *SonTek*, 2001). Low correlation can be caused by rapid advection of scatterers from the sampling volume, by the instrument operating in air, a low signal-to-noise ratio, and hardware malfunctions. In addition, highly turbulent or sheared flow can result in reflection of the pulse pairs from different scatterers in the sample volume, also leading to low correlation. An along-beam correlation of 70% is recommended for high quality velocity estimation, though a minimum of 30% will still give accurate mean flows. *Elgar et al.* (2005) used a threshold of

$$\gamma_c = 0.3 + 0.4\sqrt{f_s/f_{max}}, \tag{6.16}$$

where f_s is the sampling frequency, and f_{max} is the maximum frequency of the

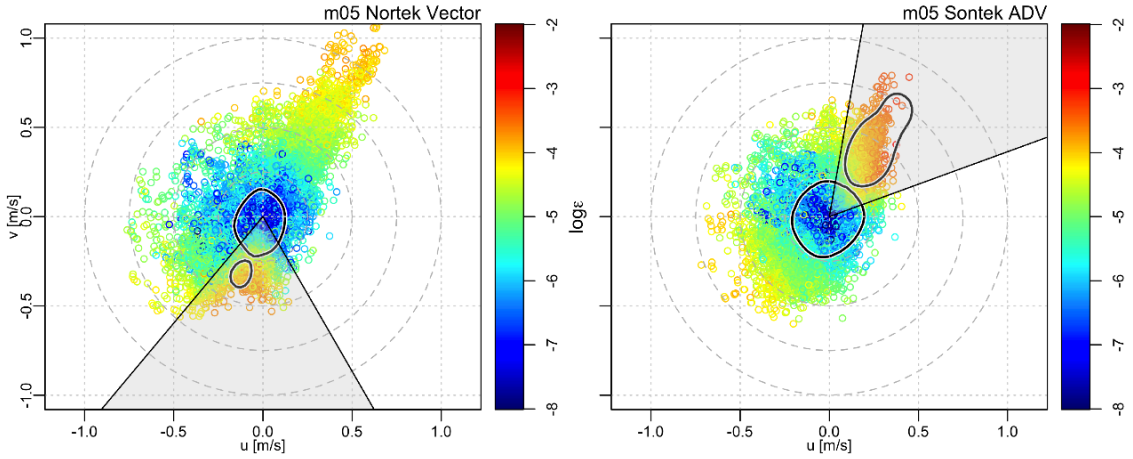

Figure 6.1: Hodographs of the two *M05* velocimeters, with color indicating the logarithm of the inferred dissipation rate. The region of high ϵ in the upper right quadrant (i.e. for flow to the Northeast) for the Sontek unit is suspicious, as is the (smaller) region for flow to the South for the Nortek unit. The overlaid contours indicate regions where quality control tests removed points; note the presence of two distinct groups in each plot. The shaded cones indicate the angles for which ϵ estimates were discarded, based both on the QC tests and the orientation of the frames relative to the flow (Figure 6.2)

instrument (e.g. 25 Hz for SonTek ADVs). For the ADVs used here, γ_c was 0.53 or 0.55, depending on the frequency (8 or 10 Hz – see Table 6.1). As with QC_c, a conservative value of 0.01 was chosen (the spectrum was rejected if more than 1% of the values were below the cutoff).

The frozen turbulence assumption leads to a final quality control check, QC_{ft}. After evaluating the mean value of $k\Phi/\overline{U}^2$, the spectrum is rejected if it is larger than 0.05.

Frame Interference

After applying the inertial dissipation method outlined in Section 6.2.1, and removing points which failed any one of the quality control tests, the data for each instrument were plotted as velocity hodographs color-coded for the dissipation rate. For illustration, the hodographs for the two *M05* velocimeters (Nortek Vector and Sontek ADV) are shown in Figure 6.1.

The difference between the two plots is striking, considering that they were only separated in the vertical by 35 cm. When currents were to the Northeast, the Sontek unit saw lower velocities, but significantly higher dissipation levels than the

Nortek unit. Alternatively, for flow to the South, the Nortek unit saw slightly higher dissipation rates. Locations of the majority of points removed by quality control tests are indicated by the contours. Each mooring shows a distinct region other than the one centred around $(0, 0)$ within which spectra were rejected. Most of the points in these regions were removed by the fit confidence parameter QC_{ci}, indicating that while the spectral level was very high ($\epsilon \sim 10^{-3}\,\mathrm{W/kg}$), the log spectral slope differed significantly from $-5/3$.

The large number of rejected spectra in the identified regions is attributed to vortex shedding off various elements on the instrument frame. The failure of the fit confidence parameter suggests that the strong high frequency flow sampled behind the frame was not fully developed turbulence. The relative orientation of the frames on the bottom, as well as a schematic of the *M05* mooring are shown in Figure 6.2. The Sontek unit, positioned at the end of the I-beam at a height of 65 cm, didn't extend above the height of the rest of the mooring, and was therefore in the lee of the frame for flow passing through it. This occurred during the falling tide, and therefore any dissipation data from these times were discarded, in addition to any spectra that failed the quality control tests.

The Nortek unit was positioned on the main frame, but at 98 cm HAB was clear of the bulk of the mooring. This is evident from Figure 6.1, in that the dissipation measured during the falling tide (upper right quadrant) appears uncontaminated. The anomalous region in the bottom of the plot, however, appears to have been caused by vortex shedding from flow past the Nortek Aquadopp, which extended out from the center support close to the level of the sampling volume. Data from these times were discarded.

Further analysis revealed that the other two pods also contained some data that were contaminated, in each case consistent with the orientation of the frame and the flow passing through it. The only velocimeter unaffected by this effect was the Nortek Vector at *M08*, which was mounted above the frame height, and had no downward looking ADP to cause interference. Angle ranges for which data were discarded are indicated by the grey cones in Figure 6.2 and in Table 6.2.

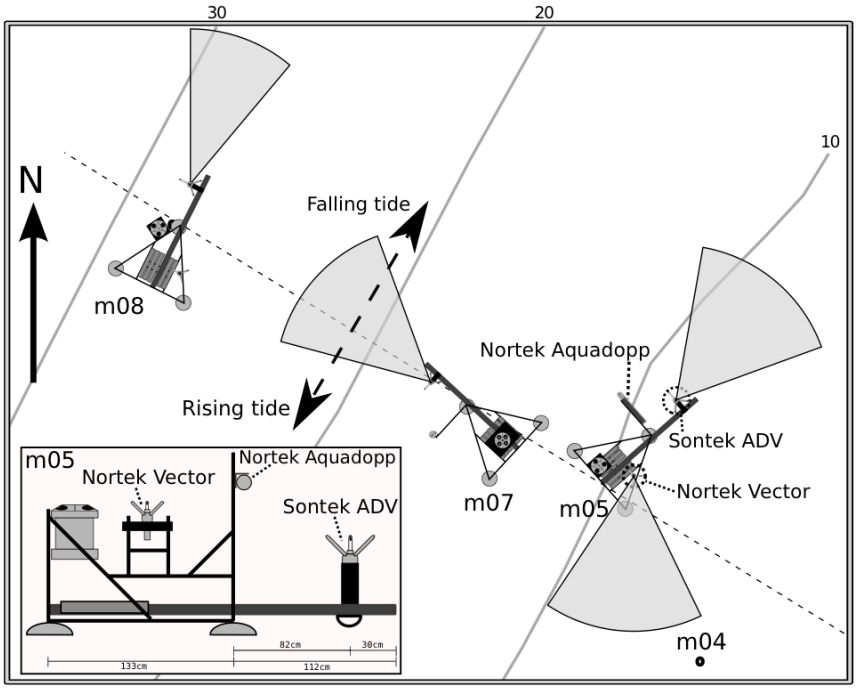

Figure 6.2: Orientation of the 3 "pod" moorings on the bottom. The size of the pods is exaggerated for clarity, but the positions relative to each other and the bathymetry (gray lines) are correct. The large dashed arrow indicates the typical direction of the tidal currents, which are mostly aligned with the bathymetry. Inset is a side-view of the *M05* pod, identifying the location of the two velocimeters and the Nortek Aquadopp. The Sontek ADV is in the lee of the frame for flow through it (flow to the Northeast). The Nortek Vector is in the lee of the Aquadopp for flow to the South. Flow angles for which frame shading is suspected for each instrument are indicated by the grey cones, identical to those in Figure 6.1.

Mooring	Angle
*M03*s	N/A
*M05*n	-130 to $-60°$
*M05*s	20 to 65°
*M07*n	110 to 165°
*M08*n	N/A
*M08*s	50 to 90°

Table 6.2: Angle ranges for which frame interference of the ADV velocities was suspected.

6.3 Results

6.3.1 Tidal Shear

In an unstratified boundary layer, the velocity profile may be assumed to follow the "law of the wall" form,

$$u(z) = \frac{u_*}{\kappa} \ln\left(\frac{z}{z_0}\right), \tag{6.17}$$

where u_* is the friction velocity, defined by $u_* = \sqrt{\tau_b/\rho}$, τ_b is the bottom stress, $\kappa = 0.41$ is von Karman's constant, and z_0 is a "roughness height" characteristic of the bottom roughness and composition (see e.g. *Soulsby* (1997) Chapter 3 and *Kundu and Cohen* (2002) Chapter 13.11). Within the turbulent boundary layer, the vertical velocity shear is given by

$$\frac{\partial u}{\partial z} = \frac{u_*}{\kappa z}. \tag{6.18}$$

Making the assumption that the Reynolds stress $\overline{u'w'} = {u_*}^2$ (i.e. that there is a constant stress layer), and that shear production and dissipation of TKE are in balance gives an estimate of the dissipation rate as

$$\epsilon = \frac{{u_*}^3}{\kappa z} \tag{6.19}$$

(see e.g. *Huntley*, 1988).

If the bottom stress follows a quadratic drag law, $\tau_b = \rho C_D u_b^2$, where u_b is the near bottom velocity and C_D is an appropriate drag coefficient, then u_* can be expressed in terms of u_b as $u_* = {C_D}^{1/2} u_b$. Substituting this into 6.19 gives

$$\epsilon = \frac{{C_D}^{3/2} U_f^3}{\kappa z}, \tag{6.20}$$

where the low-pass filtered near-bottom velocity has been substituted for u_b.

The relationship of dissipation rate to tidal flow for the *M05* Nortek Vector is shown in Figure 6.3. Here U_f is a 30 minute low-pass filtered horizontal speed representative of the longer time scale forcing expected for a tidal bottom boundary layer. Overall the data in Figure 6.3 agree with the $\epsilon \propto U_f^3$ model, however there is a significant amount of scatter around this line. At low velocities, the measured

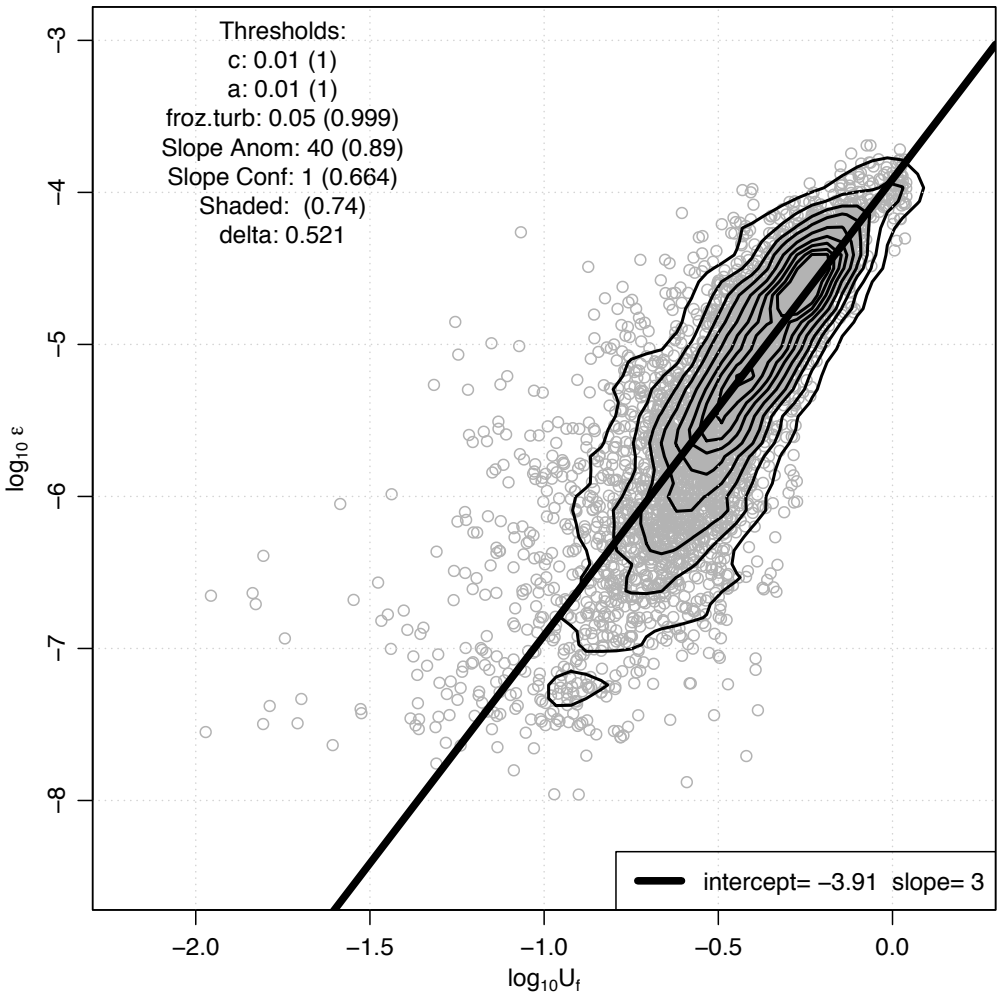

Figure 6.3: Comparison between ADV-derived U_f and ϵ for the Nortek Vector at *M05*. The individual points are plotted as grey circles, while the contours indicate data density (decreasing from 90% to 10%). The solid line is the result of a linear fit with a slope of 3. The listed thresholds show the values of the quality control tests, with the values in parentheses indicating the fraction of points remaining after bad points are removed. "Shaded" is the fraction of points remaining after removing those contaminated by flow disturbance, and "delta" is the fraction of all points remaining after all quality checks were applied.

dissipation is at times more than 2 orders of magnitude higher than predicted, which suggests that there may be processes responsible for increasing ϵ at low tidal velocities that are not accounted for using tidal shear scaling.

The drag coefficient C_D can be determined by fitting the data in log-space to

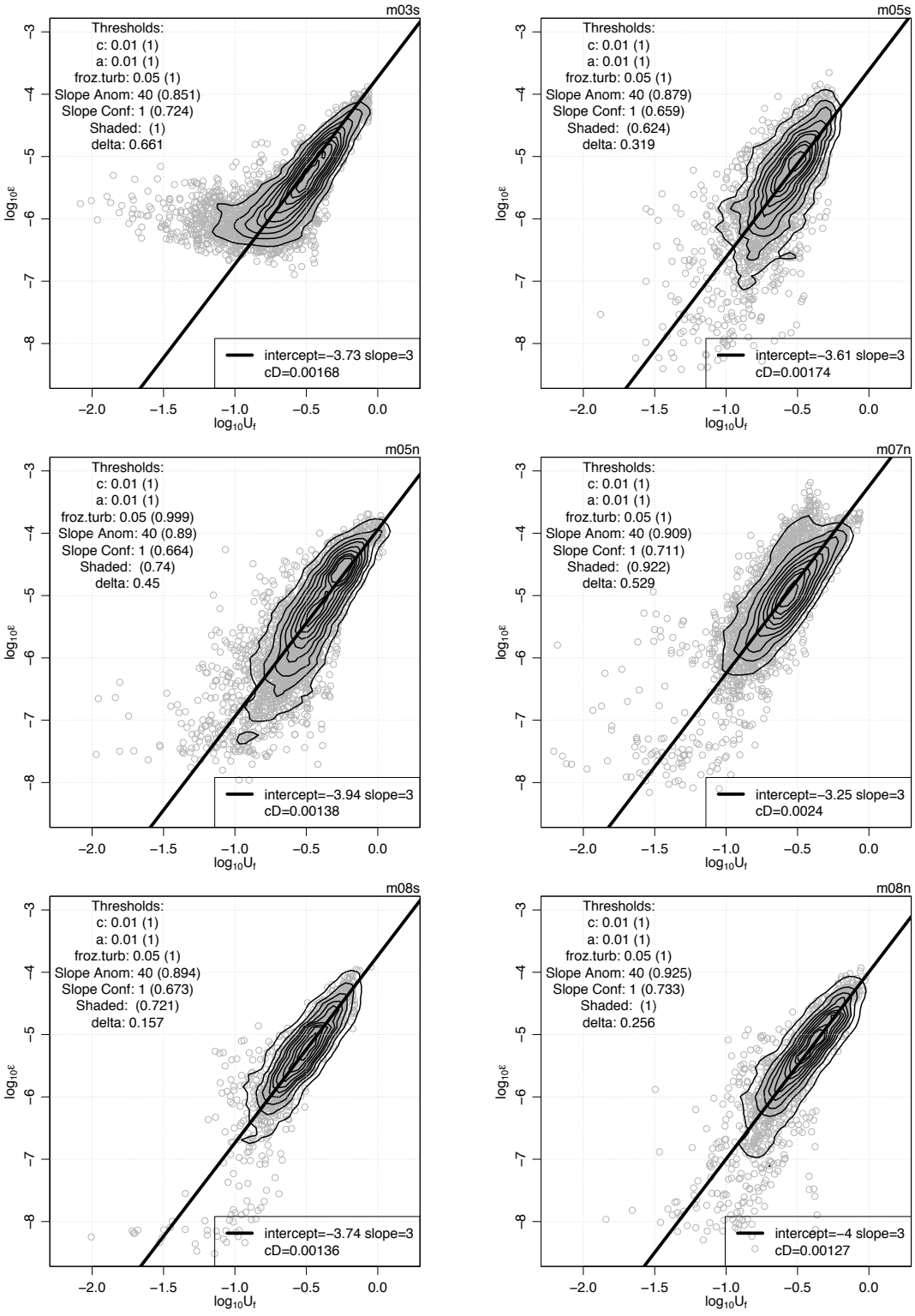

Figure 6.4: Comparison between ADV-derived U_f and ϵ, but excluding points when internal waves were present. Mooring name is indicated above the plot, where "s" stands for Sontek and "n" for Nortek units. The inferred C_D is indicated in the legend. Contour levels are as in Figure 6.3.

Equation 6.20, with a prescribed slope of 3, according to

$$\log_{10}\epsilon = 3\log_{10}U_f + \log_{10}\left(\frac{{C_D}^{3/2}}{\kappa z}\right). \tag{6.21}$$

ϵ values obtained during times when internal waves were present, as measured by the wave proxy, were excluded. C_D can then be determined from the y-intercept. Note that C_D as defined here is not a general parameter, but will vary between instruments due to differences in height above the bed and possibly local bottom roughness. Results for all 6 ADVs are presented in Figure 6.4, with the inferred C_D indicated in the legend.

The values for C_D are roughly consistent between instruments, with a mean of about 1.5×10^{-3}. Further comparison between instruments was not pursued as the measurements were all from different heights. The shape of the scatter is roughly consistent between instruments, with the exception of the *M03* ADV which has a "tail" of high ϵ at low U_f. The origin of the tail is unclear, as it exhibited no obvious relationship with any known physical variables. One possibility may be that the instrument contained a higher than normal spectral noise floor (minimum ϵ determined using the spectral method is $\sim 10^{-7}\,\mathrm{W/kg}$ as opposed to the other ADVs which were $\sim 10^{-9}\,\mathrm{W/kg}$). This may have been a result of either a configuration error or a malfunction. Generally the dissipation levels were at least an order of magnitude higher than $10^{-7}\,\mathrm{W/kg}$ across all moorings, so that the noise floor was not deemed to be a significant issue.

6.3.2 Shear Production of Turbulence

Shear production of turbulence (P) was estimated from the ADV data at both *M05* and *M08*, using the velocity measured from the two instruments (at different heights) to determine the vertical shear. The horizontal separation between the sensors was assumed to have no effect on the measurement of mean shear. The Reynolds stresses $\overline{u'w'}$ and $\overline{v'w'}$ were determined by first high-pass filtering the ADV velocities with a third order Butterworth filter with a cutoff period of 5 s, and then averaging the product of the velocities in one minute bins. Reynolds stress measured using both ADVs was then averaged and multiplied with the mean shear.

Scatterplots of P and ϵ for the two moorings are presented in Figure 6.5, and show

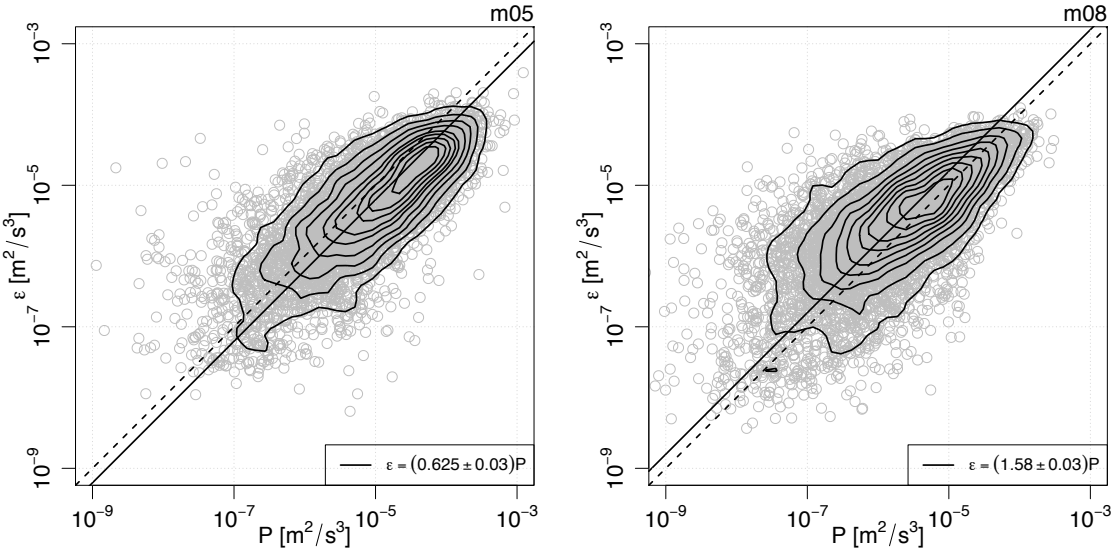

Figure 6.5: Dissipation and production at *M05* and *M08*, plotted with a logarithmic scale. The contours indicate data density as in Figure 6.3. The dashed line is the 1:1 relationship, and the solid line is a least squares fit with slope of 1. The resulting relationship between ϵ and P is indicated in the legend.

that the two quantities are generally within an order of magnitude of each other. Averaged over the entire deployment, the relationship between the two quantities appears to be different between the two locations, with *M05* showing a slight excess of P over ϵ, and the opposite at *M08* (see results of a linear fit in the legends). Visual inspection of the scatterplot for *M08*, however, suggests that the relationship between P and ϵ is not 1:1, and that P exceeds ϵ when P is large.

There are several possibilities for the differences between P and ϵ indicated by the ADV data. The first is that the TKE balance follows Equation 6.7, and includes a contribution from buoyancy flux, J_b. While J_b can be of either sign, in stratified turbulence it will generally be negative, resulting in a loss of energy from the turbulence to the potential energy field through mixing. The result is that on average production, as the main source of TKE from the mean velocity field, should exceed the dissipation.

The second possibility is that the estimates of P may be too large, due to tilts of the velocimeter not being properly corrected for. On a flat bottom, the velocity signal from a tilted ADV can be corrected using the measured pitch and roll angles so that the vertical axis is aligned perpendicular to geopotential surfaces. In this

coordinate system, the mean vertical velocity (over a time scale that is long compared to events such as upwelling or internal waves) will be zero. In the case of a sloped or irregular bottom, the correct "vertical" coordinate is less clear. One might expect that the average velocity perpendicular to the sloped bottom should be zero, however the scale over which to determine this angle is unclear. Further, local irregularities in bottom roughness will also have an effect. The result is that the vertical velocity fluctuations w' will be contaminated by the horizontal fluctuations u', potentially increasing their magnitude but also creating an artificial correlation that will be nonzero under the Reynolds averaging. A rough estimate with a slope of 2° and a purely horizontal flow of 0.5 m/s gives an apparent vertical velocity of ≈ 0.02 m/s, and a Reynolds stress proportional to $u^2 \sin(2s)$, where s is the slope angle in radians.

Possibly the error in P is a result of both buoyancy flux and vertical alignment uncertainty, but it is not possible to separate the two influences, as data were not collected that permit an accurate calculation of J_b. Further discussion on the issue of calculating buoyancy fluxes can be found in Section 7.4.2.

6.3.3 July 1st Shoaling Event

Turbulence associated with a shoaling internal wave event was examined using mooring data, ship transects, and shore-based photogrammetry, for a focus period on July 1, between the hours of 15:00 and 19:00 UTC. This time corresponded to the rising tide, during which waves are most likely to be seen (Figure 3.10). An example image from the shore-based photogrammetry is presented in Figure 6.6, showing the surface signatures of at least 6 waves propagating toward the shore. A second focus time during the opposite phase of the tide, approximately 6 hours earlier, was chosen to represent low internal wave conditions for comparison with the dissipation measurements. The focus periods had weak winds ($<$ 2-3 m s^{-1}) and minimal surface waves ($<$ 10 cm).

Figure 6.7 shows several transects of the water column structure obtained with the towed echosounder near the x-axis line. The vertical profile of σ_θ inferred from the TDRs using the TS relationship at *M08* suggests that the high backscatter layer at about 25 m depth corresponds to the pycnocline, and is therefore the location of maximum vertical internal wave displacement. Visible in Figure 6.7 a) are: a wave undergoing transition from a wave of depression to a wave of elevation ($x \approx -1250$ m),

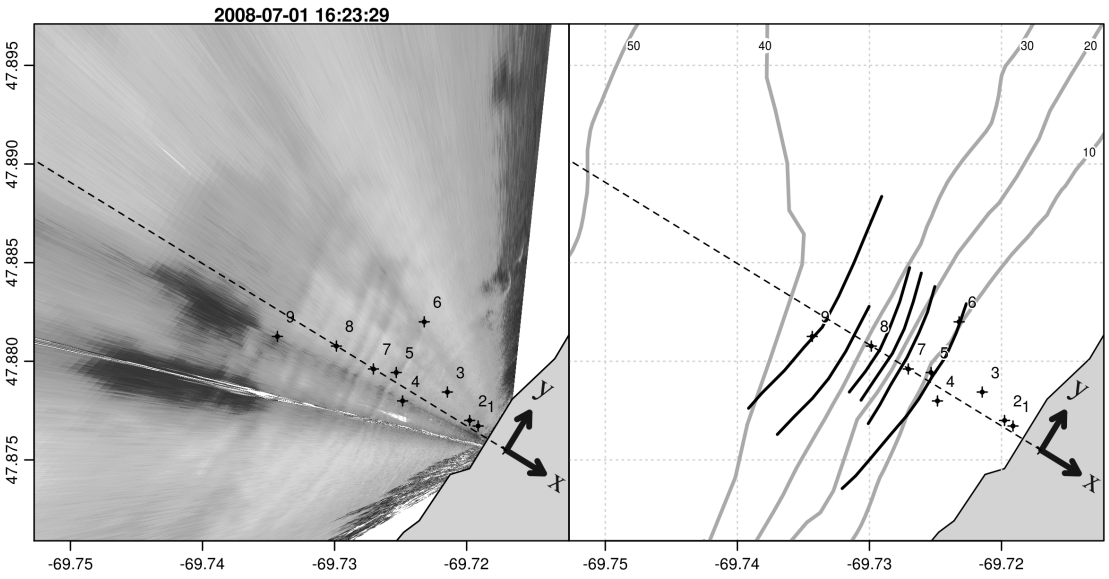

Figure 6.6: Example georectified image, on July 1 at 16:23:29 UTC. The left panel shows the rectified image plotted with the coastline, coordinate system, and the moorings. Camera elevation is 35 m. Bands of alternating brightness are surface signatures of internal waves, propagating toward the coastline. The right panel shows the same view, but with the wave front positions plotted over the bathymetry to show orthogonality of the wave propagation direction to the coast. The axes are drawn to indicate a 250 m distance.

a wave of elevation ($x \approx -1100$ m), and a series of upslope propagating wave or bolus-like features (between $x \approx -1000$ and $x \approx -800$ m, and perhaps even shallower). The locations of the moorings shows that our experimental design is well positioned to sample the waves at each phase of their transformation over the shoaling bottom (Figure 2.2).

The echosounder panels in Figure 6.7 (a, c, e, and g) show the evolution of the shoaling waves over a time period that spans 16:30 to 16:55 UTC. The vertical velocity measured by the ADCP at *M07* is plotted to the right of each transect, for a 10 minute interval centred on the time the ship passed the mooring. Together, the two data sets highlight the nonlinear evolution of the shoaling waves. In panels a/b and c/d, *M07* is within the pycnocline region, and the wave signals observed by the profiler are strongly nonlinear (note the large vertical velocities, with the maximum speeds close to the bottom). In the transects plotted in e/f and g/h, *M07* is below the main pycnocline (as indicated by the backscatter), and the maximum vertical velocity signals are correspondingly higher in the water column and less

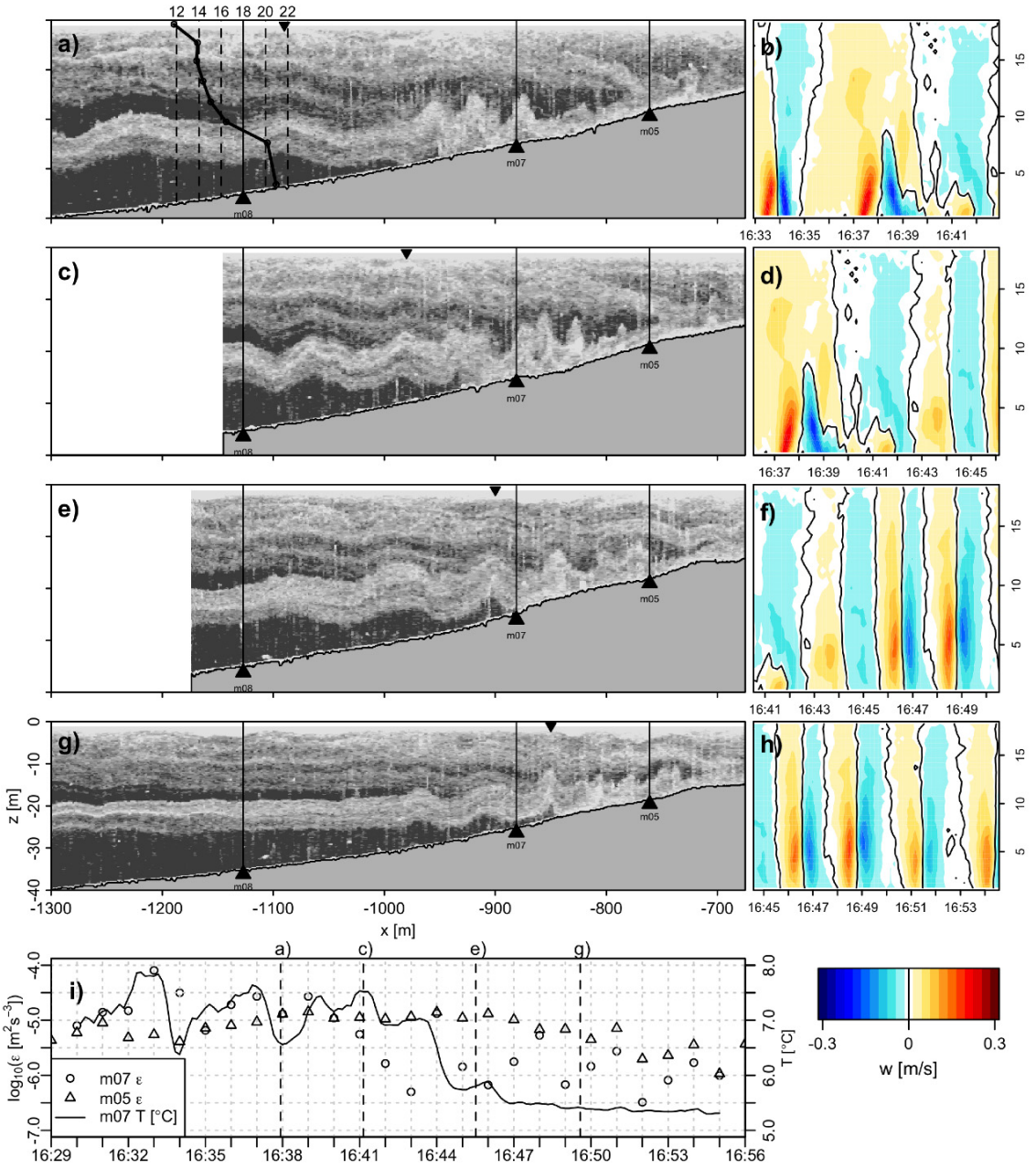

Figure 6.7: Towed echosounder transects along the mooring line, highlighting the evolution of shoaling internal waves (a, c, e, g). The distance along the x-axis is indicated along the bottom. The mooring locations are marked by the dark triangles and vertical lines, and the inverted triangles at the top of each transect identify the location of a wave feature discussed in text. The vertical σ_θ profile at *M08* is an instantaneous density profile calculated using the TDRs along with the TS relationship. Values are indicated by the dashed lines, in 2 kg/m^3 increments from 12 to 22 kg/m^3. Panels b), d), f), and h) show the vertical velocity measured by the *M07* ADCP for a 10 minute period centred on the time the ship passed the mooring. Panel i) shows a time series of the dissipation measured at *M05* and *M07*, along with the temperature measured by the *M07* ADCP.

intense. Tracking individual features in the echosounder transects from offshore to onshore highlights the cross-estuary transformation of a single wave. Note the feature identified by the inverted triangle, which transitions from a broad wave of elevation in Figure 6.7a) to a narrow, highly nonlinear bolus by g).

Figure 6.7 i) shows the dissipation measured by the ADVs at *M05* and *M07*. Along with the change in the wave properties observed at *M07* during shoaling, there is a corresponding drop in the level of inferred dissipation. The drop in dissipation can also be seen to coincide with a decrease in bottom temperature. This observation supports the view that the change in depth of the pycnocline has an effect on the wave properties observed above the mooring.

The three velocity components, vertical shear, acoustic backscatter, and temperature are presented for the *M07* ADP in Figure 6.8, showing a train of 5-6 waves of elevation (or boluses) passing the mooring over a 30 minute period. The waves show strong onshore and vertical velocities (~ 0.5 and $0.25\,\mathrm{m/s}$ respectively), and the water column vertical shear is dominated by the wave contribution. Acoustic backscatter suggests significant resuspension of sediments consistent with other studies (*Quaresma et al.*, 2007), though this was not verified here with *in situ* data. The temperature record shows pulses of cold, dense water, indicating possible horizontal transport of fluid within "trapped cores" (*Lamb*, 2003) (see e.g. Section 4.4, Figure 4.7).

To highlight the time dependence of features observed in the georectified images acquired on July 1, the pixels located along the x-axis were extracted to create a distance-versus-time representation, presented in Figure 6.10. The image uses a nonlinear grayscale mapping to reveal features, and each column in the image was adjusted to have equal average brightness, removing the effects of varying background lighting conditions.

Plotted in this way, propagating features can be identified as sloped bands, with their shoreward component of propagation speed indicated by the slope. Using the mean density profile, vertical internal wave modes were calculated following Section 3.5.3. The solid black line beginning around 15:00 UTC indicates the path that would be taken by a mode-1 internal wave for the stratification shown in Figure 3.5, using the water depths of the field site approximated with a quadratic distance-depth

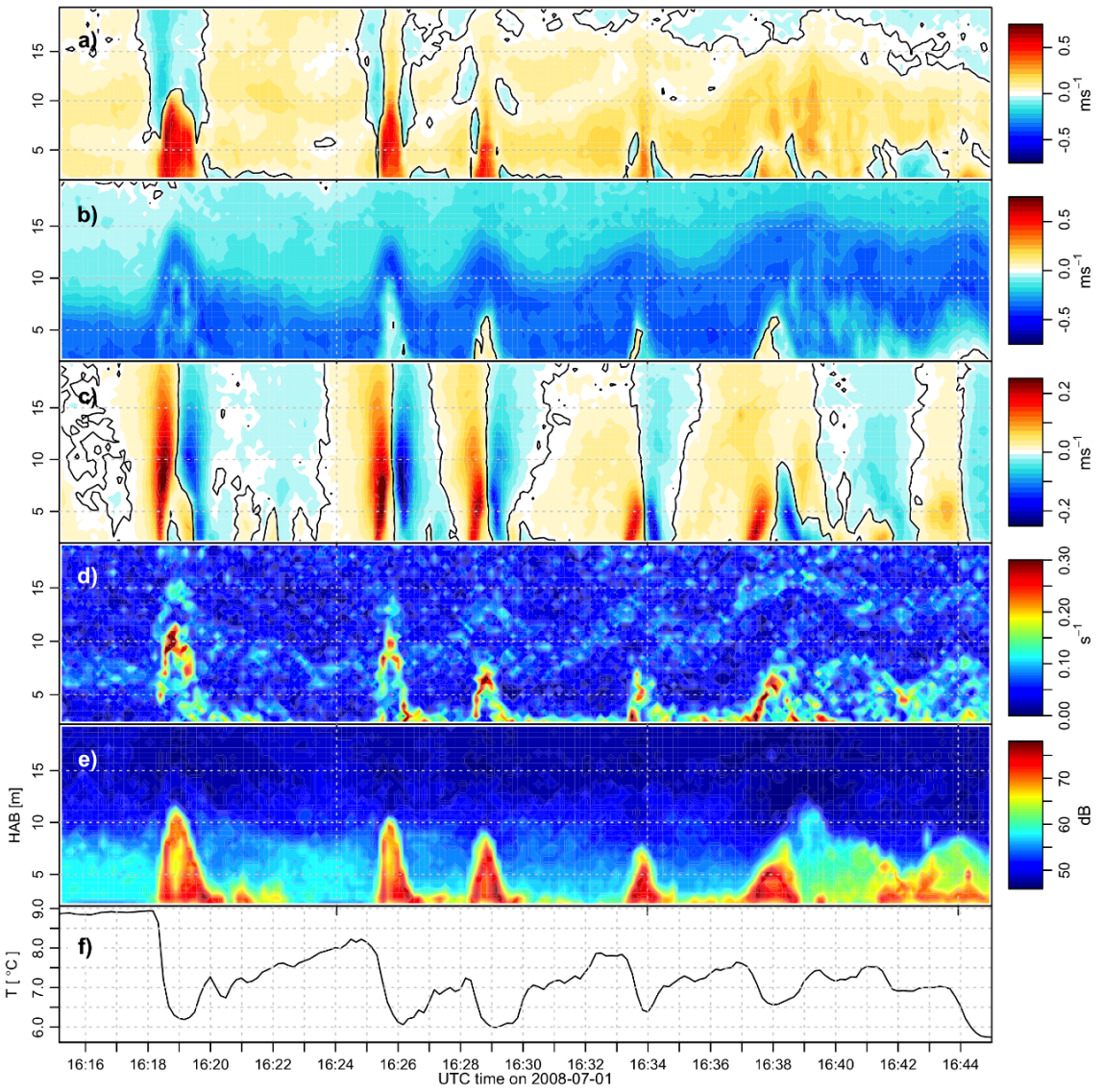

Figure 6.8: A 30 minute segment of a wave shoaling event on July 1 as measured by the *M07* ADP, showing a) onshore velocity, b) alongshore velocity, c) vertical velocity, d) magnitude of the vertical shear of the horizontal current, e) acoustic backscatter, and f) bottom temperature. The black line in a), b), and c) indicates the zero contour.

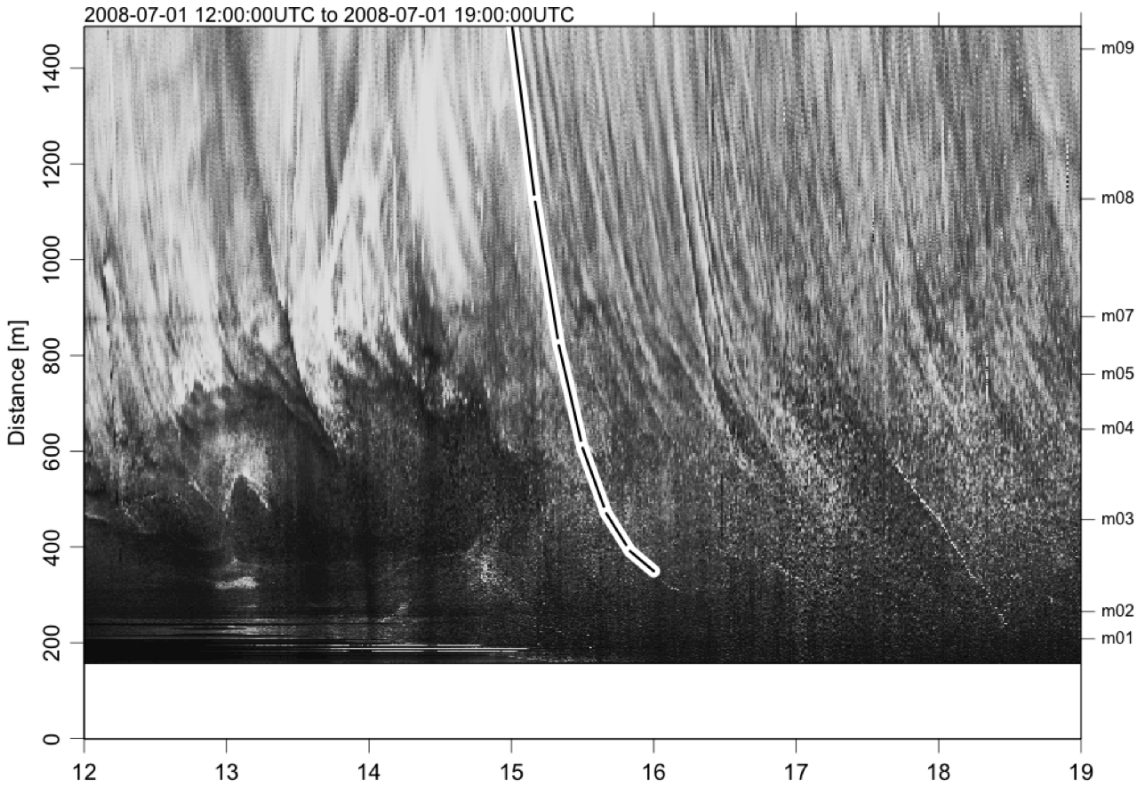

Figure 6.9: Surface brightness observed by the island-based camera, restricted to the line of pixels oriented over the mean mooring line (See Figure 2.1 for camera location and the viewing direction). A nonlinear color mapping has been applied to reveal features. Tics at the right of the image indicate the distances of moorings *M01* through *M09*; moorings *M10* and *M11* were beyond the view of the camera. Each column in the image has been adjusted to have equal average brightness. The sloping bands are possible surface signatures of internal waves propagating towards the shore. The line beginning at 15:00 UTC indicates the speed of a mode-1 internal wave for the stratification shown in Figure 3.5.

model.

Plotted overtop of the image at the positions of the moorings, are the depth-averaged vertical velocities and the bottom temperature, as measured by the ADPs. Matches between the surface features and the velocity and temperature traces, combined with the reasonably good agreement between the observed and modelled phase speeds, especially in deeper water, confirms that the features correspond to passing internal waves.

The correspondence of the observed surface signatures with internal wave signals from Figure 6.10 facilitates the extraction of the wave propagation direction from

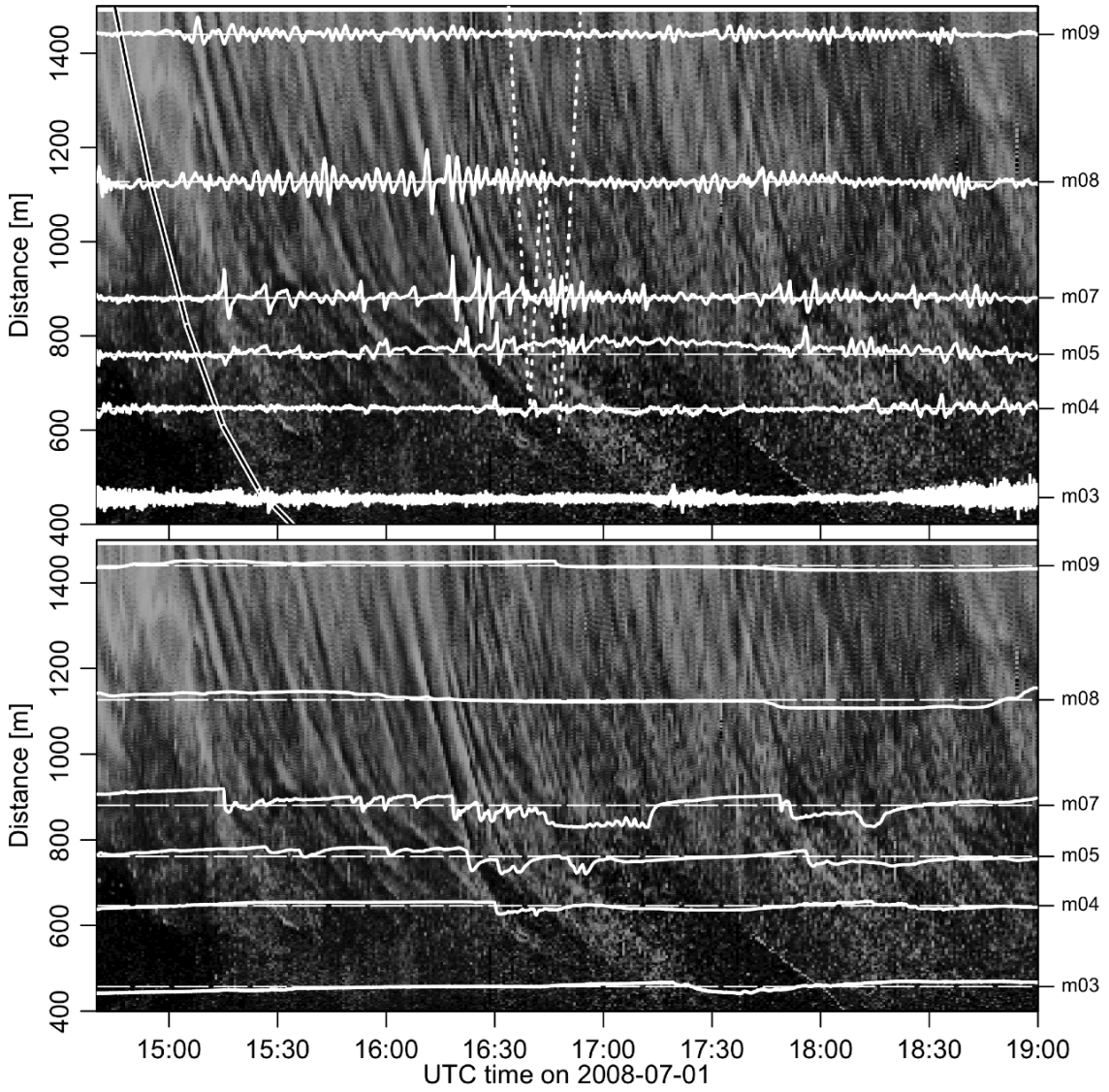

Figure 6.10: Surface brightness observed by the island-based camera, as in Figure 6.9, but for the focus period. Plotted overtop of the image are the depth-averaged vertical velocities (top), and the near-bottom temperature as measured by the ADPs (bottom). Both w and T show strong correlations with the propagating surface features. Note also the change in amplitude as the waves propagate into increasingly shallower water, indicating a loss of energy as they shoal. The vertical scale in both panels is arbitrary, but consistent between moorings. The solid black line is a model based on the mode-1 internal wave phase speed as a function of depth, and the dashed white lines indicate the locations of the echosounder transects in Figure 6.7.

the time series of georectified images (Figure 6.6). Determining wave direction in this manner eliminates the need for more complicated techniques using the moored ADPs, as was done in Chapter 5 (see also *Scotti et al.*, 2005; *Mirshak and Kelley*,

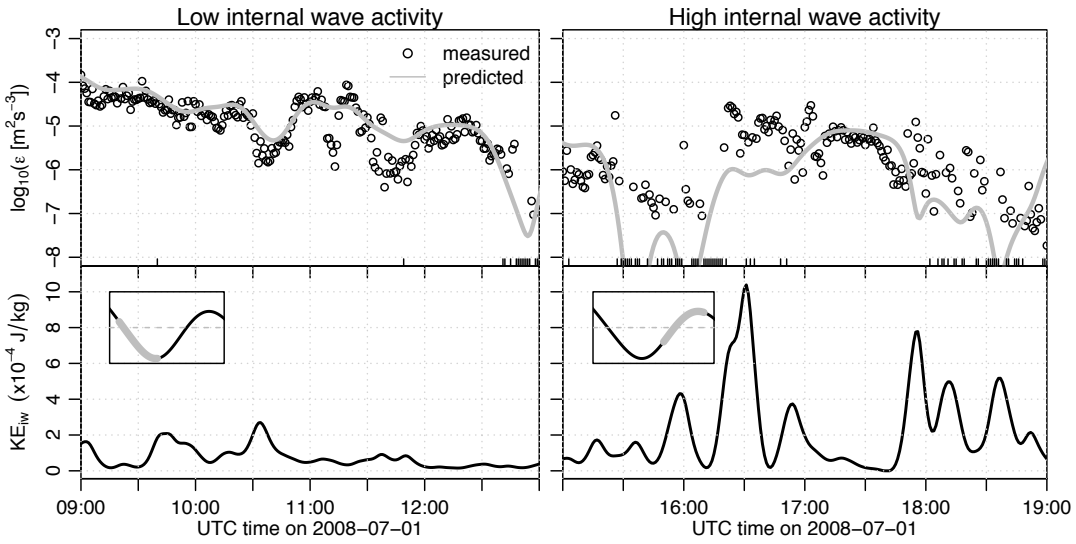

Figure 6.11: Dissipation rates inferred by the Nortek Vector at *M05* (circles) and predictions from the tidal dissipation model (gray line) for the two focus periods. Bottom panels show internal-wave activity over the same times, highlighting the periods of low (left) and high (right) internal-wave energy. The phase of the tide is plotted in the inset. The ticks along the bottom of the upper panels indicate times where dissipation values are missing due to the quality control tests.

2009). The alignment of the observed wave crests with the bathymetry, and the extent of the crest along the y-axis ($> 1\,\mathrm{km}$) supports the treatment of the waves and the shoaling process as two-dimensional (*Bourgault et al.*, 2005, 2007).

To separate the influence of the tides and internal waves on the dissipation rate, the tidal shear scaling presented in Section 6.3.1 was used. Time series of ϵ measured at *M05* (from the Nortek Vector) are shown in Figure 6.11, for the two focus periods. In the upper panels, the dissipation predicted by the tidal shear scaling is indicated by the gray line. The bottom panels show the time series of internal-wave energy proxy, following Section 3.5.2. The ϵ results on the left hand side, during the period of low internal-wave activity, show good agreement with the tidal dissipation model (rms difference 0.35). During the period of high internal-wave activity (on the right), the measured dissipation is at times several orders of magnitude greater than that predicted by the model (rms difference 1.03). The highest dissipation rates measured by the ADV during the wave passage are similar in magnitude to those observed during the maximum falling tide ($\epsilon = 5 \times 10^{-5}\,\mathrm{m^2\,s^{-3}}$).

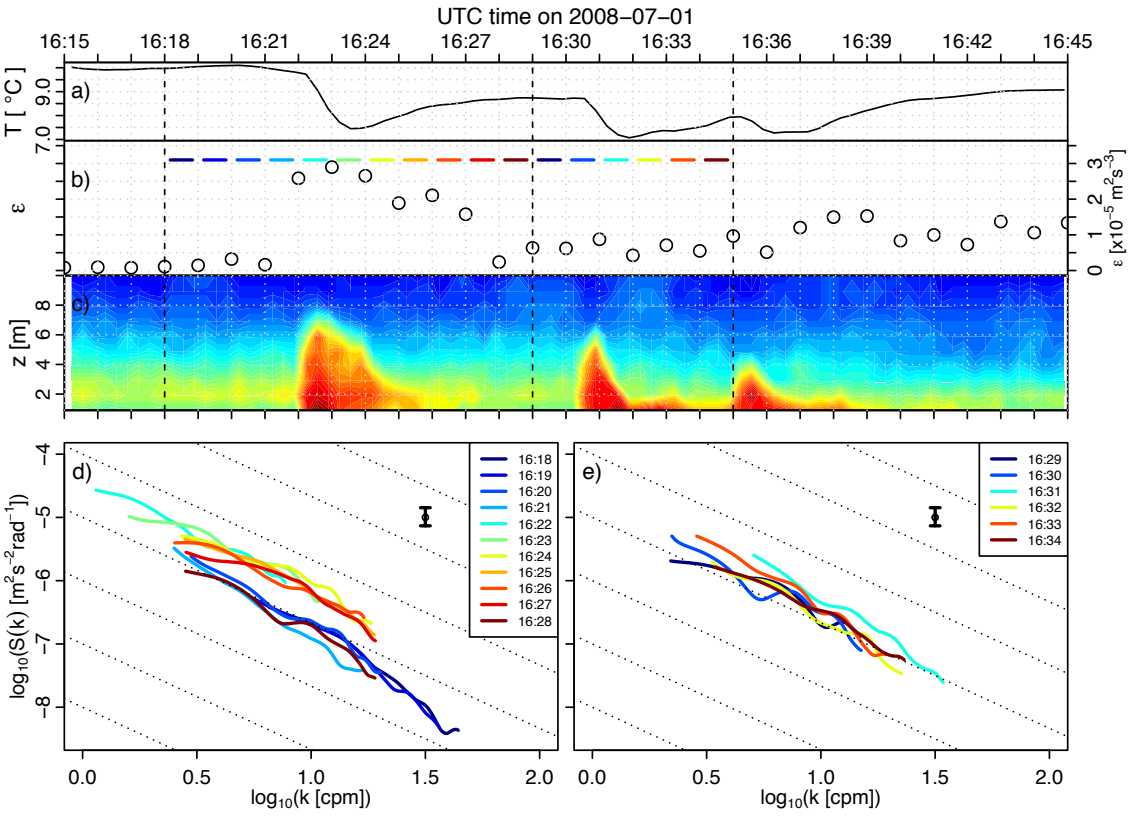

Figure 6.12: Three waves of elevation observed at *M05*, with a) temperature from the ADP, b) ϵ inferred from the Nortek Vector in 1 minute segments, c) ADP backscatter, d) spectral evolution for the period from 16:18 to 16:29, and e) spectral evolution for the period from 16:29 to 16:35. The colored segments in b indicate the times for the individual spectra in d and e, between the dashed vertical lines. The frequency spectra have been smoothed with a modified Daniell kernel with bandwidth 0.18 Hz and 95% confidence intervals indicated by the vertical bar, and the dotted lines indicate a slope of $-5/3$.

6.3.4 Sources of Turbulence

The dissipation measurements indicate a relationship between wave passage and elevated turbulence. This issue will be explored further in Chapter 7 using the entire dataset, but for the purposes of this section (to investigate the sources of the turbulence observed in the waves) the focus will remain on the July 1st event.

One explanation for the elevated turbulence may relate to advection, with waves heaving a near-bottom turbulent boundary layer into the sensing region, or with turbulence being carried laterally in trapped cores. Another explanation may relate to local production of turbulence, with waves producing turbulence through shear

instabilities or bottom boundary layer processes. These two mechanisms will be taken in turn, beginning with advection.

While observing similar waves with a vertical microstructure profiler, *Bourgault et al.* (2008) were unable to determine if observed values of high dissipation were inherent to the waves or resulted from a heaved bottom boundary layer. They speculated that the boluses may act to inhibit near-bottom turbulence, by increasing water column stability as they transport dense water up the slope. Their profiles did not extend all the way to the bottom, however, and this could have led to underestimation of the depth averaged water column dissipation by orders of magnitude. In the present case, examination of the near-bottom temperature record (Figures 6.8f and 6.12a) suggests that the source of the turbulence is not from a heaved bottom boundary layer, because the variations in temperature associated with the waves were too large to result from heaving, given the stratification. The approximately 3° C change observed in Figure 6.12 translates to a density change of $4.3\,\mathrm{kg\,m^{-3}}$ which, from the vertical profile in Figure 6.7, corresponds to a 7 m vertical displacement, much larger than the height of the sensor above the bottom.

Horizontal advection was advanced as a mechanism by *Moum et al.* (2007b) in their study of shoaling waves on the Oregon shelf. Noting that the high dissipation associated with passing waves decayed in times much shorter than the buoyancy timescale, they concluded that the turbulence measured within the waves was transported along with them, rather than being left behind to decay. Dissipation time series for the leading wave presented in Figure 6.12 show a rapid increase in ϵ, followed by a slower decay, with a timescale of $\sim 5-6$ minutes. This is longer than the buoyancy period of about $2\pi/N \approx 40-100\,\mathrm{s}$ (using either the ΔT from above or the mean pycnocline N_p of $0.06\,\mathrm{s^{-1}}$). Contrary to *Moum et al.* (2007b), this suggests that the observed waves may leak turbulent fluid behind them. A possible explanation for the discrepancy with *Moum et al.* (2007b) may be that the waves were observed during a different stage of the shoaling process.

The alternative limiting case is that turbulence is generated or dissipated entirely locally. It is possible to estimate the occurrence of turbulence generated by water column shear instabilities associated with the waves, using the density difference given above and the instantaneous values of vertical shear. From Figure 6.8d, instantaneous

values of shear near the upper front face of the waves can be as high as $0.3\,\mathrm{s}^{-1}$, over an interface about 2 m thick. Estimating $N^2 = -g/\rho_0(\partial\rho/\partial z) = 0.0206\,\mathrm{s}^{-1}$ from the temperature difference leads to an estimate of the Richardson number of

$$Ri = \frac{N^2}{\mathcal{S}^2} \simeq \frac{0.0206}{0.3^2} = 0.23,$$

which is close to the critical value of 0.25. Given the uncertainties in the estimate (using $\Delta\rho = 4.3 \pm 0.3\,\mathrm{kg\,m}^{-3}$, $\Delta z = 2.0 \pm 0.5\,\mathrm{m}$, and $S = 0.3 \pm 0.05\,\mathrm{s}^{-1}$ gives $Ri = 0.23 \pm 0.15$), this does not necessarily imply the onset of instability, but suggests that it may occur. This is consistent with the *Bourgault et al.* (2008) observations of high values of ϵ at the leading face of some of the largest waves.

Examination of the shape of successive velocity spectra provides an indication of whether the observed turbulence is locally produced (Figure 6.12d and e). Unlike the raw periodogram used to fit the functional form of the spectrum for determination of ϵ, here the frequency spectra were smoothed using a modified Daniell kernel (with bandwidth 0.18 Hz, yielding a nominal wavenumber bandwidth of 0.4 cpm). Prior to wave arrival, the overall log spectral slope is steeper than $-5/3$, indicating an excess of production versus dissipation, with more energy input to the lower wavenumbers. Once the wave arrives at the ADV (16:22 UTC), the spectrum level increases, and the shape approaches the $-5/3$ equilibrium form. During the decay, from ∼16:24 to 16:28 UTC, the spectral level at lower wavenumbers decreases relative to the higher wavenumbers, indicating dissipation exceeding production. In this sense, the waves represent a short-lived source of turbulent shear production, with local growth and decay of ϵ as a result. A similar examination of the spectra during the following wave (Figure 6.12e) is not as conclusive, possibly due to the presence of turbulence left behind by the first wave.

6.4 Conclusions

In this chapter, the turbulence dissipation rate, ϵ, was calculated from measurements made by ADV instruments. Quality control tests indicated that frame interference was an issue, and affected data were discarded. Overall, there is a slight excess of shear production of turbulence, which may be due to the presence of buoyancy fluxes,

or errors in the measurement of P due to sensor vertical alignment uncertainty.

The effects of internal waves were studied by contrasting a particular time of high internal-wave activity with a time of low internal-wave activity. It was found that ϵ is consistent with the predictions of a simple model of turbulence production by tidal shear only when internal waves are absent. Maximum values of ϵ in low-flow, high internal wave periods were as large as the tidal shear values observed during a strong ebb tide.

Near-bottom temperature signals indicate that the observed turbulence is unlikely to be caused by a heaved bottom boundary layer. Spectral shapes observed over the leading wave in a group indicate an initial excess of production versus dissipation as the wave arrives, followed by a period of decay characterized by excess dissipation. The time scale of the decay and the presence of turbulence after the wave passage both indicate that the waves may be leaving turbulent fluid behind them, at least at the level of the sensor.

Chapter 7

An Energy Budget for Internal Waves at the SLEIWEX Site

In Chapter 5, measurements of a number of discrete wave events provide a detailed picture of the properties of the incoming internal wave energy. In Chapter 6, it was demonstrated that the turbulence levels during a wave shoaling event were elevated above the background level expected from a purely tidal shear process. The goal of this chapter is to combine the results of these two previous chapters, to develop an energy budget for internal wave-generated turbulence at the SLEIWEX site, including a discussion of the energy flow to vertical mixing and buoyancy flux.

7.1 Turbulence and Internal Waves

In Chapter 3, a proxy for the presence of internal waves was developed, utilizing depth-averaged vertical velocities to estimate the kinetic energy density (per unit mass) due to waves (Equation 3.8). In this chapter, a slightly modified proxy will be used, based on all three velocity components,

$$KE_w = \frac{1}{2}\langle u_{iw}^2 + v_{iw}^2 + w_{iw}^2 \rangle_{lp}, \tag{7.1}$$

where the bandpass and lowpass filters are the same as in Section 3.5.2. The reason for using this modified proxy is to obtain a more realistic estimate of the kinetic energy (per unit mass), to compare with the discrete wave energy measurements.

Comparing this proxy with the measured dissipation rates reveals a relationship

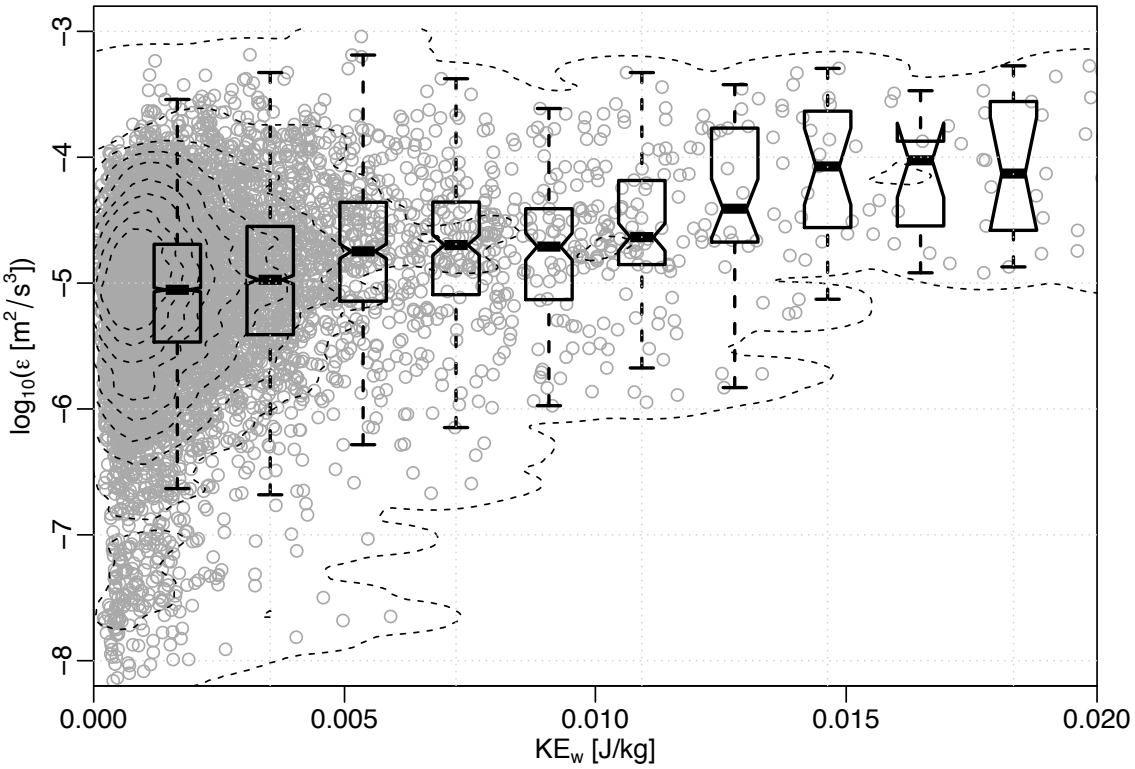

Figure 7.1: Dissipation rate and internal wave proxy measured at *M07*. Individual points are indicated by the grey circles, and the dashed lines indicate data density, decreasing from 100% to 10%. Boxplots summarize the statistics within KE_w intervals of 0.002, with the centre line for the median value, and the notches for an estimate of the 95% confidence interval on the median. Non-overlapping median ϵ values for increasing KE_w indicate a significant difference.

where high ϵ occurs when KE_w is high. This relationship is demonstrated in Figure 7.1 for *M07*. As indicated by the dotted contours, much of the data correspond to low wave proxy values ($KE_w < 0.05\,\mathrm{J/kg}$), highlighting the intermittent and episodic nature of the waves. When larger values of KE_w do occur, they correspond to relatively high values of dissipation rate ($10^{-4}\,\mathrm{W/kg}$). The boxplots in the diagram, derived from binned statistics, indicate a significant increase at high KE_w. By $KE_w \simeq 0.01$ (approximately half the maximum observed value of the proxy), the median ϵ is about a factor of 5 or 6 higher than when the proxy is near zero.

7.2 Wave Proxy and Energy Flux

Having measured the total integrated pseudoenergy $\langle \mathcal{E} \rangle$ (see Equation 5.11) of a number of discrete internal wave events in Chapter 5, it is possible to compare the measurements with the wave proxy. The pseudoenergy, measured for each observed wave, can be converted into a water column-averaged energy density (per unit volume), by dividing by the depth H and by the length of the wave, L, the latter corresponding to the length over which the entire wave velocity and density field is integrated to get the total energy from E_k and E_a (Section 5.3.2).

A comparison between the wave proxy with the measured kinetic and pseudoenergy densities (in $\mathrm{J/m^3}$) is presented in Figure 7.2. As indicated by the best-fit lines a significant relationship exists ($R^2 = 0.8223$, $p < 10^{-16}$). In each panel, the dashed line indicates either a 1:1 or a 1:2 (based on an equipartition of energy) relationship with KE and $\mathcal{E}$, respectively. The grey shaded regions indicate the 95% confidence limits of the predictions of the regression. The relationship between the wave proxy and the pseudoenergy density is

$$\mathcal{E}_w = (1.86 \pm 0.21)\rho_0 KE_w \tag{7.2}$$

The existence of a relationship between the wave kinetic energy proxy and the total energy of individual waves permits an estimate of wave energy as a function of time for each ADP. Similarly, assuming that the waves are propagating toward the shoreline (an assumption discussed further in Section 7.3), a time series of pseudoenergy flux can be estimated using the first mode internal wave speed. In the following section, the effect on dissipation rates near the shoreline as a result of a time-varying internal wave energy flux will be examined, employing the empirical relationship between $\mathcal{E}$ and KE_w.

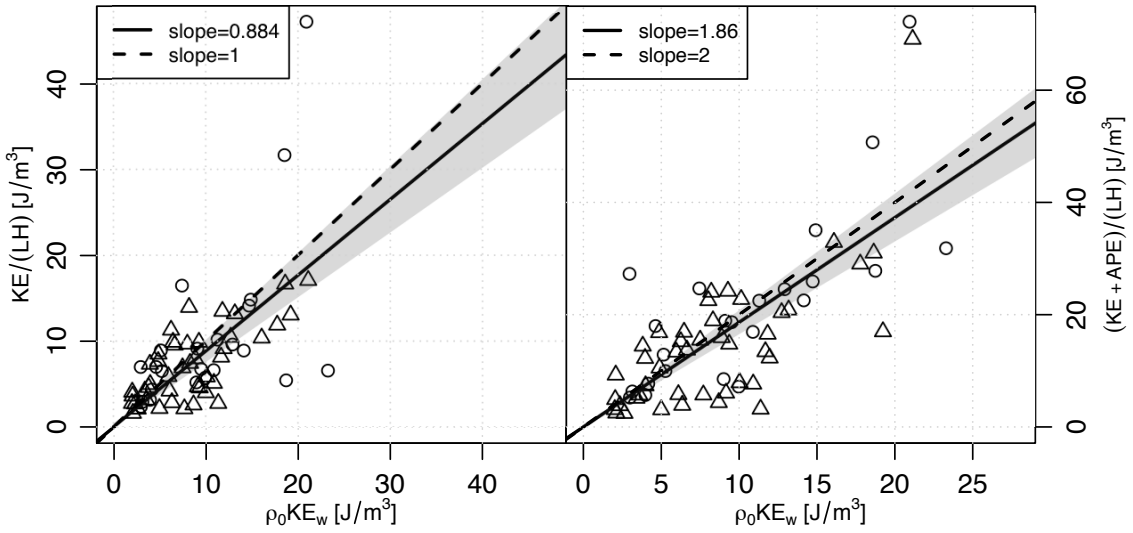

Figure 7.2: Comparison of internal wave proxy and observed wave energy density. Left: observed KE density vs the internal wave proxy. Observed densities have been divided by the water column depth and the length of the wave to convert KE to KE density (per unit volume), while KE_w is multiplied by ρ_0. The dashed line indicates a 1:1 relationship, and the solid line is the result of a linear fit through the origin. The grey shaded region is the 95% confidence interval. Circles indicate waves of depression and triangles waves of elevation. Right: Same as on left, but with the pseudoenergy $\mathcal{E}$ on the y-axis. Dashed line now indicates a slope of 2, expected if there is an equipartition of KE and APE.

7.3 A Simple Turbulence Model for Shoaling Internal Waves

Following *Moum et al.* (2007b), the equation for the pseudoenergy (i.e. Equation 5.7) can be written as

$$\frac{\partial \mathcal{E}}{\partial t} + \frac{\partial f_E}{\partial x} + \text{vertical redistribution} = -\rho_0 \epsilon + \text{other sources/sinks}. \tag{7.3}$$

For a horizontally propagating internal wave, the terms involving vertical redistribution disappear in a vertical integral, and thus do not contribute to lateral energy transport when averaged over the wave. Assuming that no other sources or sinks of energy exist, the total rate of change of energy of a wave must be balanced by dissipation, i.e.

$$\frac{D\mathcal{E}}{Dt} = -\rho_0 \epsilon. \tag{7.4}$$

Moum et al. (2007a) and *Shroyer et al.* (2010a) compared the energy loss of nonlinear internal waves over long distances by tracking coherent features and making direct measurements of $\mathcal{E}$ as a function of time, coincident with microstructure profiles of ϵ. *Moum et al.* (2007a) found good agreement between the two estimates of the rate of energy loss, when averaged over a propagation distance of hundreds of wavelengths. *Shroyer et al.* (2010a) found similar agreement, while also observing periods of energy growth during the early stages of wave lifetime.

The approach must be modified for an Eulerian framework, such as in the present case, where wave energies are measured as time series at a number of discrete locations. While the spatial variation of pseudoenergy flux is relatively well resolved by the mooring array, measuring $\partial\mathcal{E}/\partial t$ is more challenging. Attempts to assess ϵ using Equation 7.4 between two moorings (i.e. *M09* and *M07*) were unsuccessful, owing to several factors. First, difficulties tracking individual waves between moorings precluded direct estimates of $\partial\mathcal{E}/\partial t$ for individual events. Second, reliable estimates of horizontal energy flux for individual events were only obtained at *M07* and *M09*, and not farther inshore. Finally, the only estimates of ϵ between *M07* and *M09*, provided by the velocimeters at *M08*, were located well below the nominal pycnocline where much of the wave-induced turbulence would be expected.

Another approach is to consider a control volume within which the incoming waves are destroyed, with their energy converted to turbulence and dissipated. A schematic of such a scenario is shown in Figure 7.3. An integral of Equation 7.4 states that the rate of incoming wave energy $c\mathcal{E}_w WH$ is balanced by the turbulent dissipation within the volume, $\rho_0 \epsilon_w V_m$, where W is the width (in the alongshore direction), H is the offshore water depth at the location of measurement, V_m is the volume over which the turbulence occurs, and ϵ_w is the dissipation rate associated with waves.

If the control volume is assumed to have a linearly shoaling bottom, as in Figure 7.3, and the mixing is distributed over the entire triangular box, a volume-averaged dissipation rate will be

$$\epsilon_w = \frac{2c\mathcal{E}_w H}{\rho_0 L},$$

where L is the distance between the measurement location and the shoreline. More likely, the volume over which turbulence is generated (V_m) is likely to be some fraction of the total volume, possibly concentrated near the bottom, and potentially

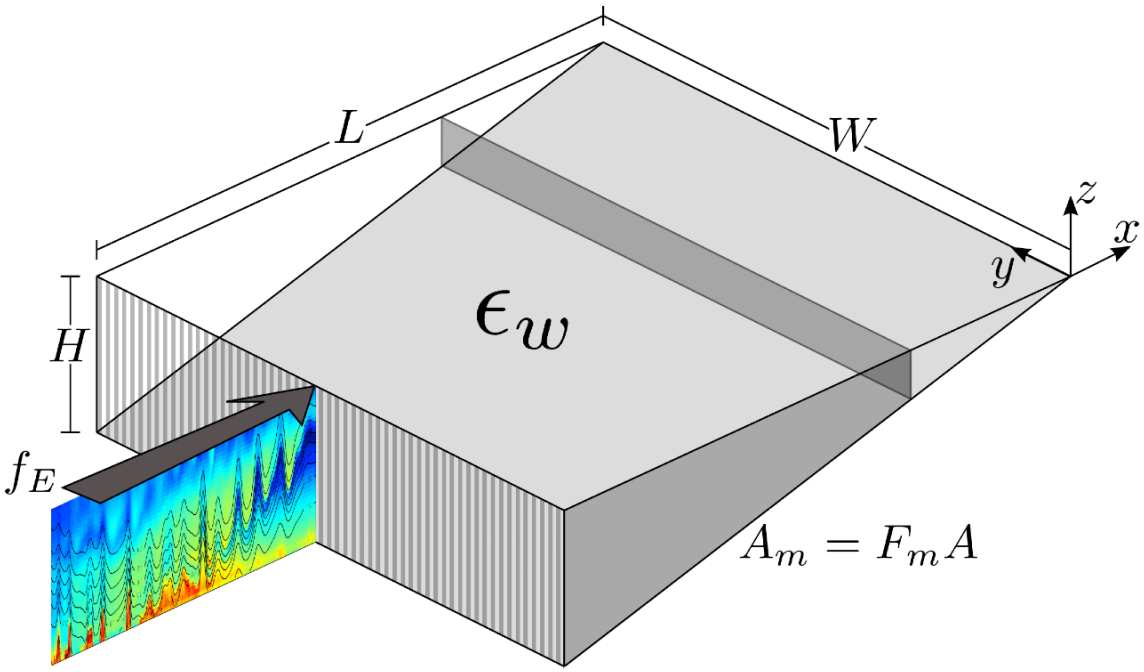

Figure 7.3: Definition sketch for internal wave turbulence model. The striped face is the location of incoming wave energy, and the checkered face is the cross-sectional corresponding to the mixing volume. See text for other details.

located within some distance of the intersection of the pycnocline and the bottom, yielding

$$\epsilon_w = \frac{c\mathcal{E}_w H}{\rho_0 F_m A}, \tag{7.5}$$

where the width W has been eliminated by assuming no lateral variation, F_m is the fraction of the total volume in which turbulence occurs, and A is the cross-sectional area associated with V.

The above estimate of wave-induced dissipation depends on complete destruction of the incoming wave energy. In other words, the reflectance of the shoaling bottom is assumed to be zero. Studies of internal wave reflectance (R) on slopes have shown that this is not always the case, and that the amount of energy reflected is a function of a ratio of the wave and topographic slopes. This is often expressed in terms of an internal Iribarren number, calculated as $\xi = s/(a/L_w)^{1/2}$, where s is the topographic slope, a is the amplitude of the wave, and L_w is the wave length scale. Using a numerical model, *Bourgault and Kelley* (2007) derived an empirical parameterization of the reflectance, which for typical values observed at the SLEIWEX site ($s = 0.02$, $a = 10\,\mathrm{m}$, and $L_w = 100\,\mathrm{m}$) suggests that $R < 0.1$, or that less than 10% of the energy

may be reflected back offshore. Due to the difficulties associated with measuring R in natural settings, whether or not the numerically-derived parameterization is realistic remains to be determined. In a recent study (*Bourgault et al.*, 2011), nonlinear wave reflectance from a steep slope was observed to be half of that predicted following *Bourgault and Kelley* (2007) (0.5 instead of 0.9). The assumption of 0 reflectance is therefore taken as reasonable here, given the uncertainties associated with other quantities, particularly the volume fraction.

A model for near-bottom turbulence at the SLEIWEX site, including contributions from tidal shear and internal waves, can now be constructed by combining Equation 6.20 with Equation 7.5 to give

$$\epsilon = \frac{{C_D}^{3/2} U_f^3}{\kappa z} + \frac{c \mathcal{E}_w H}{\rho_0 F_m A}. \tag{7.6}$$

In the following section, Equation 7.6 will be used to predict ϵ at the SLEIWEX field site.

7.4 Estimates of Turbulence and Mixing

Making use of Equations 7.2 and 7.5 to estimate the time-varying wave energy flux toward the shore and the resulting dissipation requires several assumptions.

First, the waves are assumed to propagate at a speed corresponding to the first baroclinic mode. The justification for using the first baroclinic mode speed was presented in Section 5.2.

Second, the waves are assumed to propagate perpendicular to the coast. On average the waves were observed to approach the shoreline perpendicularly. Of the 67 waves observed, only 7 of them had propagation direction $< -60^\circ$ or $> 0^\circ$ (where 0° is East, and the onshore direction is -31.5°). Further, if the width is taken as representative of the entire region of shoaling (perhaps 10-20 km at the SLEIWEX site), slight variations in propagation direction will average out, provided the waves are approximately two-dimensional and the time scale for calculating a mean ϵ is long enough. *Bourgault et al.* (2008) observed what appeared to be a pair of downslope propagating boluses, however the amplitude was small compared to the upslope propagating features. No downslope propagating waves have been detected in the

current data set.

Third, the wave-induced dissipation is assumed to be evenly distributed over the estimated mixing volume $V_m = F_m V$. Likely, the relevant volume will be a complex function of many parameters, possibly including: background stratification, incoming wave energy, fluid transport by the waves, and a nonlinearly sloping bottom. As such, the mixing volume represents a scale factor on ϵ_w, but should not significantly affect the overall pattern, which is controlled by the incoming wave energy.

Choosing F_m

The value of F_m was determined roughly by minimizing the sum of the squared error between the measured and the modelled dissipation (Equation 7.6). For *M05* and *M07* F_m was approximately 1, however, at *M03* it was much smaller, at approximately 0.05.

7.4.1 Turbulence at *M05*

The estimate of incoming internal wave energy flux at *M07* was used with Equation 7.5 and $L_m = x_1 - x_7$ (the distance between *M07* and *M01*) for the time period from June 25 23:00 to July 3 00:45 UTC. Using *M01* as the furthest extent of the mixing volume was justified by observations there of temperature signals believed to be caused by shoaling waves. An estimate of dissipation associated with tidal shear was also calculated for this time period using the near-bottom current speed, following Section 6.3.1.

The *M05* mooring contained two ADVs, each oriented differently with respect to the frame and the background flow (Figure 6.2). As a result, the Nortek unit was predominantly shaded during the rising phase of the tide, and the Sontek during the falling. Combining the measured ϵ from the two instruments, and averaging (in log-space) when they both contained reliable data reduced the fraction of missing values from about 38% (33% and 45% for the Nortek and Sontek units respectively) to about 5%.

The measured ϵ, along with the tidal and wave derived estimates, is presented in Figure 7.4, plotted against tidal phase and including all 15 of the cycles sampled. There is considerable variability between tidal cycles, with ϵ varying by as much as 2-3 orders of magnitude at the same phase of the tide. The overall pattern, however,

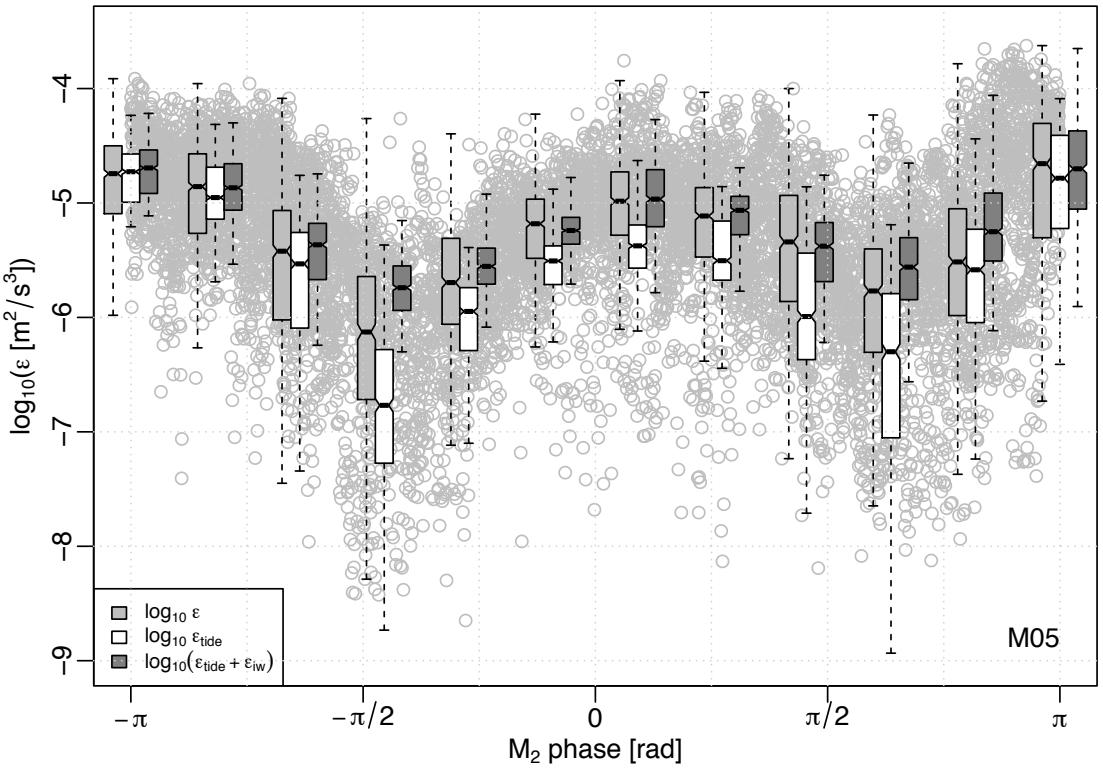

Figure 7.4: Observed and predicted dissipation at *M05*, as a function of tidal phase. The grey dots indicate individual observations. The boxplots summarize statistics; light grey corresponds to the observed dissipation rates, while white and dark grey correspond to the tidal and tidal plus internal wave models respectively.

is roughly consistent with a tidal shear model where larger currents (at phases of $\pm\pi$ and 0) result in higher dissipation. Plotted overtop are box plots summarizing the statistics of each of the time series of dissipation (measured, tidal model, and wave plus tidal model), for 12 intervals between $-\pi$ and π.

On average, the tidal shear model underestimates the observed dissipation (light grey boxes) during the rising phase of the tide, between $-\pi/2$ and $\pi/2$ (Figure 7.4). During the falling tide, however, there is good agreement between the two. The difference during the falling tide can be accounted for by adding the dissipation derived from Equation 7.5 to that predicted by tidal shear, indicated by the dark grey boxes in Figure 7.4. On average, during the rising tide, the tidal shear model underestimates the dissipation by a factor that varies between 2 and 5.

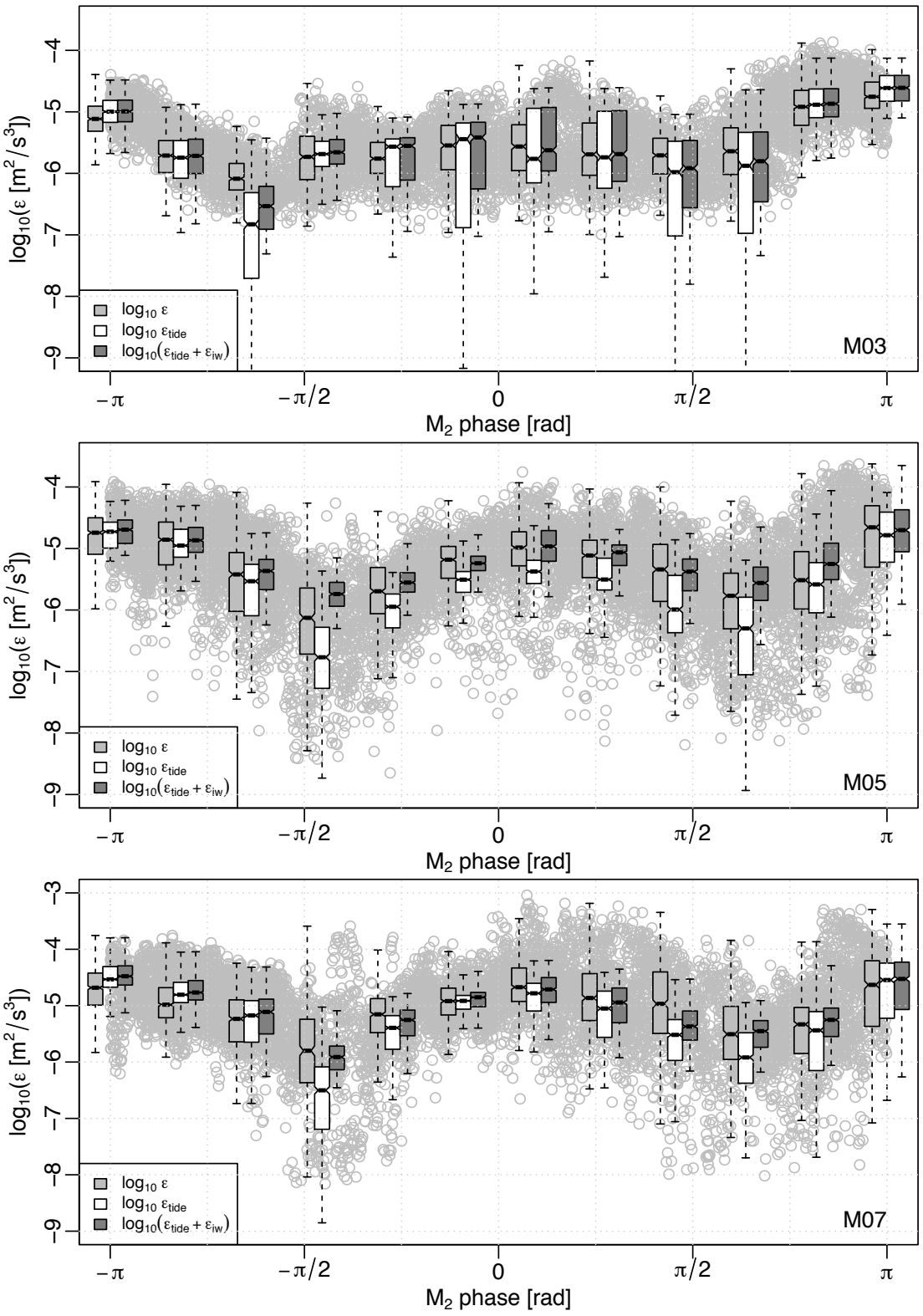

Figure 7.5: Observed and predicted dissipation at *M03*, *M05*, and *M07*, in a format the same as in Figure 7.4.

Comparison with Other ADVs

A similar analysis was applied to the ADVs at *M03* and *M07*, using internal wave energy calculated from the *M05* and *M09* ADPs, respectively. The results, presented in Figure 7.5, reveal details of the spatial pattern of wave-induced dissipation, again averaged across tidal phase.

At *M07* (lower panel), a phase dependent pattern similar to that observed at *M05* can be seen, however the mismatch between measured dissipation and the tidal model is not as large as at *M05* (middle panel). The dissipation predicted by the incoming wave energy from the *M09* ADP accounts for some of this difference, however even in the latter half of the rising tide (between 0 and $\pi/2$) the measured ϵ is typically larger than the full model would predict.

At *M03*, there is generally good agreement between measured ϵ and the tidal model. At this location it appears that the average effect of internal waves on dissipation is small (upper panel of Figure 7.5). There is some question as to whether the relationship between the wave proxy at *M05* and true wave energy flux is valid, as detailed measurements of the wave field were not made in this location. Further, being the ADV with the greatest horizontal distance from the mean intersection of the pycnocline with the bottom, it is expected that wave-induced dissipation will be apparent at *M03* only during shoaling events when the pycnocline is shallow.

The spatial variation in wave induced turbulence may be related to the location of the moorings relative to the pycnocline during each wave event. As indicated in Figure 2.2, *M05* is located at the depth of the nominal pycnocline, suggesting that during wave shoaling events it will be subject to the highest levels of turbulence resulting from wave breaking.

7.4.2 Implications for Vertical Mixing

From a phase averaged perspective, the effect of internal waves on turbulent dissipation during the rising tide at the SLEIWEX field site is significant. The estimate of ϵ_w represents an energy source for mixing that is not currently parameterized in coastal numerical models. Any physical effects associated with the increased mixing (such as buoyancy or nutrient fluxes) will not be resolved.

It is possible to estimate the vertical diffusivity (of density) K_V from ϵ using an

eddy diffusivity formulation

$$\overline{\rho' w'} = -K_V \frac{\partial \overline{\rho}}{\partial z}, \tag{7.7}$$

where K_V is often assumed to be of the form

$$K_V = \Gamma \epsilon N^{-2} \tag{7.8}$$

(*Osborn*, 1980). In Equation 7.8, Γ is a mixing efficiency, often expressed as

$$\Gamma = \frac{R_f}{1 - R_f}, \tag{7.9}$$

where the flux Richardson number is

$$R_f = \frac{1}{1 + \epsilon / J_b} \tag{7.10}$$

(see e.g. *Ivey and Imberger*, 1991). Γ represents a ratio of potential energy to kinetic energy dissipation, and is typically assumed to be ≈ 0.2 (*Oakey*, 1982). Estimates of Γ in the ocean show a range of values, typically between ~ 0.1 and 0.3, that depend on a number of different factors (see *Ivey et al.*, 2008, for a recent review).

To estimate K_V from the inferred and modelled dissipation rates, N^2 was estimated as a function of time at the height of each ADV using the fit to the TDR data from Section 3.4.2 (see e.g. Figure 3.7). Plots of K_V against tidal phase, similar to the dissipation results, are presented in Figure 7.6. The linear relationship to ϵ is clear, with a similar dependence on phase, and similar patterns in the tidal and wave modelled values. The mean value of K_V at *M05* inferred from the ϵ measurements for the rising tide is $(1.4 \pm 0.07) \times 10^{-3}\,\mathrm{m^2/s}$, whereas that predicted by tidal shear scaling is $(0.5 \pm 0.02) \times 10^{-3}\,\mathrm{m^2/s}$– different by a factor of 3.

Buoyancy Flux

Due to experimental limitations, it was not possible to reliably measure the turbulent buoyancy flux, $\overline{\rho' w'}$. Though temperature was recorded by the ADVs, measurement of the turbulent temperature fluctuations is confounded by the low sampling rate of the thermistor (1 Hz), by the long thermal time constant (compared to the ADV ping rate), and by not collecting co-located temperature and velocity measurements. Worse than this, the magnitude of the observed temperature fluctuations during

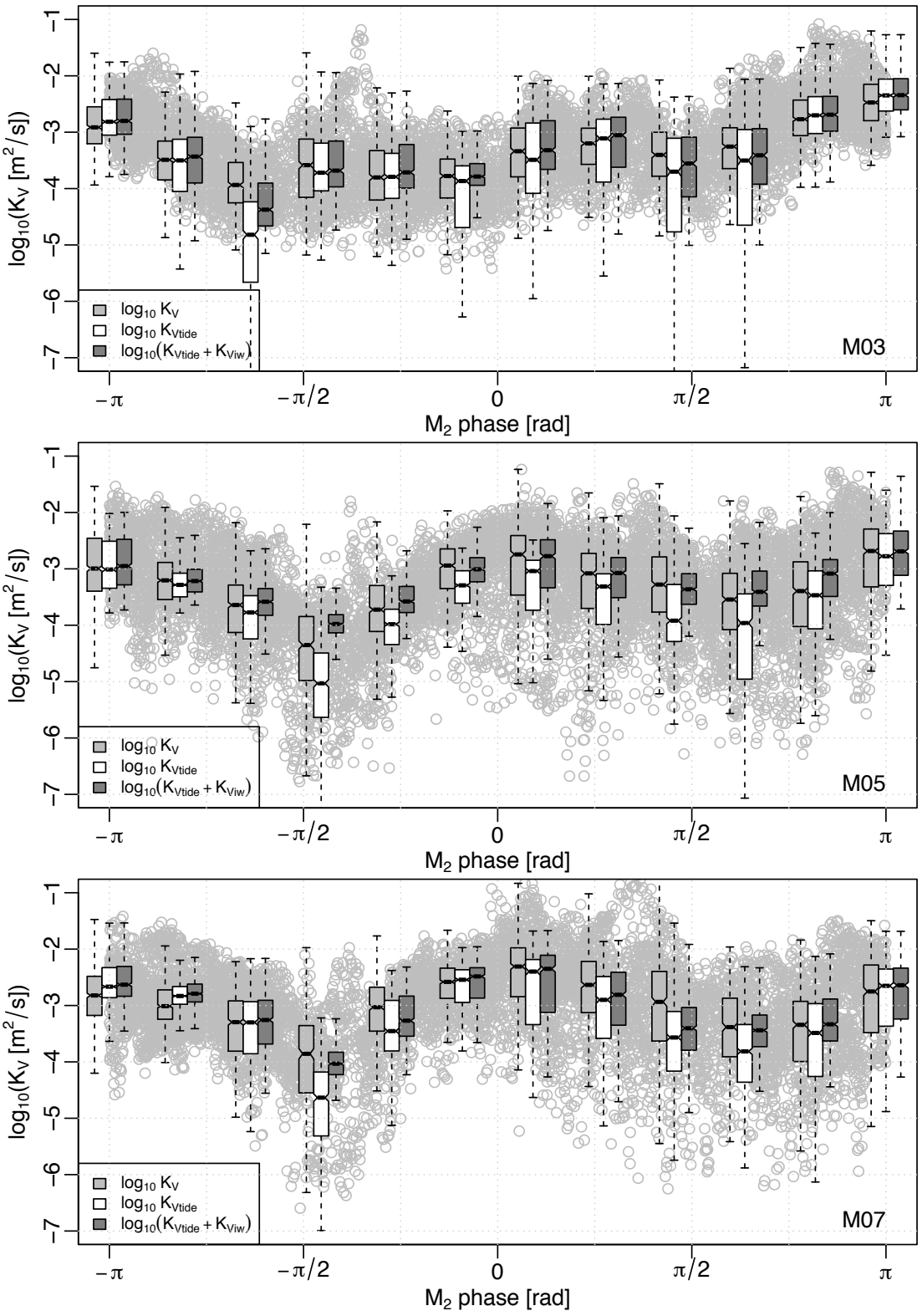

Figure 7.6: Predicted vertical diffusivities as a function of tidal phase at *M03*, *M05*, and *M07*. Shading for boxplots as in Figure 7.5.

internal wave events was only between 2-5 times the resolution of the sensor, giving large uncertainty. Finally, the orientation of the sensor should be as close to vertical as possible, to prevent contamination of the w' field by u', as discussed in Section 6.3.2.

Alternatively, the buoyancy flux can be estimated from the eddy diffusivity model, where

$$J_b = \frac{g}{\rho}\overline{\rho' w'} = K_V N^2, \tag{7.11}$$

or more simply, $J_b = \Gamma\epsilon$. The mean value of buoyancy flux at *M05* (averaged over all phases and tidal cycles) is $4.1 \times 10^{-6}\,\mathrm{W/kg}$.

To provide some context, the above value can be compared with the vertically-integrated buoyancy fluxes estimated from a numerical model in *Saucier and Chassé* (2000) (their Equation 24). To cast the present estimate of J_b into the same form as *Saucier and Chassé* (2000), it is necessary to multiply by the mean density and integrate over the depth. As a lower bound, assuming the water column average J_b occurs only over the bottom metre where dissipation was measured by the ADV, this gives a vertically integrated value of $4.2 \times 10^{-3}\,\mathrm{W/m^2}$. This is approximately a factor of 10 to 20 times larger than the mean buoyancy flux estimated by *Saucier and Chassé* (2000) for the same region (their Figure 21). Due to the multitude of assumptions involved, this comparison should be treated with some caution, but, it indicates that the processes contributing to mixing at the SLEIWEX field site are unresolved in current numerical models. While the model of *Saucier and Chassé* (2000) compares well with various observations and is a good representation of the estuary overall, localized mixing processes are smeared out by the overly simplified mixing parameterizations.

7.5 Conclusions

In this chapter, it was demonstrated that a simple internal wave proxy can be related to the energy and energy flux of individual internal wave events. The implication of this relationship is that it permits an estimate of wave energy at a given location as a function of time using only a moored ADP.

The time series of wave energy was used with a simple "box" model for turbulence.

The results suggest that on average, during the rising phase of the tide, near-bottom dissipation due to wave shoaling is between 2 and 5 times higher than dissipation from tidal shear processes. This effect was most pronounced at *M05*, which was deployed near the depth of the nominal pycnocline.

The implications for vertical mixing were explored, by estimating the vertical diffusivity and buoyancy flux using an eddy diffusivity approximation with the measured stratification. During the rising tide when waves are present, K_V is approximately three times higher on average than predictions from the tidal shear scaling. This is in contrast to the falling tide, when tidal shear dominates. A crude estimate of buoyancy flux suggests that locally it may be 10 to 20 times higher than calculated in a numerical model of the region. This likely represents a lower bound, as we have considered only mixing forced by near-bottom turbulence.

Chapter 8

Conclusions

8.1 Summary

This thesis presents measurements which show that shoaling internal waves make a significant contribution to near-bottom turbulent dissipation rates at a location in the St. Lawrence Estuary.

Chapters 2 and **3** introduced the SLEIWEX 2008 field site, experiment, and the relevant background conditions. A CTD survey revealed a tight relationship between temperature and salinity, permitting estimates of the water density from measurements of temperature alone. This relationship was exploited in later chapters to estimate the time varying density structure. Wave arrival at the field site was explored by manual detection and by using a proxy for internal wave energy. Most of the observed internal waves arrive at the field site during the rising tide.

In **Chapter 4**, a new method for inferring internal wave density structure from acoustic current profiler measurements was proposed, utilizing a relaxation scheme to estimate the streamfunction. The method was shown to be relatively insensitive to noise and background shear, and performed better than previously proposed methods using measurements from the SLEIWEX 2008 data.

The streamfunction method from Chapter 4 was applied to data from the SLEIWEX 2008 experiment in **Chapter 5** to estimate wave energy and horizontal energy flux. Overall, there is an equipartition between kinetic and available potential energy, with $KE = (1.02 \pm 0.15)APE$. Variability in this relationship for individual observations may be due to the observation of waves at different stages of shoaling.

The horizontal internal wave energy flux was estimated by 1) measuring all

components of the linear and nonlinear energy flux terms f_E, and by 2) using the product of the mode-1 internal wave phase speed and the total energy $c\mathcal{E}$. Overall there was good agreement between the two estimates, with $\langle f_E \rangle = (0.91 \pm 0.05)\langle c\mathcal{E} \rangle$, where the angle brackets represent a integral over time and depth. The energy flux measured with $\langle c\mathcal{E} \rangle$ was determined to be the preferred estimate, due to measurement uncertainties in $\langle f_E \rangle$ resulting from under-sampling of the water column and incomplete removal of the background flow.

Measurements of turbulence from near-bottom ADVs in **Chapter 6** suggest that the overall pattern of dissipation ϵ at the SLEIWEX field site is controlled by tidal flow. Measurements of shear production of turbulence P using the Reynolds stress suggests that it is slightly larger than ϵ on average. It is uncertain if the observed excess of P is caused by the presence of a buoyancy flux (which was unmeasured) or is a result of vertical alignment uncertainties.

Dissipation rates inferred by spectral analysis of the ADVs during a period of internal wave shoaling were observed to be as much as an order of magnitude higher than predicted by a tidal shear model of turbulence. The source of the turbulence was explored by examining individual velocity spectra, and it was determined that the observed turbulence is unlikely to be caused by a heaved near-bottom boundary layer. The evolution of the turbulence spectral shape suggests an excess of production as the wave arrives, followed by an excess of dissipation after the wave passes. This implies that turbulence is at least partly locally generated by the wave, rather than simply being transported within it as a trapped core.

In **Chapter 7** the measurements of wave energy were brought together with the dissipation measurements, to determine the overall importance of internal wave induced turbulence at the field site. It was found that there is a significant relationship between the individual measurements of internal wave energy from Chapter 5 and a simple proxy for internal waves based only on the currents. By using this relationship to infer the time-varying internal wave energy flux at the SLEIWEX field site, a simple model for near-bottom dissipation was developed incorporating tidal shear and internal waves. It was found that near the nominal pycnocline depth (at mooring *M05*), the internal wave turbulence model is required to explain observed dissipation rates during the rising phase of the tide. Offshore of this location (at *M07*) a similar

but less pronounced relationship was found. Further onshore (at *M03*) the tidal shear model was representative of the measured dissipation, implying that internal wave generated turbulence is not significant there. The implications for vertical mixing were explored, suggesting that on average during the rising tide mixing caused by internal waves is three times larger than that caused by tidal shear.

8.2 Future Work

Based on the results presented in this thesis, several avenues for future work can be suggested. The first section deals with studies which may be undertaken with the present data set, as extensions to the current results. The second section proposes new experiments to build on the results of the current study.

8.2.1 Extensions to the Present Work

Improvements to the Streamfunction Method

The relaxation method for streamfunction determination proposed here uses a single vertical density profile upstream of the wave to infer the heaved density field. In situations where velocity data are collected simultaneously with vertical density profiles (e.g. from a ship instead of a bottom mooring), it should be possible to combine the two to obtain an improved streamfunction estimate. In this way, any vertical profile that goes through the wave could be used to constrain the relaxation, eliminating the dependence on the single upstream density estimate. This may be accomplished through an iterative procedure, where the computed streamfunction is adjusted based on any available measurements, and the algorithm is repeated to minimize residuals. Such an approach would also present a good opportunity to test the assumptions involved in the streamline-to-isopycnal mapping. Additionally, the technique could be further tested using a directed experiment involving rapid vertical sampling, perhaps with two or more free-fall profilers.

Further tests examining the sensitivity of the techniques to background flows with divergence (resulting either from rapid heaving of a simple shear layer or due to uncertainty in the wave propagation direction) are warranted. Initial tests indicate that the SR method is relatively insensitive to the presence of divergence, while streamlines produced by the MS technique are significantly distorted. This may be one of the reasons the SR method was superior for the SLEIWEX data.

Event-Based Study of Boluses and Turbulence

The approach taken in this thesis for assessing the influence of internal waves on turbulence has made use of the time series measurements, rather than focusing entirely on individual events. There may be much to be learned from such an approach, particularly with regards to quantifying the difference between large and small wave events and further observing the internal structure of the boluses produced during shoaling. The *M05* and *M07* moorings each contained a downward looking ADP, profiling velocity in 4 cm bins to the bottom. Excessive tilts and orientation uncertainties led to the decision to not include these instruments in the present study, but future data processing techniques may permit usable data to be extracted. No such studies of boluses in a natural environment have yet been undertaken, to the author's knowledge.

8.2.2 Future Experiments

Generation

One of the most obvious avenues for future exploration related to internal wave at the SLEIWEX field site is the question of generation. An attempt to collect observations relating to generation was made during the 2008 experiment, but the resulting data are incomplete and do not permit unambiguous conclusions about generation mechanisms. Some hypotheses have been formulated for generation, but they remain to be tested. For completeness, they will be outlined in this section.

During the 2008 experiment, vigorous vertical motions were observed near the Cap-de-la-Tête-au-Chien headland along the Northern coast (see Figure 2.1). The internal motions resulted in visible surface rip-currents and "boils", as well as signatures of overturns in CTD profiles. During the final stages of the experiment, just prior to mooring recovery, the *RV Coriolis II* was used to perform underway ADP transects near the headland. Two examples are presented in Figure 8.1, one during the rising tide and one approximately 6 hours later during the falling tide.

In Figure 8.1, the interaction of the flow with the headlands is obvious, particularly during the rising tide (i.e. flood – top panel). Depth averaged vertical velocities near the headland features during flood are at times in excess of 0.2 m/s, and the observed patterns indicate lee wave generation. Analysis of the across-channel velocities (not shown here) indicates that there is also flow around the headlands.

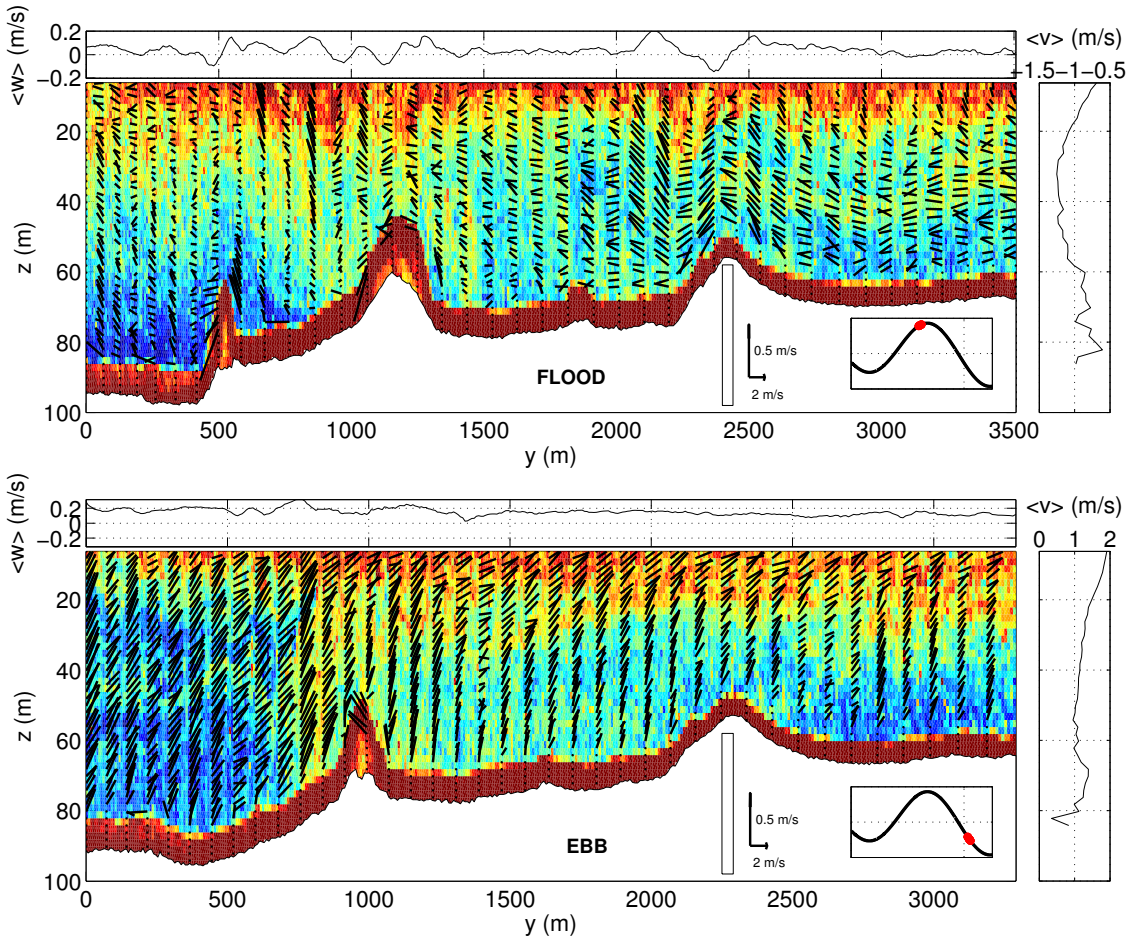

Figure 8.1: Ship-mounted ADCP transects parallel to the Northern coast, near Cap-de-la-Tête-au-Chien (see Figure 2.1). Acoustic backscatter is indicated by the colors, and the two-dimensional currents (v, w) are represented by the line segments. A scale for the velocity vectors is provided in each plot, along with the aspect ratio, and the phase of the tide during which the transect was acquired. Top: flow during the rising (flood) tide. Mean flow is to the left, (i.e. upstream). Bottom: flow during the falling (ebb) tide. Mean flow is to the right (downstream). The plots above and below show the depth and horizontally averaged velocities.

Similarly, during the falling tide (i.e. ebb) strong vertical motions associated with the protruding headland can be seen (Figure 8.1 – lower panel). These vertical motions appeared simultaneously with the surface features described previously. There is also a mean upward vertical velocity throughout the transect, of approximately 0.1 m/s. How this upward velocity is balanced by continuity elsewhere in the domain is an open question.

The fate of any lee waves generated from the headlands is unknown. Further, it is

unclear if waves generated on the rising tide are the ones observed at the SLEIWEX field site. The mode-1 phase speeds suggest that the time required to propagate from the headland to the field site should be about 4 hours (with no background current), as opposed to the approximately 9 hour difference observed here. It is possible that the waves are advected by the background current, and therefore don't follow a straight path between the locations (see next section for a discussion of wave propagation).

Aside from internal wave generation, the role that the headlands may play in the overall mixing and circulation in the St. Lawrence Estuary is unknown. Studies at other headlands have shown that lee wave generation and horizontal flow separation are a significant sink of energy from the barotropic flow (*Signell and Geyer*, 1991; *Edwards et al.*, 2004; *McCabe et al.*, 2006). How the interaction between baroclinic flow and coastal headlands in the St. Lawrence Estuary contributes to drag, wave generation, and mixing is open question.

Propagation

Answering questions regarding wave propagation within the domain will aid interpretation of the wave dissipation and generation results, by connecting the two processes spatially. This section will outline some of the outstanding questions related to wave propagation, and discuss avenues for future exploration.

Question 1: How is wave propagation affected by the background hydrography, flow, and shear?

Question 2: Is the phase-dependent arrival of waves at the field site related to the timing of the generation process, or to redistribution resulting from the background flow (or both)?

The success of the shore-based photogrammetry used in this experiment suggests that similar techniques may help answer these two questions. Autonomous camera systems that can be deployed for longer periods of time could reveal the wave field through surface signatures, when the weather conditions are favourable. Land-based radar may provide a similar perspective, unaffected by weather conditions.

The use of satellite or airborne synthetic aperture radar would provide a broader view of internal waves through their surface signatures throughout the estuary.

During this study, attempts were made to access the RadarSat[1] database and to schedule acquisition of images. The attempts were not as productive as hoped. Archived images were generally of insufficient spatial resolution to reveal internal waves, or the polarization band in which they were acquired was not suited to detecting surface roughness features of the appropriate scale. New image acquisition was hampered by conflicts with other Government of Canada departments, such as the Canadian Ice Service.

Question 3: How do phenomena such as strong vertical or horizontal shear and fronts affect wave propagation?

Question 4: What happens when waves of different origins interact (see e.g. Figure 2.3)?

Addressing these two questions will likely require specifically executed experiments, possibly using three-dimensional numerical modelling process studies to aid in the interpretation of results. Recent observations of interacting wave trains reveal a complicated interaction process which is difficult to interpret, even from a relatively well sampled dataset (*Shroyer et al.*, 2010a; *Wang and Pawlowicz*, 2012).

Question 5: Finally, can the wave redistribution be modelled in a simple manner, perhaps to be included as a component in a regional circulation model?

Tests with simple kinematic models of waves propagating in time-varying currents indicated that this may be an avenue for modelling wave redistribution, given a variety of known generation regions (or mechanisms). Models of this type could be run in parallel with a circulation model, and if combined with parameterizations for wave generation and dissipation, they could be used to identify other regions of wave shoaling.

Measurements of Mixing

The final topic to which future studies should be directed is obtaining direct measurements of mixing and buoyancy flux resulting from the internal waves. Such

[1]RadarSat I and II are owned and operated by MacDonald Dettwiler and Associates, with access to imagery made possible through collaboration with the Government of Canada.

measurements were not possible with the present data set. *Bourgault et al.* (2008) observed that boluses may act to reduce water-column turbulence, by advecting dense water up the slope and thereby increasing stratification. They made use of vertical profiles of turbulence, but only sampled to within a few metres of the bottom. The results presented in this thesis suggest that near-bottom turbulence levels are elevated under the waves, especially near the pycnocline depth where the most vigorous overturning is expected. As *Bourgault et al.* (2008) sampled only for a short period of time at a location above the pycnocline depth, it is possible that they missed the largest turbulence signals. Comparison between the two experiments is difficult, as the present study lacked water column turbulence measurements, and had only dissipation estimates near the bottom. The original proposal included simultaneous ADV measurements and vertical microstructure profiles, however, the profiler was lost on the first day of sampling.

Estimates of near-bottom buoyancy flux could be obtained by pairing the ADVs with fast response thermistors, sampling as close to the acoustic scattering volume as possible (see e.g. *Davis and Monismith*, 2011, for a recent example). Additionally, configuring the ADVs to sample at higher rates would permit direct calculation of the TKE. Such a calculation was not performed for this study, as the sampling rates were such that the changing wavenumber range in each spectrum (due to the frozen turbulence hypothesis) masked the true rate of change of TKE. Estimates of TKE and buoyancy flux would permit further examination of the near-bottom turbulence energy budget, which was not possible in this study (see e.g. Sections 6.3.2 and 7.4.2).

Measurements of buoyancy flux would also permit instantaneous estimates of the mixing efficiency. Several authors have suggested that a fixed value of $\Gamma = 0.2$ is unrealistic when the turbulence is not steady state, especially during the early stages of overturning (see e.g. *Smyth et al.*, 2001; *Moum et al.*, 2003). An enhanced mixing efficiency associated with the waves, even if only for short periods at a time, could lead to greatly enhanced buoyancy fluxes.

Appendix A

ADP/ADV Coordinate Transformations

A.1 Coordinate Transformations

Acoustic instruments use returns from acoustic beams to measure 3-dimensional water velocity. The measured *beam* velocities can be translated to an orthogonal coordinate system (XYZ) using a transformation matrix, and then subsequently rotated to give velocities in an East-North-Up (ENU) coordinate system.

Due to the variety of acoustic Doppler system configurations, differing between and within each manufacturer, there is no general procedure for obtaining earth-referenced velocities. The purpose of this appendix is to summarize a standard set of instructions for transforming instruments used in the SLEIWEX 2008 field program.

The following formula is the general formula to be used for a 3 axis rotation to correct heading, pitch and roll.

$$
\begin{aligned}
R &= \overbrace{\begin{bmatrix} cH & sH & 0 \\ -sH & cH & 0 \\ 0 & 0 & 1 \end{bmatrix}}^{R_M} \overbrace{\begin{bmatrix} 1 & 0 & 0 \\ 0 & cP & -sP \\ 0 & sP & cP \end{bmatrix}}^{R_S} \overbrace{\begin{bmatrix} cR & 0 & sR \\ 0 & 1 & 0 \\ -sR & 0 & cR \end{bmatrix}}^{R_F} \\
&= \begin{bmatrix} sH*sP*sR + cH*cR & cP*sH & -cR*sH*sP + cH*sR \\ cH*sP*sR - cR*sH & cH*cP & -cH*cR*sP - sH*sR \\ -cP*sR & sP & cP*cR \end{bmatrix} \qquad \text{(A.1)}
\end{aligned}
$$

where $cH = \cos(\phi_H), sH = \sin(H), cP = \cos(\phi_P), sP = \sin(\phi_P), cR = \cos(\phi_R)$, and $sR = \sin(\phi_R)$. The rotation is performed according to:

$$\begin{bmatrix} E \\ N \\ U \end{bmatrix} = R * \begin{bmatrix} S \\ F \\ M \end{bmatrix}.$$

The angles $\phi_{H,P,R}$ represent the heading, pitch and roll relative to the intermediate starboard-forward-mast (SFM) axes, while the actual heading, pitch and roll output by the instrument are written $\theta_{H,P,R}$. For a given instrument, Table A.1 presents a summary of how to obtain the inputs to Equation A.1.

Instrument	ϕ_H	ϕ_P	ϕ_R	S	F	M
1. RDI up	θ_H	$\arctan(\tan(\theta_P)\cos(\theta_R))$	θ_R	$-X$	Y	$-Z$
2. RDI down	θ_H	$\arctan(\tan(\theta_P)\cos(\theta_R))$	$-\theta_R$	X	Y	Z
3. ADP up	$\theta_H - 90$	$-\theta_P$	$-\theta_R$	X	Y	Z
4. ADP down	$\theta_H - 90$	$-\theta_P$	$-\theta_R$	X	Y	Z
5. SL08-ADP up	$\theta_H - 90$	θ_R	$-\theta_P$	X	Y	Z
6. PCADP up	$\theta_H - 90$	θ_R	$-\theta_P$	X	Y	Z
7. PCADP down	$\theta_H - 90$	θ_R	$-\theta_P$	X	Y	Z
8. Aquadopp up	$\theta_H - 90$	θ_R	$-\theta_P$	X	Y	Z
9. Aquadopp down	$\theta_H - 90$	θ_R	$-\theta_P$	X	$-Y$	$-Z$
10. ADV/Vector up	$\theta_H - 90$	θ_R	$-\theta_P$	X	$-Y$	$-Z$
11. ADV/Vector down	$\theta_H - 90$	θ_R	$-\theta_P$	X	Y	Z
12. Cabled-Vector up	$\theta_H - 90$	θ_R	$-\theta_P$	X	Y	Z
13. Cabled-Vector down	$\theta_H - 90$	θ_R	$-\theta_P$	X	$-Y$	$-Z$
14. SL08-Vector m07 up	$(\theta_H - 90) - 90$	$-\theta_P$	$-\theta_R$	X	Y	Z
15. SL08-Vector m08 up	$(\theta_H - 90) + 90$	θ_P	θ_R	X	Y	Z

Table A.1: Summary table for XYZ to ENU rotation procedures for various instruments, including deployments specific to the SLEIWEX 2008 fieldwork.

A.2 Mooring Diagrams

This appendix contains sketches of the moorings, illustrating the relative orientations of instruments on the frames, as well as a sketch showing the orientation of the frames on the bottom after deployment.

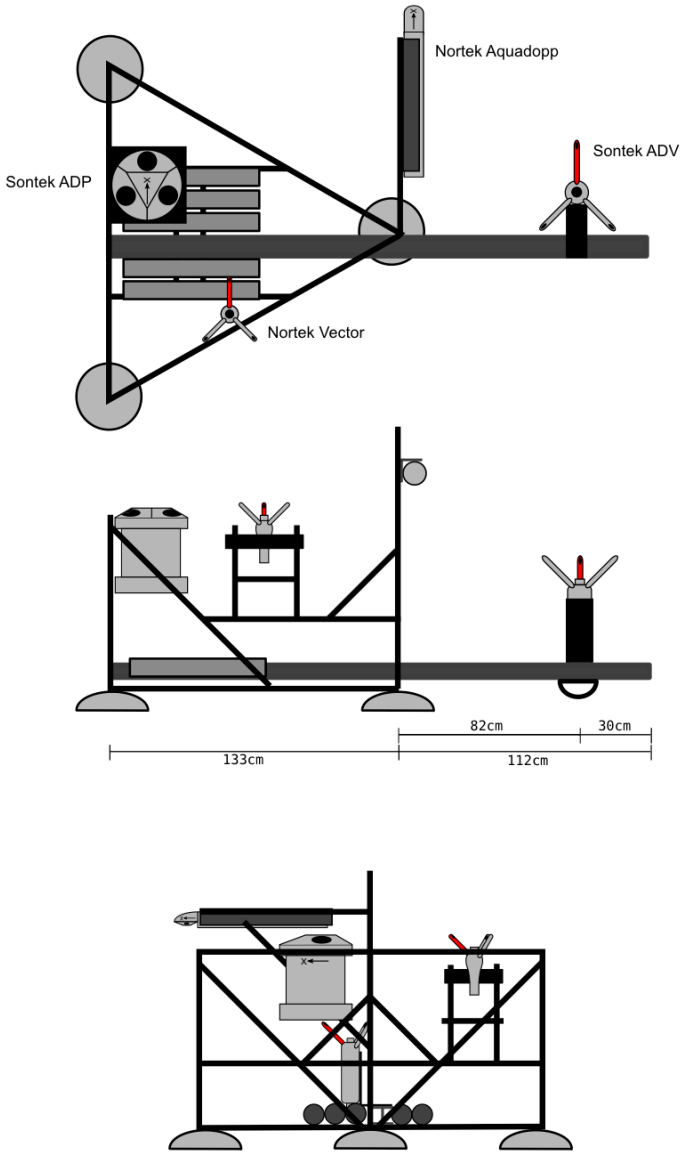

Figure A.1: Mooring sketch for *M05*.

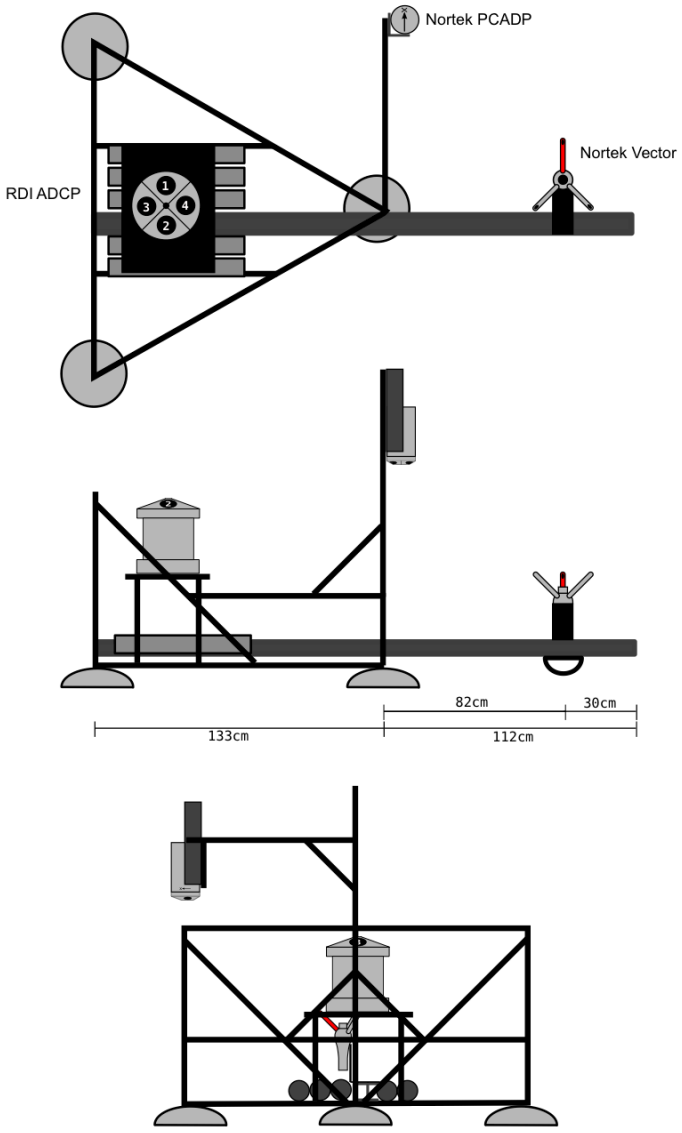

Figure A.2: Mooring sketch for *M07*.

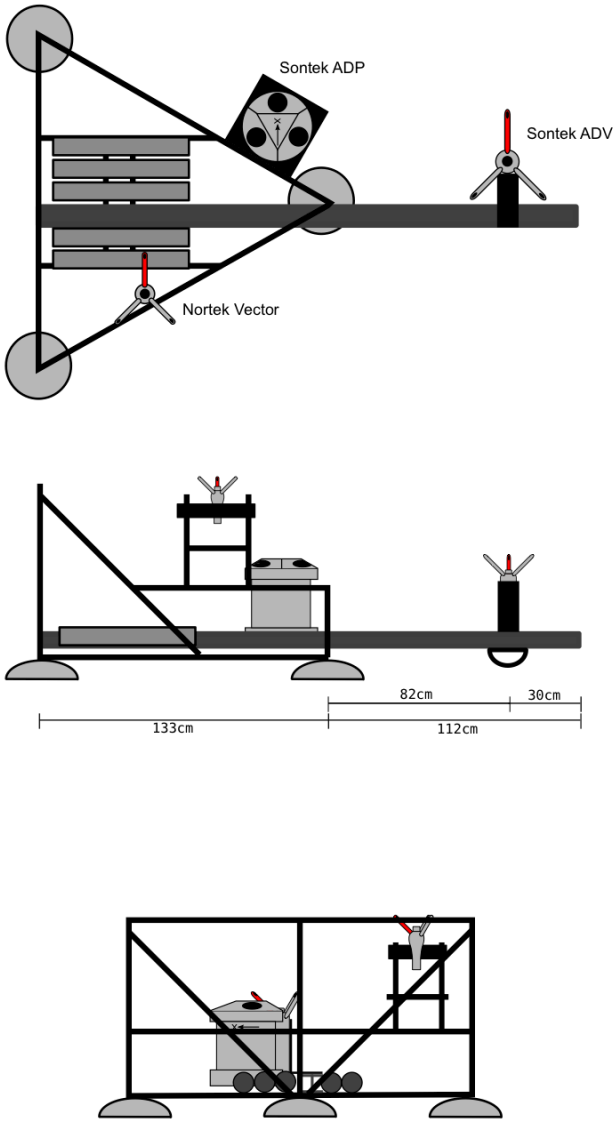

Figure A.3: Mooring sketch for *M08*.

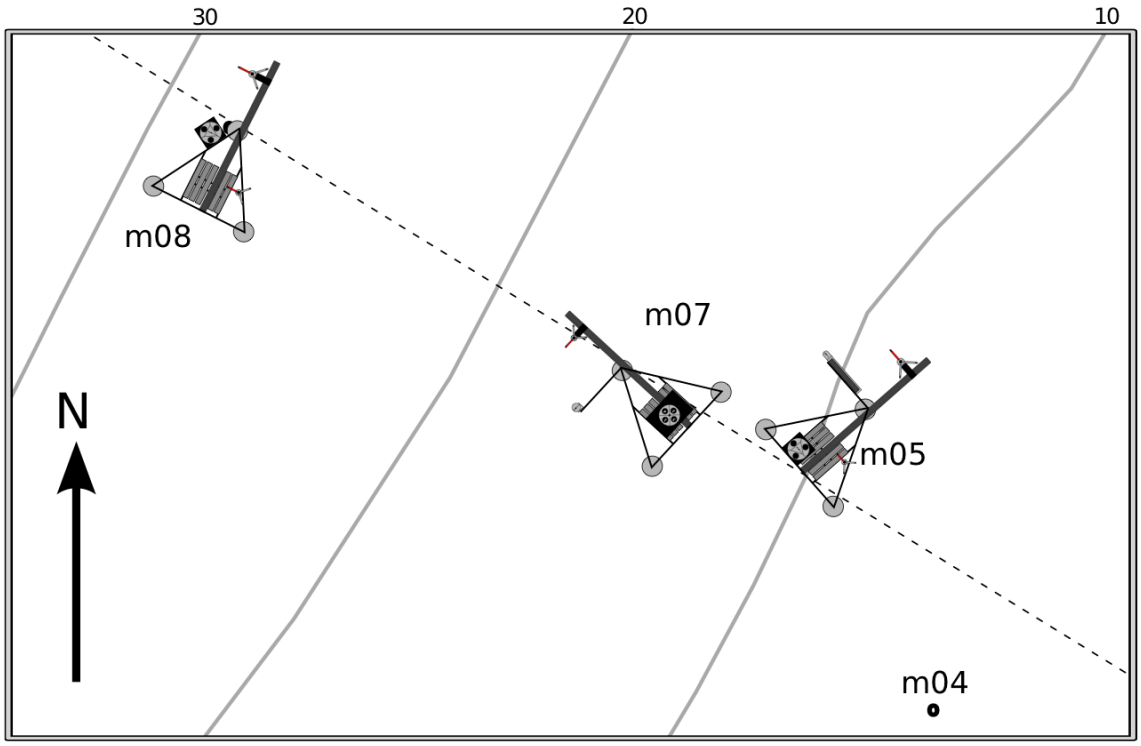

Figure A.4: Orientations of moorings after deployment.

Appendix B

Synthetic Internal Solitary Wave Fields

The purpose of this appendix is to outline the method used for creating the solitary internal wave fields used in various aspects of the thesis. Section B.1 will outline the theoretical basis behind the calculation of the wave fields, while Section B.2 will summarize the numerical model used.

The numerical model was graciously provided by Dr. Kevin Lamb. No modifications to the code were made for this study.

B.1 Theory

Following *Stastna and Lamb* (2002), consider an internal solitary wave propagating over a flat bottom with speed c in a fluid with undisturbed density $\overline{\rho}(z)$ and horizontal velocity $U(z)$. In a frame moving with the wave, the isopycnal displacement $\eta(x,z)$ is defined by

$$\rho(x,z) = \overline{\rho}(z - \eta(x,z)). \tag{B.1}$$

After some algebraic manipulations of the governing equations (the dimensionless Boussinesq Euler equations without rotation, see *Stastna and Lamb* (2002) and references therein), it can be shown that η satisfies the nonlinear elliptic eigenvalue problem

$$\nabla^2\eta = -\frac{U(z-\eta)}{c-U(z-\eta)}\left[\left(\frac{\partial\eta}{\partial x}\right)^2 + \left(\frac{\partial\eta}{\partial z} - 2\right)\frac{\partial\eta}{\partial z}\right] - \frac{N^2(z-\eta)}{(c-U(z-\eta))^2}\eta. \tag{B.2}$$

For $U = 0$, this can be seen to reduce to the familiar Dubriel-Jacotin-Long (DJL) equation for large amplitude internal solitary waves (see e.g. *Turkington et al.*, 1991).

The boundary conditions for η are

$$\begin{aligned} \eta(x,0) = \eta(x,1) &= 0 \\ \lim_{x\to\pm\infty} \eta(x,z) &= 0, \end{aligned} \tag{B.3}$$

and after Equation B.2 is solved for η and c, the streamfunction of the wave induced motion is found with

$$\psi = \psi^b(z-\eta) - \psi^b(z) + c\eta, \tag{B.4}$$

where the streamfunction of the background flow ψ^b is given by

$$\psi^b = \int U(z)\, dz. \tag{B.5}$$

The wave-induced velocities can then be recovered from Equation B.4.

B.2 The Internal Solitary Wave Model

The details of the computational algorithm used by *Stastna and Lamb* (2002) to solve Equation B.2 are provided in their Appendix. Their method is a generalization of the variational algorithm proposed by *Turkington et al.* (1991) which involves specifying the background velocity and density fields, along with an available potential energy. The algorithm then iteratively finds the wave solution that minimizes the kinetic energy.

The various fields output by the model include: the horizontal and vertical velocities (u, w), the wave speed c, the nondimensional density ρ, the isopycnal displacements η, and the nondimensional available potential energy density. Example wave fields for a hyperbolic tangent density profile with no background flow in 100 m of water are shown in Figure B.1. The wave phase speed was calculated to be 0.548 m/s.

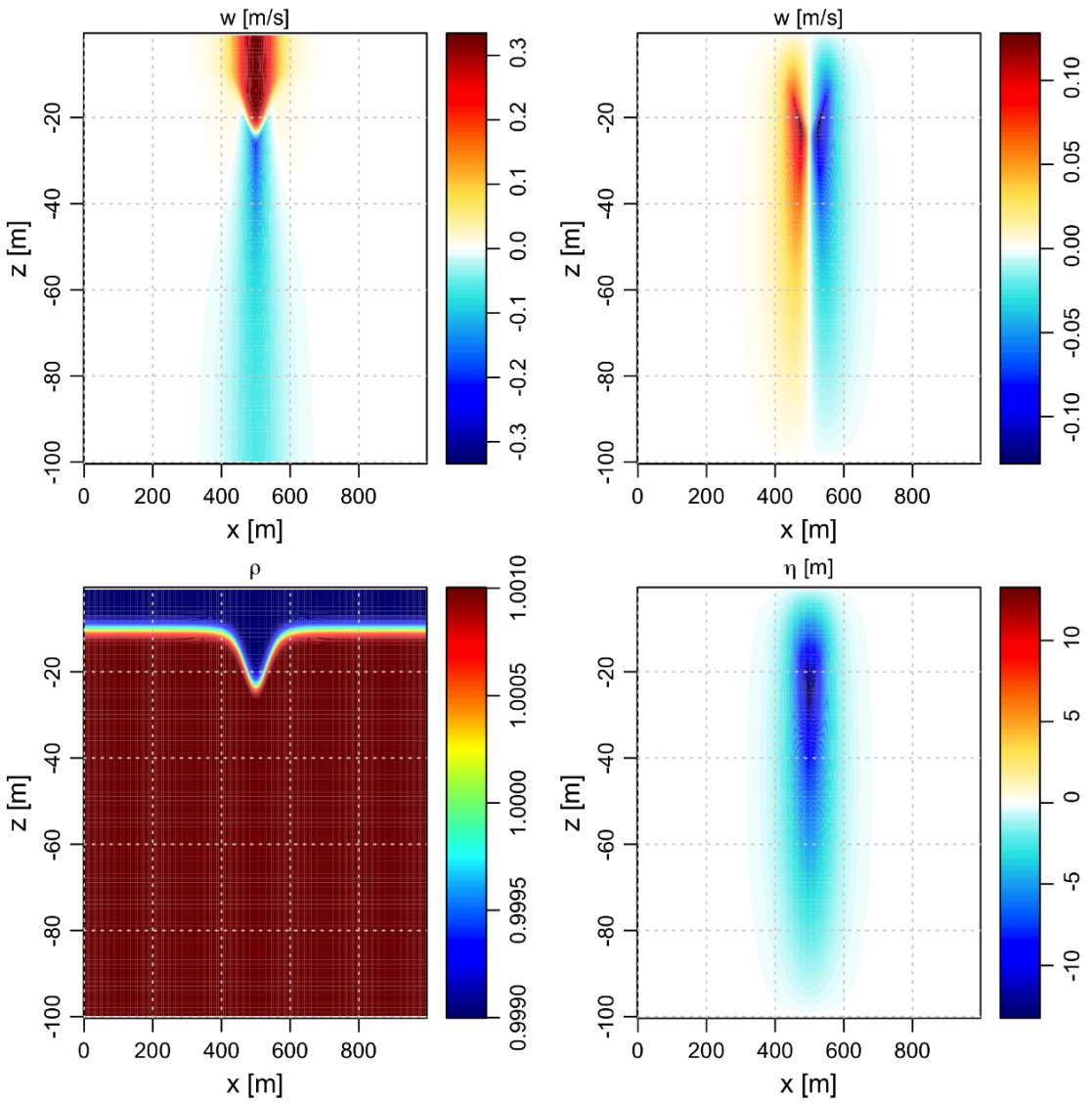

Figure B.1: Example internal solitary wave calculated using the model of *Stastna and Lamb* (2002). Proceeding clockwise, the fields are: the horizontal velocity u, the vertical velocity w, the isopycnal displacement η, and the nondimensional density field ρ.

Bibliography

Aghsaee, P., L. Boegman, and K. Lamb, Breaking of shoaling internal solitary waves, *Journal of Fluid Mechanics*, *1*, 1–29, 2010.

Alford, M., Redistribution of energy available for ocean mixing by long-range propagation of internal waves., *Nature*, *423*, 159–62, 2003.

Batchelor, G., *The theory of homogeneous turbulence*, Cambridge University Press, 1953.

Bogucki, D., and C. Garrett, A simple model for the shear-induced decay of an internal solitary wave, *Journal of Physical Oceanography*, *23*, 1767–1776, 1993.

Bourgault, D., Shore-based photogrammetry of river ice, *Canadian Journal of Civil Engineering*, *35*, 80–86, 2008.

Bourgault, D., and D. Kelley, On the reflectance of uniform slopes for normally incident interfacial solitary waves, *Journal of Physical Oceanography*, *37*, 1156–1162, 2007.

Bourgault, D., and D. E. Kelley, Wave-induced boundary mixing in a partially mixed estuary, *Journal of Marine Research*, *61*, 553–576, 2003.

Bourgault, D., F. Saucier, and C. Lin, Shear instability in the St. Lawrence Estuary, Canada: A comparison of fine-scale observations and estuarine circulation model results, *Journal of Geophysical Research*, *106*, 9393–9410, 2001.

Bourgault, D., D. Kelley, and P. Galbraith, Interfacial solitary wave run-up in the St. Lawrence Estuary, *Journal of Marine Research*, *63*, 1001–1015, 2005.

Bourgault, D., M. Blokhina, R. Mirshak, and D. Kelley, Evolution of a shoaling internal solitary wavetrain, *Geophysical Research Letters*, *34*, 2007.

Bourgault, D., D. E. Kelley, and P. S. Galbraith, Turbulence and boluses on an internal beach, *Journal of Atmospheric and Oceanic Technology*, *66*, 563–588, 2008.

Bourgault, D., D. C. Janes, and P. S. Galbraith, Observations of a large-amplitude internal wave train and its reflection off a steep slope, *Journal of Physical Oceanography*, *41*, 586–600, 2011.

Chang, M., R. Lien, T. Tang, E. D'Asaro, and Y. Yang, Energy flux of nonlinear internal waves in northern South China Sea, *Geophysical Research Letters*, *33*, 2006.

Cyr, F., D. Bourgault, and P. S. Galbraith, Interior versus boundary mixing of a cold intermediate layer, *Journal of Geophysical Research*, *116*, C12029+, 2011.

Davis, K. A., and S. G. Monismith, The modification of bottom boundary layer turbulence and mixing by internal waves shoaling on a barrier reef, *Journal of Physical Oceanography*, *41*, 2223–2241, 2011.

Deguise, J., High frequency internal waves in the St. Lawrence estuary, Master's thesis, McGill University, 1977.

DFO, Webtide tidal prediction model (downloaded 2009-06-04), 2009, department of Fisheries and Oceans, Canada.

Edwards, K., P. MacCready, J. Moum, G. Pawlak, J. Klymak, and A. Perlin, Form drag and mixing due to tidal flow past a sharp point, *Journal of Physical Oceanography*, *34*, 1297–1312, 2004.

El-Sabh, M., Physical oceanography of the St. Lawrence Estuary, in *Hydrodynamics of Estuaries*, edited by B. Kjerfve, vol. 2, pp. 61–78, CRC Press, Florida, 1988.

Elgar, S., B. Raubenheimer, and R. Guza, Quality control of acoustic Doppler velocimeter data in the surfzone, *Measurement Science and Technology*, *16*, 1889, 2005.

Feddersen, F., Quality controlling surf zone acoustic Doppler velocimeter observations to estimate the turbulent dissipation rate, *Journal of Atmospheric and Oceanic Technology*, *27*, 2039–2055, 2010.

Fischer, H., E. List, R. Koh, J. Imberger, and N. Brooks, *Mixing in Inland and Coastal Waters, 483 pp*, Academic Press, San Diego. Calif, 1979.

Galbraith, P., Relating overturns to mixing and buoyancy flux., Ph.D. thesis, Dalhousie University, 1992.

Gill, A. E., *Atmosphere-ocean dynamics*, vol. 30 of *International geophysics series*, Academic Press, New York, 1982.

Goring, D., and V. Nikora, Despiking acoustic Doppler velocimeter data, *Journal of Hydraulic Engineering*, *128*, 117, 2002.

Green, M., Spectral estimates of bed shear stress at subcritical Reynolds numbers in a tidal boundary layer, *Journal of Physical Oceanography*, *22*, 1992.

Gregg, M., Diapycnal mixing in the thermocline: A review, *Journal of Geophysical Research*, *92*, 5249–5286, 1987.

Hebert, D., The available potential energy of an isolated feature, *Journal of Geophysical Research*, *93*, 556–564, 1988.

Helfrich, K., and W. Melville, Long nonlinear internal waves, *Annual Review of Fluid Mechanics*, *38*, 395–425, 2006.

Helfrich, K., and B. White, A model for large-amplitude internal solitary waves with trapped cores, *Nonlinear Processes in Geophysics*, *17*, 303–318, 2010.

Helfrich, K. R., Internal solitary wave breaking and run-up on a uniform slope, *Journal of Fluid Mechanics*, *243*, 133–154, 1992.

Huntley, D., A modified inertial dissipation method for estimating seabed stresses at low Reynolds numbers, with application to wave/current boundary layer measurements, *Journal of Physical Oceanography*, *18*, 339–346, 1988.

Ingram, R. G., Internal wave observations off Isle Verte, *Journal of Marine Research*, *36*, 715–724, 1978.

Ivey, G., K. Winters, and J. Koseff, Density stratification, turbulence, but how much mixing?, *Annual Review of Fluid Mechanics*, *40*, 169–184, 2008.

Ivey, G. N., and J. Imberger, On the nature of turbulence in a stratified fluid. Part I: the energetics of mixing, *Journal of Physical Oceanography*, *21*, 650–658, 1991.

JCGM, *Evaluation of measurement data – Guide to the expression of uncertainty in measurement*, Joint Committee for Guides in Metrology, 2008.

Jeffreys, H., and B. Jeffreys, *Methods of Mathematical Physics*, Cambridge University Press, 1956.

Kang, D., and O. Fringer, On the calculation of available potential energy in internal wave fields, *Journal of Physical Oceanography*, *40*, 2539–2545, 2010.

Kantha, L., and C. Clayson, *Small scale processes in geophysical fluid flows*, vol. 67, Academic Press, 2000.

Kim, S.-C., C. T. Friedrichs, J. P.-Y. Maa, and L. D. Wright, Estimating bottom stress in tidal boundary layer from acoustic Doppler velocimeter data, *Journal of Hydraulic Engineering*, *126*, 399–406, 2000.

Klymak, J., and J. Moum, Internal solitary waves of elevation advancing on a shoaling shelf, *Geophys. Res. Lett*, *30*, 2045, 2003.

Klymak, J. M., R. Pinkel, C.-T. Liu, A. K. Liu, and L. David, Prototypical solitons in the South China Sea, *Geophysical Research Letters*, *33*, doi:10.1029/2006GL025932, 2006.

Kolmogorov, A. N., The local structure of turbulence in incompressible viscous fluid for very large reynolds numbers, *Proceedings: Mathematical and Physical Sciences*, *434*, pp. 9–13, 1941a.

Kolmogorov, A. N., Dissipation of energy in the locally isotropic turbulence, *Proceedings: Mathematical and Physical Sciences*, *434*, pp. 15–17, 1941b.

Kundu, P. K., and I. M. Cohen, *Fluid Mechanics*, second ed., Academic Press, 2002.

Kunze, E., L. Rosenfeld, G. Carter, and M. Gregg, Internal waves in Monterey Submarine Canyon, *Journal of Physical Oceanography*, *32*, 1890–1913, 2002.

Lamb, K., A numerical investigation of solitary internal waves with trapped cores formed via shoaling, *Journal of Fluid Mechanics*, *451*, 109–144, 2002.

Lamb, K., Shoaling solitary internal waves: on a criterion for the formation of waves with trapped cores, *Journal of Fluid Mechanics*, *478*, 81–100, 2003.

Lamb, K., Energy and pseudoenergy flux in the internal wave field generated by tidal flow over topography, *Continental Shelf Research*, *27*, 1208–1232, 2007.

Lamb, K., On the calculation of the available potential energy of an isolated perturbation in a density-stratified fluid, *Journal of Fluid Mechanics*, *597*, 415–427, 2008.

Lamb, K. G., and V. T. Nguyen, Calculating energy flux in internal solitary waves with an application to reflectance, *Journal of Physical Oceanography*, *39*, 559–580, 2009.

Lien, R.-C., E. A. D'Asaro, F. Henyey, M.-H. Chang, T.-Y. Tang, and Y.-J. Yang, Trapped core formation within a shoaling nonlinear internal wave, *Journal of Physical Oceanography*, *42*, 511–525, 2012.

Lorenz, E., Available potential energy and the maintenance of the general circulation, *Tellus*, *7*, 157–167, 1955.

Marsden, R., A proposal for a neutral regression, *Journal of Atmospheric and Oceanic Technology*, *16*, 876–883, 1999.

Marsden, R., and R. Ingram, Correcting for beam spread in acoustic Doppler current profiler measurements, *Journal of Atmospheric and Oceanic Technology*, *21*, 1491–1498, 2004.

McCabe, R., P. MacCready, and G. Pawlak, Form drag due to flow separation at a headland, *Journal of Physical Oceanography*, *36*, 2136–2152, 2006.

Miles, J., On the stability of heterogeneous shear flows, *Journal of Fluid Mechanics*, *10*, 496–508, 1961.

Mirshak, R., Interfacial internal waves impacting sloped boundaries, Ph.D. thesis, Dalhousie University, 2008.

Mirshak, R., and D. Kelley, Inferring propagation direction of nonlinear internal waves in a vertically sheared background flow, *Journal of Atmospheric and Oceanic Technology*, *26*, 615–625, 2009.

Monin, A., and A. Yaglom, *Statistical fluid mechanics II*, MIT Press, 1975.

Moum, J., and W. Smyth, The pressure disturbance of a nonlinear internal wave train, *Journal of Fluid Mechanics*, *558*, 153–177, 2006.

Moum, J., D. Farmer, W. Smyth, L. Armi, and S. Vagle, Structure and generation of turbulence at interfaces strained by internal solitary waves propagating shoreward over the continental shelf, *Journal of Physical Oceanography*, *33*, 2093–2112, 2003.

Moum, J., D. Farmer, E. Shroyer, W. Smyth, and L. Armi, Dissipative losses in nonlinear internal waves propagating across the continental shelf, *Journal of Physical Oceanography*, *37*, 1989–1995, 2007a.

Moum, J. N., J. M. Klymak, J. D. Nash, A. Perlin, and W. D. Smyth, Energy transport by nonlinear internal waves, *Journal of Physical Oceanography*, *37*, 1968–1988, 2007b.

Nash, J., M. Alford, and E. Kunze, Estimating internal wave energy fluxes in the ocean, *Journal of Atmospheric and Oceanic Technology*, *22*, 1551–1570, 2005.

Oakey, N. S., Determination of the rate of dissipation of turbulent energy from simultaneous temperature and velocity shear microstructure measurements, *Journal of Physical Oceanography*, *12*, 256–271, 1982.

Osborn, T., Estimates of the local rate of vertical diffusion from dissipation measurements, *Journal of Physical Oceanography*, *10*, 83–89, 1980.

Ott, M. W., An improvement in the calculation of ADCP velocities, *Journal of Atmospheric and Oceanic Technology*, *19*, 1738–1741, 2002.

Press, W., S. Teukolsky, W. Vetterling, and B. Flannery, *Numerical recipes in C*, 3rd ed., Cambridge Univ. Press Cambridge MA, USA:, 2007.

Priestley, M. B., *Spectral Analysis and Time Series*, Academic Press, 1981.

Quaresma, L., J. Vitorino, A. Oliveira, and J. da Silva, Evidence of sediment resuspension by nonlinear internal waves on the western Portuguese mid-shelf, *Marine Geology*, *246*, 123–143, 2007.

R Development Core Team, *R: A Language and Environment for Statistical Computing*, R Foundation for Statistical Computing, Vienna, Austria, 2012, ISBN 3-900051-07-0.

RD Instruments, *Acoustic Doppler current profiler principles of operation: a practical primer*, RD Instruments, San Diego, CA, 1996.

RD Instruments, *ADCP coordinate transformations*, RD Instruments, San Diego, CA, 1997.

Saucier, F., and J. Chassé, Tidal circulation and buoyancy effects in the St. Lawrence Estuary, *Atmosphere-Ocean*, *38*, 505–556, 2000.

Scotti, A., and J. Pineda, Observation of very large and steep internal waves of elevation near the Massachusetts coast, *Geophysical Research Letters*, *31*, L22307, 2004.

Scotti, A., B. Butman, R. Beardsley, P. Alexander, and S. Anderson, A Modified Beam-to-Earth Transformation to Measure Short-Wavelength Internal Waves with an Acoustic Doppler Current Profiler, *Journal of Atmospheric and Oceanic Technology*, *22*, 583–591, 2005.

Scotti, A., R. Beardsley, and B. Butman, On the interpretation of energy and energy fluxes of nonlinear internal waves: an example from Massachusetts Bay, *Journal of Fluid Mechanics*, *561*, 103–112, 2006.

Scully, M., C. Friedrichs, and J. Brubaker, Control of estuarine stratification and mixing by wind-induced straining of the estuarine density field, *Estuaries and Coasts*, *28*, 321–326, 2005.

Shepherd, T., A unified theory of available potential energy, *Atmosphere Ocean*, *31*, 1–26, 1993.

Shroyer, E., J. Moum, and J. Nash, Energy transformations and dissipation of nonlinear internal waves over New Jersey's continental shelf, *Nonlinear processes in Geophysics*, *17*, 345–360, 2010a.

Shroyer, E. L., J. N. Moum, and J. D. Nash, Observations of polarity reversal in shoaling nonlinear internal waves, *Journal of Physical Oceanography*, *39*, 691–701, 2009.

Shroyer, E. L., J. N. Moum, and J. D. Nash, Vertical heat flux and lateral mass transport in nonlinear internal waves, *Geophysical Research Letters*, *37*, L08601, 2010b.

Shukla, J., and K. Saha, Computation of non-divergent streamfunction and irrotational velocity potential from the observed winds, *Monthly weather review*, *102*, 419–425, 1974.

Signell, R., and W. Geyer, Transient eddy formation around headlands, *Journal of Geophysical Research*, *96*, 2561–2575, 1991.

Smyth, W., J. Moum, and D. Caldwell, The efficiency of mixing in turbulent patches: inferences from direct simulations and microstructure observations, *Journal of Physical Oceanography*, *31*, 1969–1992, 2001.

SonTek, *SonTek ADVField Acoustic Doppler Velocimiter: Technical Documentation*, San Diego, CA, 2001.

Soulsby, R., *Dynamics of marine sands: a manual for practical applications*, Thomas Telford, 1997.

Sreenivasan, K., On the universality of the Kolmogorov constant, *Physics of Fluids*, *7*, 2778–2784, 1995.

Stapleton, K., and D. Huntley, Seabed stress determinations using the inertial dissipation method and the turbulent kinetic energy method, *Earth Surface Processes and Landforms*, *20*, 807–815, 1995.

Stastna, M., and K. Lamb, Large fully nonlinear internal solitary waves: The effect of background current, *Physics of Fluids*, *14*, 2987, 2002.

Sutherland, G., Inferred boundary mixing rates from density inversions in the St. Lawrence Estuary, Master's thesis, Memorial University of Newfoundland, 2009.

Tennekes, H., and J. Lumley, *A first course in turbulence*, The MIT press, 1972.

Turkington, B., A. Eydeland, and S. Wang, A computational method for solitary internal waves in a continuously stratified fluid, *Studies in Applied Mathematics*, *85*, 93–127, 1991.

Venayagamoorthy, S., and O. Fringer, Nonhydrostatic and nonlinear contributions to the energy flux budget in nonlinear internal waves, *Geophysical research letters*, *32*, 15603–15603, 2005.

Venayagamoorthy, S., and O. Fringer, On the formation and propagation of nonlinear internal boluses across a shelf break, *Journal of Fluid Mechanics*, *577*, 137–159, 2007.

Wallace, B., and D. Wilkinson, Run-up of internal waves on a gentle slope in a two-layered system, *Journal of Fluid Mechanics*, *191*, 419–442, 1988.

Wang, C., and R. Pawlowicz, Propagation speeds of strongly nonlinear near-surface internal waves in the Strait of Georgia, *Journal of Geophysical Research*, *116*, C10021+, 2011.

Wang, C., and R. Pawlowicz, Oblique wave-wave interactions of nonlinear near-surface internal waves in the strait of georgia, *Journal of Geophysical Research*, *117*, C06031, 2012.

Winters, K., P. Lombard, J. Riley, and E. D'Asaro, Available potential energy and mixing in density-stratified fluids, *Journal of Fluid Mechanics*, *289*, 115–128, 1995.

Young, D., *Iterative solution of large linear systems*, Dover, 1971.

Zedel, L., A. Hay, R. Cabrera, and A. Lohrmann, Performance of a single-beam pulse-to-pulse coherent Doppler profiler, *Oceanic Engineering, IEEE Journal of*, *21*, 290–297, 1996.